Master's thesis

NTNU
Norwegian University of Science and Technology
Faculty of Natural Sciences
Department of Physics

Sara Abnar

Magnon-Mediated Superconductivity

Investigating the Emergence of Strong Topological Superconductivity Mediated by Magnons in a Coplanar, Non-Collinear Magnet

Master's thesis in Physics and mathematics (MTFYMA)
Supervisor: Asle Sudbø
Co-supervisor: Kristian Mæland
July 2023

NTNU
Norwegian University of
Science and Technology

Sara Abnar

Magnon-Mediated Superconductivity

Investigating the Emergence of Strong Topological Superconductivity Mediated by Magnons in a Coplanar, Non-Collinear Magnet

Master's thesis in Physics and mathematics (MTFYMA)
Supervisor: Asle Sudbø
Co-supervisor: Kristian Mæland
July 2023

Norwegian University of Science and Technology
Faculty of Natural Sciences
Department of Physics

NTNU
Norwegian University of
Science and Technology

Acknowledgements

In the pursuit of knowledge and the exploration of novel phenomena, no effort is solitary. Here, I express my sincerest appreciation to those who have played invaluable roles in the realisation of this thesis.

To my supervisor, professor Asle Sudbø, I am immensely grateful. Your guidance and expertise has helped me forward on this academic journey. I am honoured to have had the opportunity to learn from you.

I extend my heartfelt appreciation to my co-supervisor, Kristian Mæland, for your guidance and collaboration throughout this thesis. Your insights and critical feedback have helped me navigate several complex challenges.

I would like to thank you both for your patience throughout this semester. You have consistently shown remarkable patience and provided the guidance needed for my understanding, despite my numerous questions and requests for clarification. Thank you both, for your patience and support.

My deepest gratitude extends to my loving partner. Your belief in my abilities and your constant encouragement have been an incredible source of motivation for me. Your patience and understanding has provided me with the strength I needed during the highs and lows. Thank you for supporting me unconditionally.

To my incredible family, who have always been my pillars of support, I am immensely grateful. Through your continuous encouragement and support, you have inspired me to reach new heights. Thank you for your endless love, positive encouragement, and countless sacrifices that have enabled me to pursue my dreams.

Last, but not least, I would like to express my deepest gratitude to the research centre QuSpin. Your inspiring work environment has played a vital role in shaping my academic growth. To my fellow master's students at QuSpin, I am truly thankful for your continuous efforts in ensuring that I take breaks and maintain a healthy work-life balance. Thank you for being an integral part of this memorable experience.

I extend my sincere acknowledgement to all individuals who have been a part of my academic education as a whole. Thank you for making this journey enjoyable with your presence and encouragement.

Sara Abnar
Trondheim, Norway
July 2023

Note to the examiner

With the purpose of a self-contained thesis, parts of previous work is included. Specifically, the chapters marked with asterisk (*) are inspired by work from my project thesis, while chapters marked with double asterisk (**) are taken directly from my project thesis, only with minor modifications. This being said, I hope you enjoy reading the work from my journey.

Abstract

This master's thesis investigates whether strong topological superconductivity can manifest in a bilayer system comprising a normal metal and a coplanar spin-phase magnet. We build upon the work by Mæland and Sudbø [1], who successfully derived strong topological superconductivity in a bilayer comprising a normal metal and a skyrmion spin crystal ferromagnetic insulator. Thus, our research aims to extend these findings and investigate the emergence of strong topological superconductivity in a normal metal/spiral-phase ferromagnetic insulator bilayer.

This investigation employs a combination of theoretical frameworks, including the Holstein-Primakoff transformation, Schrieffer-Wolff transformation, Bogoliubov transformation, and the Bardeen-Cooper-Schrieffer theory. To simplify the analysis, certain assumptions are made, such as disregarding easy-axis anisotropy and considering a single-component Dzyaloshinskii-Moriya interaction. The analysis is performed on a triangular lattice with lattice matching between the normal metal and spiral-phase ferromagnetic insulator monolayers.

The key findings of this study reveal the absence of strong topological superconductivity in the studied system. We attempted to understand the underlying factors giving rise to this nonexistence of strong topological superconductivity by retracing our calculations. It is concluded that we may gain deeper insights into the absence of strong topological superconductivity from an analytical expression for the Bogoliubov transformation matrix. Nevertheless, deriving an analytical expression for this 20×20 sized matrix is a daunting problem. Even if these expressions were to be obtained, their interpretation would yet be highly challenging due to their considerable length and complexity. The implications of these findings encourage future research of studying a corresponding system, though of fewer sub-lattices. This will reduce the matrix size, making an analytical derivation of the Bogoliubov transformation matrix more feasible. By implementing these adjustments, future researchers may proceed to investigate whether any coplanar spin-structured magnet in bilayer with a normal metal may give rise to strong topological superconductivity.

This research is motivated by that coplanar spin states possess lower energy compared to skyrmion spin states [2], thereby favouring the practical creation and stability of spiral-phase spin structures. Although the current investigation did not yield strong topological superconductivity, it provides a comprehensive analysis of a spiral-phase ferromagnetic insulator in bilayer with a normal metal, thereby opening for specific future studies on the interplay between topological properties and coplanar spin structures.

In conclusion, this research contributes to the understanding of magnon-mediated

topological superconductivity in coplanar, non-collinear magnets. The findings underscore the importance of obtaining an analytical expression for the Bogoliubov transformation matrix and lay the foundation for future investigations in this field.

Sammendrag

Denne masteroppgaven undersøker hvorvidt topologisk superledning kan oppstå i et bilagssystem bestående av et normalmetall og en magnet med koplanær spinnfase. Vi bygger videre på arbeidet til Mæland og Sudbø [1], som fant topologisk superledning i en heterostruktur bestående av et normalmetall og en ferromagnetisk isolator med skyrmion-spinnfase. Med dette sikter vårt studie på å undersøke fremveksten av sterk topologisk superledning i et normalmetall/koplanær spiral-spinnfase ferromagnetisk insulator bilagssystem.

Denne studien benytter seg av en kombinasjon av teoretiske rammeverk, inkludert Holstein-Primakoff transformasjonen, Schrieffer-Wolff transformasjonen, Bogoliubov-transformasjonen og Bardeen-Cooper-Schrieffer teorien. For å forenkle analysen gjøres flere antakelser, for eksempel ved å se bort fra enkel-akse-anisotropi og begrense til kun én komponent av den antisymmetriske vekselvirkningen. Analysen utføres på en triklinisk gitterstruktur med samsvar mellom monolagene av normalmetall og spinnfase-ferromagnetisk insulator.

Funnene i denne studien viser fraværet av sterk topologisk superledning i det undersøkte systemet. Vi forsøkte å forstå de underliggende faktorene som fører til dette fraværet av sterk topologisk superledning ved å gjennomgå beregningene. Vi konkluderer med at vi kan få dypere innsikt i bakgrunnen for fraværet av sterk topologisk superledning fra et analytisk uttrykk for Bogoliubov-transformasjonsmatrisen. På den annen side er utledningen av et analytisk utrykk for denne 20×20 store matrisen en omfattende oppgave. Selv hvis man utleder disse utrykkene, vil deres tolkning være svært utfordrene som konsekvens av deres lengde og kompleksitet. Med dette oppfordres videre forskning på et tilsvarende system dog med færre undergittre, slik at matrisestørrelsen reduseres. Dermed åpnes muligheten for å utlede analytiske utrykk for elementene av Bogoliubov matrisen. Slik kan fremtidige forskere fortsette undersøkelsen på hvorvidt koplanare spinnstrukturer i magneter i heterostruktur med normalmetaller kan gi grunnlag for sterk topologisk superledning.

Denne forskningen er motivert av at koplanære spinntilstander har lavere energi sammenlignet med skyrmion tilstander, og dermed favoriserer praktisk opprettelse og stabilitet av spiralfase spinnstrukturer [2]. Selv om denne studien konkluderte med fraværet av sterk topologisk superledning, gis en grundig analyse av en spinnfase-ferromagnet i et bilagssystem med et normalmetall, og dermed åpner for spesifikke videre studier på det komplekse samspillet mellom topologiske egenskaper og koplanære spinn-strukturer.

Avslutningsvis bidrar denne forskningen til forståelsen av magnon-mediert to-

pologisk superledning i koplanære, ikke-kolineære magneter. Funnene understreker viktigheten av å utlede et analytisk uttrykk for Bogoliubov-transformasjonsmatrisen, og legger et grunnlag for fremtidig forskning på dette feltet.

Table of Contents

List of Figures

List of Acronyms

eBZ1 first electron Brillouin zone. 33, 36, 37, 41, 42

eBZ electron Brillouin zone. xi, xiii, 22, 30, 33, 36, 38, 42

mBZ1 first magnon Brillouin zone. 36, 37, 40, 41

mBZ magnon Brillouin zone. xi, xiii, 30, 33, 36, 41–43

BCS Bardeen-Cooper-Schrieffer; used in the context of their theory or paper [3]. v, vii, 1, 4, 8, 9, 29, 35, 42, 47, 60, 62

BdG Bogoliubov-de-Gennes. 10

BZ Brillouin zone. 42

DMI Dzyaloshinskii-Moriya interaction. v, 3, 20, 23, 24, 27, 35, 39, 68

DoS density of states. xi, 22, 23, 36–38

FMI ferromagnetic insulator. 3, 39, 69

HP Holstein-Primakoff; used in the context of their transformation [4]. v, vii, 12, 13, 24, 25, 29, 65, 69, 79, 80

NM normal metal. v, 3, 4, 11, 19, 21, 29, 30, 35, 36, 69

SOC spin-orbit coupling. 23

SPFMI spiral [spin]-phase ferromagnetic insulator. v, xi, 3, 4, 11–13, 15, 19, 20, 23, 24, 26, 28–30, 35–37, 39, 65, 68, 69

1 Introduction

1.1 *Background and motivation

Superconductivity, the remarkable phenomenon discovered by Heike Kamerlingh Onnes in 1911 [5], continues to fascinate condensed matter physicists with its novel properties. In his work, Onnes discovered that "at very low temperatures [...] the resistance [of mercury] would, within the limits of experimental accuracy, become zero" [5, No. 120b, p. 18]. Additionally, he noted that the superconducting transition temperature (also referred to as *critical temperature*) of mercury was about 4K. These observations fascinated the physicists to date, leading several succeeding experiments. Not before 1933 did Walther Meissner and Robert Ochsenfeld discover that superconductors also expel any external magnetic field [6]; the effect now known as the Meissner effect. With the experimental observations of superconductivity at hand, the quest for a solid theoretical explanation was highly sought.

The theories of superconductivity were not established before almost half a century after its discovery by Onnes. In 1950, the macroscopic properties of superconductors were successfully explained by the Ginzburg-Landau theory proposed by V. Ginzburg and L. Landau [7]. However, a complete microscopic theory of superconductivity was first formulated in 1957, known as the BCS theory after the physicists J. Bardeen, L.N. Cooper, and R. Schrieffer [3]. Succeeding these theories, newer theories and experiments indicate the occurrence of superconductivity at higher transition temperatures [8, 9, 10]. Despite the significant progress in this field, several fundamental questions remain unanswered, necessitating further research.

The study of superconductors is motivated by its many technological advancements. These advancements include energy-efficient power transmission, medical imaging, particle accelerators, and quantum technologies [11].

In recent years, the exploration of topological superconductors has emerged as a frontier area of research, with major applications in quantum computing [12, 13, 14]. Quantum computing has the potential to revolutionise computing both in terms of computational power and energy efficiency, thus surpassing classical computers [15]. Classical computers rely on manipulating classical bits through heat-generating mechanics [16, 17]. In contrast, quantum computers store information in the quantum bits, also known as *qubits*, which utilise the quantum mechanical properties of superposition and entanglement [18]. These features of qubits allow for parallel computations, reducing the number of operations required for certain tasks

and hence increasing time and energy efficiency. However, a significant challenge in quantum computing is quantum decoherence, where even small perturbations can corrupt the information stored in qubits [19, 20]. To address this challenge, researchers have been exploring the integration of topological superconductors into quantum computing systems, which may protect the fragile qubits from decoherence hence enhance quantum coherence [21]. This motivates the ongoing research on topological superconductors.

Topological superconductivity is a rapidly advancing field in condensed matter physics investigating the unconventional properties of certain superconducting materials [12, 13]. Unlike conventional superconductors (also referred to as *topologically trivial* superconductors), topological superconductors exhibit non-trivial topological characteristics leading the emergence of protected boundary states. Topological superconductors may be classified from the symmetries of the superconducting gap.

The paper on *Topological Superconductivity Mediated by Skyrmionic Magnons* by Mæland and Sudbø [1] provides insights into the manifestation of strong topological superconductivity at the interface between a skyrmion crystal magnet and a normal metal. The choice of investigating interfaces is motivated by the novel electronic properties that arise at the interface between different materials [22]. Note that in strong topological superconductors, the superconducting state is characterised by nontrivial topology, giving rise to robust surface states that are protected against local perturbations [12]. In contrast, weak topological superconductors lack such robustness, thus being more susceptible to perturbations. This motivates the sought of strong topological characteristics. Furthermore, the authors discuss whether the use of a coplanar and non-collinear spin-state magnet could produce similar results, leaving this at an open question.

Other literature have studied the topology at the interface of a conventional superconductor and a spiral or skyrmion spin structure magnet [23, 24]. The authors of these papers found that a non-coplanar skyrmion spin structure was required to obtain strong topological superconductivity. Note however that their system is significantly different from that in [1]. In this light, our curiosity returns to whether a coplanar spin phase magnet is sufficient for strong topological superconductivity in a normal metal/magnet bilayer.

With the aforementioned findings at hand, this thesis aims to investigate the potential manifestation of strong topological superconductivity at the interface of a bilayer composed of a normal metal and a coplanar, non-collinear spin-phase magnet. The investigation of coplanar, non-collinear spin structures as potential hosts of strong topological superconductivity is driven by their lower energy states compared to skyrmion crystals [2]. This relative stability and ease of manipulation make coplanar spin configurations appealing for experimental exploration and practical applications. If coplanar spin structures are found to exhibit strong topological superconductivity, it could thus yield major advancements in the field of condensed matter physics. Thereby, our understanding of fundamental physics may be advanced, and technological advancements may be achieved, by investigating strong topological superconductivity at the interface of a normal metal and a coplanar, non-collinear spin-phase magnet.

In summary, this thesis investigates the potential manifestation of strong topological superconductivity at the interface of a bilayer comprising a normal metal and a coplanar, non-collinear spin-phase magnet. This is done by studying the symmetries of the gap parameters of our system. Eventually, we aim to contribute the understanding of strong topological superconductors.

1.2 *Scope and delimitations

This report aims to study the bilayer of a normal metal (NM) and a coplanar, non-collinear magnet, and the potential emergence of strong topological superconductivity at the interface. In more detail, we seek to determine the symmetries of the superconducting state of this bilayer model. In achieving this, some simplifications and approximations were made. With this section, we propose to clarify the scope and delimitations of this thesis.

The first delimitation to note, is the consideration of the magnetic layer to be a ferromagnetic insulator (FMI) providing the interesting properties such as insulating behaviour and magnetic order [25]. Despite these properties, the magnetic order of the FMI is perturbed by quantised spin-fluctuations, known as *magnons*. By incorporating a ferromagnetic insulator in the bilayer system, it is possible to explore the interplay between layers without allowing the electrons of the NM to disorder the spin-structure of the FMI.

Moreover, as our magnetic layer is insulating, this thesis will for brevity refer to *electrons in the NM* when considering electrons, and *magnons in the FMI* when considering magnons.

Furthermore, we let the FMI have a coplanar and non-collinear spiral-phase spin structure, and is hereby referred to as SPFMI. In this context, three crucial couplings come into play: the influence of easy-axis anisotropy, the Dzyaloshinskii-Moriya interaction (DMI), and the symmetric exchange coupling within the magnet [1]. For simplicity, we eventually disregard the easy-axis anisotropy; consider DMI only along the global $\hat{y}$-axis; and let the spin-coupling within the magnet be diagonal. The interplay between these couplings is seen to give rise to a coplanar, non-collinear SPFMI.

Another delimitation of this thesis regards the motion of the electrons in the NM. We let the NM be described by the tight-binding model, only allowing nearest-neighbour hopping of the electrons. This hopping is additionally limited to be spin-conserving.

Moreover, this thesis delimits to lattice matching of the SPFMI and NM, thus disregarding any lattice strain at the bilayer interface. This delimitation greatly simplifies the calculations required to characterise the topology of our superconductor.

Furthermore, this thesis delimits to weak interactions between corresponding lattice sites across the bilayer interface (electron-magnon interactions). This is a direct consequence of the spatially exponentially decaying nature of atomic wave functions, leading little overlap between the wave-functions of the NM and the SPFMI. There-

fore, the electron-magnon coupling strength may be considered a perturbation; any term beyond the second order in this coupling strength is neglected.

Motivated by the low-temperature regime of superconductors, this thesis considers low temperatures of the system. This is analogous to assuming that the SPFMI is nearly ordered with localised spins fluctuating by first-order magnon interactions [26, p. 49]. In other words, interactions beyond lowest order in magnon creation or annihilation operators are negligible. As a consequence, the exchange coupling is assumed weak and only finite between nearest-neighbouring sites.

The low temperature also leads to few available electron-magnon scattering states [27]. Resultingly, the electron-magnon scattering is only present for electron momenta within a thin shell enclosing the Fermi-surface. This restriction on the electron momenta suggests that the system may be quantised.

Furthermore, the system Hamiltonian is reduced in the formalism of the BCS theory of superconductivity, presented in [3]. In our system, the quantised spin-fluctuations are anticipated to play a role analogous to phonons in the BCS theory of superconductivity. Thereby, we expect magnons to mediate electron-electron interactions and facilitate Cooper pair formation. In this light, we investigate whether the magnons of the SPFMI may facilitate the emergence of strong topological superconductivity.

1.3 Structure of thesis

We aim to prepare the reader for the content and structure of this thesis by presenting its framework.

The preliminaries in chapter 2 sets the groundwork of this thesis, introducing the crucial background knowledge in order to follow the relevant arguments and calculations. In section 2.1, we clarify the notation employed in this thesis. Then, we continue to briefly discuss the theory of superconductivity in section 2.2. From this, we review relevant operator properties in section 2.3, before the Bogoliubov transformation is presented in section 2.4. At last, the Schrieffer-Wolff transformation is presented in section 2.5.

Succeedingly, the models of our bilayer system are presented in chapter 3. Here, we first present the model for the normal metal (NM) in section 3.1, before continuing to the model of the spiral-phase ferromagnetic insulator (SPFMI) in section 3.2. In section 3.3 we present the exchange interaction at the bilayer interface.

We continue to formulate the system as an effective electron-electron interaction in chapter 4. Accordingly, the total system Hamiltonian is transformed in the framework of the Schrieffer-Wolff transformation. From this we obtain the effective interaction potential.

In chapter 5 we apply simplifications to our model, letting us solve the system in more detail. Introductory to this chapter, these simplifications are stated and validated. Then we proceed to study the NM, the SPFMI, and the effective interaction potential in sections 5.1 to 5.3, respectively.

With this at hand, we continue to investigate the superconducting system in

terms of these simplifications in chapter 6. In section 6.1, we formulate the effective interaction Hamiltonian as a self-consistent one-particle problem in the mean-field approximation. Thus, we apply the Bogoliubov transformation to diagonalise this Hamiltonian in terms of new fermionic quasi-particles called Bogoliubons. The energy spectrum of these Bogoliubons is seemingly gapped, and we obtain the corresponding gap equation in section 6.2. Here, the Helmholtz free energy is minimised to ensure that our system is at its energetically favourable state. The gap equation on matrix notation is derived in section 6.2.1, in terms of the coupling functions matrix. In section 6.2.2, we linearise the gap equation to eventually solve it numerically in section 6.2.3. We finalise this chapter with a discussion of possible origins of the results in section 6.2.4.

Chapter 7 concludes the results of this thesis while presenting an encouraged outlook for future research.

At last, the Appendices are provided with the intention to present additional information whenever seen helpful, without removing focus. This information is either in form of more detailed calculations, or in form of plots.

2 Preliminaries

2.1 Notation

In the field of physics, mathematics serves as a profound tool for understanding the world around us. Achieving this understanding necessitates a solid grasp of the notation used to describe mathematical concepts.

This report employs the established groundwork of notation in physics, with few additions. In the sought of coherent communication, the employed notation is in this section presented and clarified. This includes notation for various quantities, such as vectors, matrices, as well as that for various operations.

Vector and matrix quantities are primarily denoted in bold, with a few exceptions. The first exception applies to unit vectors that are denoted with hat, such that $\hat{x} = \boldsymbol{x}/x$ for $x = |\boldsymbol{x}|$. Moreover, for any set of particle operators, we adapt the nomenclature introduced by Tsallis in [28]: we write $\langle a_{\boldsymbol{q}}| = (a_{\boldsymbol{q},1}\ a_{\boldsymbol{q},2} \cdots a_{\boldsymbol{q},m}) = |a_{\boldsymbol{q}}\rangle^\dagger$ for the set of m particle operators $a_{\boldsymbol{q},i}$ of momentum $\boldsymbol{q}$. We extend this bra-ket notation to also apply for column vectors $|\alpha_i\rangle$ of a matrix $\boldsymbol{A}$. Note therefore that the bra-ket notation in this thesis is not used in the context of quantum mechanical states, as in traditions. To avoid confusion, the reader must keep these conventions in mind.

Furthermore, we may classify the order of terms: a term is of order n in A, denoted as $\mathcal{O}(A^n)$, if it represents a product comprising n elements of the matrix $\boldsymbol{A}$. Note thus that this definition disregards which elements constitute the product; the products $A_{ij}A_{ml}$ and $(A_{ij})^2$ are both $\mathcal{O}(A^2)$. This convention is analogous for products of vector elements. Note also that diagonal matrix elements $A_{ii} \equiv A_i$ for brevity of notation. Thereby, the diagonal matrix elements must not be confused with vector elements, as should be clear from the context.

Occasionally, vector and matrix elements may be denoted by several sub- and superscripts. In general, the Latin letters i, j in subscript represent atomic lattice sites, while $\boldsymbol{q}, \boldsymbol{k}$ denote the momentum state. Additionally, the Greek and Latin letters $\alpha, \beta \in \{x, y, z\}$ indicate the axis of projection. For quantities whose axis of projection must be clarified in addition to the lattice site or momentum state, the parameters denoting the axis of projection are written as superscripts. For instance, s_i^z symbolises the spin along the global spin $\hat{z}$-axis of an electron on lattice site i; while k_x is the electron momentum along the $\hat{k}_x$-axis. Moreover, the sub- and superscript $\sigma \in \{\uparrow, \downarrow\}$ denotes a spin-state, while any variable $\sigma \in \{+, -\}$ denotes

the corresponding spin eigenvalue. Altogether, one must be careful to understand the notation of sub- and superscripts from the context.

Furthermore, the matrix operators used in this report are: the inverse operator, denoted $(\cdot)^{-1}$; the complex conjugate, $(\cdot)^*$; and the transpose $(\cdot)^T$. Note that these operators commute with each other [29]. In this report, these operators may be combined to give the conjugate transpose, also referred to as the *adjoint* operator, or the *Hermitian conjugate* $(\cdot)^{*T} \equiv (\cdot)^\dagger$; the inverse adjoint $((\cdot)^{-1})^\dagger \equiv (\cdot)^{-\dagger}$; and the inverse transpose $((\cdot)^{-1})^T \equiv (\cdot)^{-T}$.

Additionally, some mathematical operators are employed for the purpose of clarity and brevity of notation. For instance, the mathematical equating operator $\stackrel{!}{=}$ is used to indicate the requirement of equating the right-hand side with the left-hand side. Moreover, the sum over all sites i and its nearest neighbours j is denoted $\sum_{\langle i,j\rangle}$. Occasionally this summation is limited to a given site i, at which the sum over its nearest neighbours j is represented by $\sum_{\langle j\rangle_i}$.

Moreover, the notation h.c is introduced for brevity of notation in mathematical expressions, representing the hermitian conjugate of the preceding terms, within the same parentheses if applicable. For example, the expression $A + (B + \text{h.c}) = A + B + B^\dagger$, while $A + B + \text{h.c} = A + B + A^\dagger + B^\dagger$.

At a last note, $\hbar = 1$ throughout this thesis, i.e., Planck units are employed.

2.2 Theory of superconductivity

The interplay between research and practical applications of superconductivity has motivated scientists to explore its enigmas, revealing a realm of possibilities that may have, and possibly will, revolutionise the utilisation of electric currents [11]. This section presents the underlying theory behind the phenomenon of superconductivity. We explain the theory behind conventional superconductors, followed by an outline of the theory behind topologically non-trivial superconductivity.

2.2.1 Conventional superconductors

The BCS theory is a comprehensive microscopic theory of conventional superconductivity, postulating its emergence from the condensation of electron pairs [3]. These electron pairs were soon referred to as Cooper pairs; the weakly bound electron pairs of opposite spin and momenta.

In the conventional superconductor, the electron pairing exhibits s-wave symmetry; the Cooper pairs consist of electrons with opposite spin, forming a singlet Cooper pair [13]. Moreover, a spin-singlet pair potential has a total angular momentum ℓ even, while that of a spin-triplet has ℓ odd [12]. We draw an analogy with atomic orbitals to conclude that Cooper pairs with $\ell = 0, 1$ manifest s- and p-wave symmetry, respectively. The corresponding basis functions may be defined in a simplified representation. In terms of the angle $\theta = \arctan(k_y/k_x)$ for $\boldsymbol{k}$ the electron energy on the Fermi surface: the s-state is constant, while the p_x and p_y go as $\cos\theta$ and $\sin\theta$, respectively [30]. The pairing symmetries apart from s-wave

are common in unconventional superconductors. In these, the Cooper pairs may be spin-triplets; either comprising spinfull electrons of opposite spin, or spinless (spin-polarised) electrons.

Furthermore, the BCS theory considers the formation of these Cooper pairs resulting from the effective interaction between electrons as mediated by phonons [3]. In addition, the founders of the BCS paper found that the superconducting state is characterised by an energy gap separating the ground state condensate from excited states, hence the *super*conductivity. Thereby, the breakdown of superconductivity is associated with the breakdown of Cooper pairs. This breakdown occurs at transition temperatures corresponding to the low binding energy of Cooper pairs, resulting the low-temperature regime of superconductors.

At the transition temperature T_c, the material undergoes a phase transition from normal to superconducting state, thereby exhibiting zero electrical resistance [5]. It goes without saying that the low T_c of conventional superconductors may significantly limit their practical applications. Nevertheless, the recent emergence of high-T_c superconductors has sparked tremendous interest and potential for practical applications in various fields [13, ch. 8–10]. Note however that high-T_c values are still far below room temperature. To this day, it remains a challenge to develop room-temperature superconductors.

Another challenge of superconductors lies in their applications in quantum computing. Superconducting qubits are typically formed using superconducting circuits consisting of Josephson junctions; i.e., devices that exhibit superconducting properties [19, 13]. The Josephson junctions can be designed to behave as qubits, with two distinguishable quantum states representing the logical 0 and 1 states of the qubit. Conventional superconductors may be susceptible to perturbations, such that the decoherence time of the superconducting qubits is insufficient. A solution to this limitation is the application of topological superconductors; their unique properties lead robustness against local perturbations [31].

2.2.2 Topological superconductivity

Topological superconductors are materials that display properties of superconductivity under the principles of topology. The concept of topology originates from mathematics, explaining the invariant properties of a material under continuous deformations [32].

Moreover, topological superconductors are associated with Majorana fermions; excotic quasi-particles which are their own antiparticles [33]. These Majorana fermions are described by non-Abelian statistics, meaning that particle exchanges are non-trivial operations which in general do not commute [13]. This property of the Majorana fermions gives rise to various characteristics of topological superconductors, making these materials ideal for applications in topological quantum computers [34, 35, 36].

The characterisation of topological superconductors is often in terms of a fully gapped bulk energy spectrum while hosting protected gapless surface or edge states [12]. In the absence of the gapless surface or edge states, the material is clas-

sified as a bulk topological superconductor. Furthermore, the fully gapped bulk energy spectrum is a general recognition for the formation of strong topological superconductivity. Thereby, we distinguish between conventional superconductors, which are topologically trivial; weak topological superconductors, which have topologically protected gap nodes; and strong topological superconductors, which host fully gapped bulk exitations. Resultingly, the symmetry properties of the superconducting gap may provide sufficient information to classify the topology of superconductors [12].

The classification of superconductors in terms of topology is usually conducted by computing a bulk topological invariant [12]. A bulk topological invariant is an integer used to distinguish the topological superconducting state (nonzero integer) from the topologically trivial superconducting state (null integer). In quantum condensed matter, we may consider two main categories for such topological invariants: the Chern number for systems with broken time-reversal symmetry, and the $\mathbb{Z}_2$ invariant for systems which conserve this symmetry.

In this thesis, the system considered is time-reversal symmetric, as we will note later. Thus, we may easily define the $\mathbb{Z}_2$ for a system in which the mean-field Hamiltonian is spin-decoupled. As will be clear later (see section 6.1), this spin-decoupled Hamiltonian would in our system require $\Delta_{\boldsymbol{k}\uparrow\downarrow} = \Delta_{\boldsymbol{k}\downarrow\uparrow} = 0$ for the unpolarised superconducting gaps. Equivalently, we may attempt to continuously close these gaps; the classification of strong topological superconductivity remains under this transformation [31].

For this reason, define the Bogoliubov-de-Gennes (BdG) Hamiltonian as in the following

$$\mathcal{H}_{\mathrm{BdG}}(x) = \frac{1}{2}\sum_{\boldsymbol{k}} \langle \Psi_{\boldsymbol{k}} |\, \mathbf{H}_{\boldsymbol{k}}(x)\, | \Psi_{\boldsymbol{k}} \rangle \,, \tag{2.2.1}$$

with $\langle \Psi_{\boldsymbol{k}}| = \left(c^\dagger_{\boldsymbol{k}\uparrow},\ c^\dagger_{\boldsymbol{k}\downarrow},\ c_{-\boldsymbol{k}\downarrow},\ c_{-\boldsymbol{k}\uparrow}\right) = |\Psi_{\boldsymbol{k}}\rangle^\dagger$, and the matrix

$$\mathbf{H}_{\boldsymbol{k}} = \begin{pmatrix} \epsilon_{\boldsymbol{k}} & 0 & \Delta_{\boldsymbol{k}\uparrow\downarrow}(1-x) & \Delta_{\boldsymbol{k}\uparrow\uparrow} \\ 0 & \epsilon_{\boldsymbol{k}} & \Delta_{\boldsymbol{k}\downarrow\downarrow} & \Delta_{\boldsymbol{k}\downarrow\uparrow}(1-x) \\ \Delta^\dagger_{\boldsymbol{k}\uparrow\downarrow}(1-x) & \Delta^\dagger_{\boldsymbol{k}\downarrow\downarrow} & -\epsilon_{-\boldsymbol{k}} & 0 \\ \Delta^\dagger_{\boldsymbol{k}\uparrow\uparrow} & \Delta^\dagger_{\boldsymbol{k}\downarrow\uparrow}(1-x) & 0 & -\epsilon_{-\boldsymbol{k}} \end{pmatrix}. \tag{2.2.2}$$

If the fully gapped bulk remains for all $x \in [0,1]$, we may proceed to calculate the topological invariant to classify whether our system displays strong topological superconductivity. For such a system, the bulk topological $\mathbb{Z}_2$ invariant is defined as

$$\nu_{\mathbb{Z}_2} = \frac{1}{2}\left(N_\uparrow - N_\downarrow\right) \mod 2, \tag{2.2.3}$$

in which the winding number

$$N_\sigma = \frac{1}{8\pi}\int_{\mathrm{eBZ}} \mathrm{d}\boldsymbol{k}\, \epsilon_{ij}\hat{d}_{\boldsymbol{k}\sigma}\cdot\left(\partial_{k_i}\hat{d}_{\boldsymbol{k}\sigma}\times\partial_{k_j}\hat{d}_{\boldsymbol{k}\sigma}\right), \tag{2.2.4}$$

is an integral over the electron Brillouin zone [1, 31]. Due to time-reversal symmetry, we note that $N_\uparrow = -N_\downarrow$. Moreover, ϵ_{ij} is the Levi-Civita tensor for $i, j \in \{x, y\}$, and $\hat{d}_{\boldsymbol{k}\sigma}$ is the unit vector along $\boldsymbol{d}_{\boldsymbol{k}\sigma}$. Following [1], the $\boldsymbol{d}_{\boldsymbol{k}\sigma}$-vector is defined as follows

$$\boldsymbol{d}_{\boldsymbol{k}\sigma} = \Big(\mathfrak{Re}(\Delta_{\boldsymbol{k}\sigma\sigma}),\ -\mathfrak{Im}(\Delta_{\boldsymbol{k}\sigma\sigma}),\ \epsilon_{\boldsymbol{k}}\Big), \tag{2.2.5}$$

in which all components must be finite to avoid a trivial null-solution of the winding number.

Thereby, to classify the topology of our superconductor, we first obtain the symmetries of the superconducting gap parameters $\Delta_{\boldsymbol{k}\sigma_1\sigma_2}$. From this we determine whether the superconducting gap is nodeless. If this is the case, we proceed to investigate whether this gap remains fully gapped by continuosly closing the unpolarised gaps. If so, we continue to assure that $\Delta_{\boldsymbol{k}\sigma\sigma}$ are complex with finite real and imaginary parts before calculating the winding number in eq. (2.2.4). At last, we must insert N_σ into the topological invariant eq. (2.2.3) to classify the topology of our system.

2.3 **Operator properties

It is essential to present some operator properties to use in obtaining the model Hamiltonian. This includes operators such as the spin operator of lattice site i in the NM, $\boldsymbol{s}_i$ referred to as the fermion spin operator; the spin operator of site i in the SPFMI, $\boldsymbol{S}_i$ referred to as the boson spin operator; and the fermion and boson creation and annihilation operators. The properties of interest are the commutation relations; the fermion/boson spin-flip operators; and the dot products between two spin operators.

Consider first the commutation relations between operators. For the components of some general spin operator $\boldsymbol{A}$, this is given by [30, p. 177-178]

$$[A_i,\ A_j] = i\epsilon_{ijk}A_k, \tag{2.3.1}$$

where $i = \sqrt{-1}$ is the imaginary unit, and ϵ_{ijk} is the rank 3 Levi-Civita tensor [37, p. 144].

The commutation relation between the boson creation and annihilation operators $a_i^{(\dagger)}$ is [4, p. 15].

$$\left[a_i,\ a_j^\dagger\right] = \delta_{i,j}, \tag{2.3.2a}$$
$$\left[a_i^\dagger,\ a_j\right] = -\delta_{i,j}, \tag{2.3.2b}$$
$$[a_i,\ a_j] = 0. \tag{2.3.2c}$$

However, the fermion creation and annihilation operators $c_{i\sigma}^{(\dagger)}$ must satisfy

$$\{c_{i\sigma}^\dagger,\ c_{j\sigma'}\} = \delta_{i,j}\delta_{\sigma,\sigma'}, \tag{2.3.3a}$$
$$\{c_{i\sigma},\ c_{j\sigma'}\} = 0, \tag{2.3.3b}$$

the fermionic anti-commutation relation [4, p. 76].

Let us now obtain the corresponding spin-flip operators of $\boldsymbol{s}_i$ and $\boldsymbol{S}_i$. Generally, the spin-flip operator

$$A_+ = A_-^\dagger = A^x \pm iA^y, \tag{2.3.4}$$

of some spin operator $\boldsymbol{A}$ with real components [30, p. 172-173].

The relation in eq. (2.3.4) may be inverted to

$$A^x = \frac{1}{2}\left(A_+ + A_-\right), \tag{2.3.5a}$$

$$A^y = \frac{1}{2i}\left(A_+ - A_-\right). \tag{2.3.5b}$$

Thus, the general spin operator may be written component-wise as

$$\boldsymbol{A} = \frac{1}{2}\left(A_+ + A_-\right)\hat{x} + \frac{1}{2}\left(A_+ - A_-\right)\hat{y} + A^z\hat{z}. \tag{2.3.6}$$

Apply this to the atomic orbital spin operator. This is given by

$$\boldsymbol{s}_i = \frac{1}{2}\left\langle c_i\right|\boldsymbol{\sigma}\left|c_i\right\rangle, \tag{2.3.7}$$

where $\boldsymbol{\sigma}$ is the row vector of Pauli-matrices, and the spinor $\langle c_i| = \left(c_{i\uparrow}^\dagger \; c_{i\downarrow}^\dagger\right) = |c_i\rangle^\dagger$ consists of fermion operators [26, p. 134]. The spin z-component s_i^z is then

$$s_i^z = \frac{1}{2}\left\langle c_i\right|\boldsymbol{\sigma^z}\left|c_i\right\rangle \tag{2.3.8a}$$

$$= \frac{1}{2}\begin{pmatrix} c_{i\uparrow}^\dagger & c_{i\downarrow}^\dagger \end{pmatrix}\begin{pmatrix} 1 & 0 \\ 0 & -1 \end{pmatrix}\begin{pmatrix} c_{i\uparrow} \\ c_{i\downarrow} \end{pmatrix} \tag{2.3.8b}$$

$$= \frac{1}{2}\sum_\sigma c_{i\sigma}^\dagger \sigma c_{i\sigma}, \tag{2.3.8c}$$

where the Pauli matrix $\boldsymbol{\sigma^z}$ was inserted for.

The corresponding spin-flip operators are given by

$$s_{i+} = c_{i\uparrow}^\dagger c_{i\downarrow} \tag{2.3.9a}$$

$$s_{i-} = c_{i\downarrow}^\dagger c_{i\uparrow} \tag{2.3.9b}$$

Thus, inserting eqs. (2.3.8c) and (2.3.9) into eq. (2.3.6) for $\boldsymbol{A} = \boldsymbol{s}_i$, the fermion spin operator may be written component-wise as

$$\boldsymbol{s}_i = \frac{1}{2}\left(c_{i\uparrow}^\dagger c_{i\downarrow} + c_{i\downarrow}^\dagger c_{i\uparrow}\right)\hat{x} + \frac{1}{2i}\left(c_{i\uparrow}^\dagger c_{i\downarrow} - c_{i\downarrow}^\dagger c_{i\uparrow}\right)\hat{y} + \frac{1}{2}\sum_\sigma c_{i\sigma}^\dagger \sigma c_{i\sigma}\hat{z} \tag{2.3.10}$$

On the other hand, the explicit expression for the boson spin operator is approximated due to the spin fluctuations in the SPFMI; the local S_i^z-component is obtained using the Holstein-Primakoff (HP) transformation [4, p. 50]

$$S_i^z = S - a_i^\dagger a_i \tag{2.3.11}$$

where $S = 1/2$ is the ordered spin at site i of the SPFMI.

The boson spin-flip operators may be obtained first by using eq. (2.3.4) to rewrite the following product

$$S_{i+}S_{i-} = \left(S_i^x + iS_i^y\right)\left(S_i^x - iS_i^y\right) \tag{2.3.12a}$$

writing out the product gives

$$S_{i+}S_{i-} = \left(S_i^x\right)^2 + \left(S_i^y\right)^2 - iS_i^xS_i^y + iS_i^yS_i^x \tag{2.3.12b}$$

inserting $\boldsymbol{S}_i^2 = \left(S_i^x\right)^2 + \left(S_i^y\right)^2 + \left(S_i^z\right)^2$ and rewriting the last two terms into a commutator, we obtain

$$S_{i+}S_{i-} = \boldsymbol{S}_i^2 - \left(S_i^z\right)^2 - i\left[S_i^x,\ S_i^y\right] \tag{2.3.12c}$$

in which each term may be inserted for: for the first term, we use the identity $\boldsymbol{S}_i^2 = S\left(S+1\right)$ [4, p. 50]; for the second term we insert the HP transformation from eq. (2.3.11); and in the last term we insert the spin commutation relation eq. (2.3.1) for $(ijk) = (xyz)$. We then get

$$S_{i+}S_{i-} = S^2 + S - \left(S - a_i^\dagger a_i\right)^2 - i\left(iS_i^z\right) \tag{2.3.12d}$$

writing out the third term and again inserting for the HP transformation in the last term, gives

$$S_{i+}S_{i-} = S + 2Sa_i^\dagger a_i - \left(a_i^\dagger a_i\right)^2 + S - a_i^\dagger a_i \tag{2.3.12e}$$

$$= \left(2S - a_i^\dagger a_i\right)a_i^\dagger a_i + \left(2S - a_i^\dagger a_i\right) \tag{2.3.12f}$$

thus, using the the boson commutation relations in eq. (2.3.2), we obtain

$$S_{i+}S_{i-} = \left(2S - a_i^\dagger a_i\right)a_ia_i^\dagger \tag{2.3.12g}$$

$$\approx 2Sa_ia_i^\dagger \tag{2.3.12h}$$

to lowest order in the boson creation and/or annihilation operators.

With eq. (2.3.12h), we approximate

$$S_{i+} = \sqrt{2S}a_i \tag{2.3.13}$$

with corrections involving quadratic terms in a_i.

This results

$$\begin{aligned}\boldsymbol{S}_i &= \frac{1}{2}\left(\sqrt{2S}a_i + \sqrt{2S}a_i^\dagger\right)\hat{x} + \frac{1}{2i}\left(\sqrt{2S}a_i - \sqrt{2S}a_i^\dagger\right)\hat{y} + \left(S - a_i^\dagger a_i\right)\hat{z} \\ &= \frac{\sqrt{2S}}{2}\left(a_i + a_i^\dagger\right)\hat{x} + \frac{\sqrt{2S}}{2i}\left(a_i - a_i^\dagger\right)\hat{y} + \left(S - a_i^\dagger a_i\right)\hat{z}\end{aligned} \tag{2.3.14}$$

the boson spin operator element wise.

Finally, consider the dot-product between any two spins $\boldsymbol{A}$, $\boldsymbol{B}$

$$\boldsymbol{A}\cdot\boldsymbol{B} = A^x B^x + A^y B^y + A^z B^z \tag{2.3.15a}$$

in terms of the spin-flip operators eq. (2.3.5), this becomes

$$\begin{aligned}\boldsymbol{A}\cdot\boldsymbol{B} &= \left(\frac{1}{2}\left(A_+ + A_-\right)\right)\left(\frac{1}{2}\left(B_+ + B_-\right)\right) \\ &\quad + \left(\frac{1}{2i}\left(A_+ - A_-\right)\right)\left(\frac{1}{2i}\left(B_+ - B_-\right)\right) + A^z B^z \qquad (2.3.15b)\\ &= \frac{1}{4}\left(A_+B_- + A_-B_+\right) - \frac{1}{4}\left(-A_+B_- - A_-B_+\right) + A^z B^z \qquad (2.3.15c)\\ &= \frac{1}{2}\left(A_+B_- + A_-B_+\right) + A^z B^z \qquad (2.3.15d)\end{aligned}$$

in which the spin-flip operators and z-component of spins may be inserted in the specific case for further calculation.

2.4 Bogoliubov transformation

The Bogoliubov transformation is a powerful mathematical technique used to diagonalise the quantum mechanical Hamiltonian of a system [38]. In general, we seek to obtain the diagonalised Hamiltonian to describe the eigenstates of the uncoupled system. Moreover, this diagonal representation significantly simplifies the analysis and interpretation of the system's properties and behaviours.

We extend the Bogoliubov transformation in [38] to a framework that diagonalises a system of m bosons. The Bogoliubov Hamiltonian in momentum representation is given by

$$\mathcal{H} = \sum_{i,j,\boldsymbol{q}}\left[\lambda^1_{ij}a^\dagger_{\boldsymbol{q},i}a_{\boldsymbol{q},j} + \lambda^2_{ij}a^\dagger_{\boldsymbol{q},i}a^\dagger_{-\boldsymbol{q},j} + \lambda^3_{ij}a_{-\boldsymbol{q},i}a_{\boldsymbol{q},j} + \lambda^4_{ij}a_{-\boldsymbol{q},i}a^\dagger_{-\boldsymbol{q},j}\right], \tag{2.4.1}$$

where $i,j \in [1,m]$. In matrix notation, the Hamiltonian for any given $\boldsymbol{q}$ may be written as

$$\mathcal{H}_{\boldsymbol{q}} = \langle\alpha|\,\boldsymbol{\Lambda}\,|\alpha\rangle\,, \tag{2.4.2}$$

where the momentum dependence is implicit in the $2m$-dimensional basis vector, defined as follows

$$|\alpha\rangle = \begin{pmatrix}|a_{\boldsymbol{q}}\rangle\\ \left|a^\dagger_{-\boldsymbol{q}}\right\rangle\end{pmatrix} = \begin{pmatrix}a_{\boldsymbol{q},1}\\ \vdots\\ a_{\boldsymbol{q},m}\\ a^\dagger_{-\boldsymbol{q},1}\\ \vdots\\ a^\dagger_{-\boldsymbol{q},m}\end{pmatrix}; \tag{2.4.3a}$$

$$\langle\alpha| = |\alpha\rangle^\dagger = \begin{pmatrix}\left\langle a^\dagger_{\boldsymbol{q}}\right| & \langle a_{-\boldsymbol{q}}|\end{pmatrix} = \begin{pmatrix}a^\dagger_{\boldsymbol{q},1} & \cdots & a^\dagger_{\boldsymbol{q},m} & a_{-\boldsymbol{q},1} & \cdots & a_{-\boldsymbol{q},m}\end{pmatrix}. \tag{2.4.3b}$$

The $2m \times 2m$ block matrix

$$\boldsymbol{\Lambda} = \begin{pmatrix} \boldsymbol{\lambda^1} & \boldsymbol{\lambda^2} \\ \boldsymbol{\lambda^3} & \boldsymbol{\lambda^4} \end{pmatrix}, \tag{2.4.4}$$

with elements λ^n_{ij} will hereby be referred to as the grand-dynamical matrix [39]. We require this grand-dynamical matrix to be Hermitian with positive, real eigenvalues [39, p. 333].

We diagonalise this Hamiltonian in eq. (2.4.2) by a unitary basis transformation $\boldsymbol{T}$ of the boson operators. This is the Bogoliubov transformation. Write

$$\begin{aligned} \mathcal{H}_{\boldsymbol{q}} &= \langle\alpha| \boldsymbol{\Lambda} |\alpha\rangle \\ &= \left\langle \alpha \middle| \boldsymbol{T}^\dagger \boldsymbol{T}^{-\dagger} \boldsymbol{\Lambda} \boldsymbol{T}^{-1} \boldsymbol{T} \middle| \alpha \right\rangle \\ &\equiv \langle\beta| \boldsymbol{\Omega} |\beta\rangle , \end{aligned} \tag{2.4.5}$$

with the diagonalised matrix

$$\begin{aligned} \boldsymbol{\Omega} &= \boldsymbol{T}^{-\dagger} \boldsymbol{\Lambda} \boldsymbol{T}^{-1} \\ &= \frac{1}{2} \operatorname{diag}(\omega_1, \ \cdots, \ \omega_{2m}) , \end{aligned} \tag{2.4.6}$$

of the magnon modes ω_γ positive, sorted such that $\omega_\gamma = \omega_{\gamma+m}$. The new basis $|\beta\rangle$ is defined by

$$|\beta\rangle = \boldsymbol{T} |\alpha\rangle = \begin{pmatrix} |b_{\boldsymbol{q}}\rangle \\ \\ \left|b^\dagger_{-\boldsymbol{q}}\right\rangle \end{pmatrix}, \tag{2.4.7}$$

using the same notation as in eq. (2.4.3). The positive-definiteness of $\boldsymbol{\Lambda}$ implies that the new basis $|\beta\rangle$ is of the same form as the original basis $|\alpha\rangle$, i.e., the system consists of m bosonic modes.

Physically, the new boson operators $b_{\boldsymbol{q},\gamma}$ represent long-lived magnons in the SPFMI. Therefore, these operators must satisfy the bosonic commutation relations in eq. (2.3.2). Generalising the bosonic commutation relation to m bosons, gives [28]

$$|\beta\rangle \langle\beta| - \left(|\beta^*\rangle \langle\beta^*| \right)^T = \boldsymbol{\sigma}^z_m \equiv \begin{pmatrix} \mathbb{1}_m & 0_m \\ 0_m & -\mathbb{1}_m \end{pmatrix}. \tag{2.4.8}$$

Note that $|\beta^*\rangle^T \neq |\beta\rangle^\dagger = \langle\beta|$. Moreover, $\boldsymbol{\sigma}^z_m = \boldsymbol{\sigma}^z \otimes \mathbb{1}_m$ is the para-unit matrix [39, p. 423] and resembles the Pauli z-matrix $\boldsymbol{\sigma}^z$ generalised to $2m$ dimensions, hence the chosen notation. Here, the notation $\mathbb{1}_m$ and 0_m represents the $m \times m$ unit- and null- matrices, respectively.

From the requirement in eq. (2.4.8), we may insert for $|\beta\rangle$ and its adjoint from eq. (2.4.7) to obtain

$$\boldsymbol{T}^\dagger \boldsymbol{\sigma}^z_m = \boldsymbol{\sigma}^z_m \boldsymbol{T}^{-1}. \tag{2.4.9}$$

Consequently, we say that $\boldsymbol{T}$ is a para-unitary matrix.

The diagonalised matrix in eq. (2.4.6) must conform to this requirement on the Bogoliubov transformation matrix $\boldsymbol{T}$; isolating $\boldsymbol{T}^{\dagger}$ in eq. (2.4.9) and inserting into eq. (2.4.6), eventually gives

$$\boldsymbol{\sigma}_m^z \boldsymbol{\Lambda} \boldsymbol{T}^{-1} = \boldsymbol{T}^{-1} \boldsymbol{\mathcal{M}}, \tag{2.4.10}$$

for $\boldsymbol{\mathcal{M}} = \boldsymbol{\sigma}_m^z \boldsymbol{\Omega} = \boldsymbol{\Omega} \boldsymbol{\sigma}_m^z$ diagonal. Consider then eq. (2.4.10) for any column of index γ of $\boldsymbol{T}^{-1}$, $|\tau_\gamma\rangle$. As the matrix $\boldsymbol{\mathcal{M}}$ is diagonal, we may write eq. (2.4.10) to the following

$$\left(\boldsymbol{\sigma}_m^z \boldsymbol{\Lambda} - \boldsymbol{\mathcal{M}}_\gamma \mathbb{1}_{2m}\right) |\tau_\gamma\rangle = 0; \quad \gamma = 1, 2, \cdots, 2m. \tag{2.4.11}$$

Note that solving eq. (2.4.11) is equivalent to solving $2m$ eigenproblems. However, numerical issues arose by solving this eigensystem for the magnon spectrum and Bogoliubov transformation matrix. Alternatively, we follow Colpa's diagonalisation scheme [39]. As the grand-dynamical matrix is positive-definite, we write its Cholesky decomposition

$$\boldsymbol{\Lambda} = \boldsymbol{\mathcal{K}}^{\dagger} \boldsymbol{\mathcal{K}}, \tag{2.4.12}$$

for $\boldsymbol{\mathcal{K}}$ non-singular $2m$-dimensional upper triangular matrix. We may write the matrix $\boldsymbol{\mathcal{M}}$ in terms of $\boldsymbol{\mathcal{K}}$ as follows

$$\boldsymbol{\mathcal{M}} = \boldsymbol{\mathcal{U}}^{-1} \boldsymbol{\mathcal{K}} \boldsymbol{\sigma}_m^z \boldsymbol{\mathcal{K}}^{\dagger} \left(\boldsymbol{\mathcal{U}}^{\dagger}\right)^{-1}, \tag{2.4.13}$$

with $\boldsymbol{\mathcal{U}}$ such that

$$\boldsymbol{T}^{-1} \equiv \boldsymbol{\mathcal{K}}^{-1} \boldsymbol{\mathcal{U}} \boldsymbol{\Omega}^{1/2}. \tag{2.4.14}$$

In other words, we diagonalise the matrix $\boldsymbol{\mathcal{K}} \boldsymbol{\sigma}_m^z \boldsymbol{\mathcal{K}}^{\dagger}$ to obtain the eigenvalues $\boldsymbol{\mathcal{M}}_\gamma$ in $\boldsymbol{\mathcal{M}}$ and eigenvectors $|\mathfrak{u}_\gamma\rangle$ in $\boldsymbol{\mathcal{U}}$. Thereby, we calculate the magnon spectrum from $\boldsymbol{\Omega} = \boldsymbol{\sigma}_m^z \boldsymbol{\mathcal{M}}$; and the inverse Bogoliubov transformation $\boldsymbol{T}^{-1}$ from eq. (2.4.14). From the latter, we may proceed to derive the long-lived magnon operators.

As a consequence of the para-unitarity of $\boldsymbol{T}$, we write the inverse of the Bogoliubov transformation matrix

$$\boldsymbol{T}^{-1} = \begin{pmatrix} |\tau_1\rangle & |\tau_2\rangle & \cdots & |\tau_{2m}\rangle \end{pmatrix} \tag{2.4.15a}$$

$$= \begin{pmatrix} \boldsymbol{U}_{\boldsymbol{q}} & \boldsymbol{V}_{\boldsymbol{q}} \\ \boldsymbol{V}_{-\boldsymbol{q}}^{*} & \boldsymbol{U}_{-\boldsymbol{q}}^{*} \end{pmatrix}, \tag{2.4.15b}$$

as a block matrix, motivated by the "textbook" u/v-notation as often used for calculations of the traditional single-bosonic mode. Note that the columns $\boldsymbol{T}^{-1}$, i.e. the eigenvectors $|\tau_\gamma\rangle$ of eq. (2.4.11), are not unique and may be accompanied by any phase factor $e^{i\theta_\gamma}$.

Eventually, the old boson operators may be written as linear combinations of the long-lived boson operators. With the form of $\boldsymbol{T}^{-1}$ in eq. (2.4.15b), these operators

transform as

$$a_{\boldsymbol{q}i} = \sum_{\gamma=1}^{m} \left(u_{\boldsymbol{q}i\gamma} b_{\boldsymbol{q}\gamma} + v_{\boldsymbol{q}i\gamma} b^{\dagger}_{-\boldsymbol{q}\gamma} \right), \tag{2.4.16a}$$

$$a^{\dagger}_{-\boldsymbol{q}i} = \sum_{\gamma=1}^{m} \left(v^{*}_{-\boldsymbol{q}i\gamma} b_{\boldsymbol{q}\gamma} + u^{*}_{-\boldsymbol{q}i\gamma} b^{\dagger}_{-\boldsymbol{q}\gamma} \right), \tag{2.4.16b}$$

where $|a_{\boldsymbol{q}}\rangle$ include all types of bosons, and $|b_{\boldsymbol{q}}\rangle$ include all boson modes.

Lastly, one must note that a numerical solve of eigenvalues and corresponding eigenvectors will in general fail to provide orthogonal eigenvectors for degenerate eigenvalues. For this purpose, we implement the Gram-Schmidt method of orthonormalising a set of vectors. The procedure is as follows: For a set of degenerate eigenvalues $\{\omega_\gamma\}$, let the set of corresponding eigenvectors be $\{|\mathfrak{u}_\gamma\rangle\}$. Then, the new set of orthogonal eigenvectors $\{|e_\gamma\rangle\}$ is obtained by

$$|e_1\rangle = |\mathfrak{u}_1\rangle \tag{2.4.17a}$$

$$\left|e^{(1)}_{\gamma}\right\rangle = |\mathfrak{u}_\gamma\rangle - \mathrm{proj}_{|e_1\rangle}\left(|\mathfrak{u}_\gamma\rangle\right); \qquad \gamma > 1 \tag{2.4.17b}$$

$$\left|e^{(i)}_{\gamma}\right\rangle = \left|e^{(i-1)}_{\gamma}\right\rangle - \mathrm{proj}_{|e_i\rangle}\left(\left|e^{(i-1)}_{\gamma}\right\rangle\right); \qquad i = 2, 3, \cdots, \gamma - 1 \tag{2.4.17c}$$

where $\mathrm{proj}_{|u\rangle}(|v\rangle)$ is the projection of $|v\rangle$ onto $|u\rangle$, defined by

$$\mathrm{proj}_{|u\rangle}(|v\rangle) = |u\rangle \frac{\langle u| \boldsymbol{\sigma}^z_m |v\rangle}{\langle u| \boldsymbol{\sigma}^z_m |u\rangle}. \tag{2.4.18}$$

2.5 *Schrieffer-Wolff transformation

We seek to express the Hamiltonian purely in terms of free particles and effective interactions between electrons, to obtain the system in terms of Cooper pairs. In this section, we thereby consider a relevant Hamiltonian to our system, as will be confirmed in section 3.3. To obtain the Hamiltonian in the desired form purely in terms of electrons, we apply the Schrieffer-Wolff transformation.

The Schrieffer-Wolff transformation is a unitary basis transformation by the time-independent operator ξ. Essentially, the axes of the Hilbert space are rotated, leaving the eigenvectors rotated and the eigenvalues unchanged.

Thereby, let $\mathcal{H}$ be the Hamiltonian of a system with free and interacting fermions and bosons. We must write this Hamiltonian only in terms of fermions to obtain an effective fermion interaction model. For this purpose, consider the interaction term as a perturbation to the free-particle terms, such that

$$\mathcal{H} = \mathcal{H}_0 + \lambda \mathcal{H}_1, \tag{2.5.1}$$

in which $\mathcal{H}_0$ is the free particle term, and $\lambda\mathcal{H}_1$ is the interaction term for the smallness parameter λ. Note that this interaction term is linear in boson operators for our relevance.

Proceed to introduce the Schrieffer-Wolff transformation; a unitary basis transformation by the time-independent generator ξ, giving the effective interaction Hamiltonian

$$\mathcal{H}_{\text{eff}} = e^{-\xi}\mathcal{H}e^{\xi}, \tag{2.5.2}$$

for which we require the special case of $\lambda\mathcal{H}_1 = 0$ to give $\mathcal{H}_{\text{eff}} \overset{!}{=} \mathcal{H}_0$, i.e., ξ must also be zero. Therefore, we conclude that termwise

$$\xi \sim \lambda\mathcal{H}_1, \tag{2.5.3}$$

and redefine $\xi \to \lambda\xi$ to indicate its smallness. Thereby, we use the Baker-Campbell-Hausdorff formula [40] to expand this effective Hamiltonian. Truncating terms beyond $\mathcal{O}(\lambda^2)$, this gives

$$\mathcal{H}_{\text{eff}} \approx \mathcal{H}_0 + \lambda\mathcal{H}_1 - \lambda\left[\xi,\ \mathcal{H}_0\right] - \lambda^2\left[\xi,\ \mathcal{H}_1\right] + \frac{\lambda^2}{2}\left[\xi,\ \left[\xi,\ \mathcal{H}_0\right]\right]. \tag{2.5.4}$$

Note then that the terms linear in the boson operator, i.e., ξ and $\mathcal{H}_1$, are also linear in λ the smallness parameter. To obtain the effective Hamiltonian purely in terms of fermion operators, the terms linear in boson operators must be eliminated. We achieve this by choosing ξ such that the terms linear in λ cancel. Thus, we must require

$$\lambda\mathcal{H}_1 - \lambda\left[\xi,\ \mathcal{H}_0\right] \overset{!}{=} 0, \tag{2.5.5}$$

which concurs with the requirement in eq. (2.5.3). With this, the effective Hamiltonian may be written

$$\mathcal{H}_{\text{eff}} = \mathcal{H}_0 - \frac{\lambda^2}{2}\left[\xi,\ \mathcal{H}_1\right], \tag{2.5.6}$$

in which the last term represents $\mathcal{H}_{\text{pair}}$ the effective fermion-fermion pair interaction. This concludes the Schrieffer-Wolff transformation in its general form.

For later convenience, a summary of the Schrieffer-Wolff transformation is presented. We begin with writing $\mathcal{H} = \mathcal{H}_0 + \mathcal{H}_1$ for our system of free ($\mathcal{H}_0$) and interacting ($\mathcal{H}_1$) fermions and bosons. Thus, the effective pair interaction of fermions is obtained by the commutator consisting of the perturbation $\mathcal{H}_1$ and the generator ξ. The perturbation $\mathcal{H}_1$ is known, while the generator ξ may be obtained from the requirement in eq. (2.5.5). Following this procedure will give the effective fermion-fermion pair interaction Hamiltonian in terms of the corresponding pair potential.

3 Bilayer model

In this chapter, we present the relevant models for our bilayer system. This bilayer consists of two monoatomic layers: the tight binding normal metal (NM) and the coplanar non-collinear spiral-phase ferromagnetic insulator (SPFMI). We let both have a triangular lattice structure, and assume a lattice matched bilayer for simplicity. The cross-section of this bilayer is illustrated in fig. 3.1, while the SPFMI monolayer is illustrated in fig. 3.2.

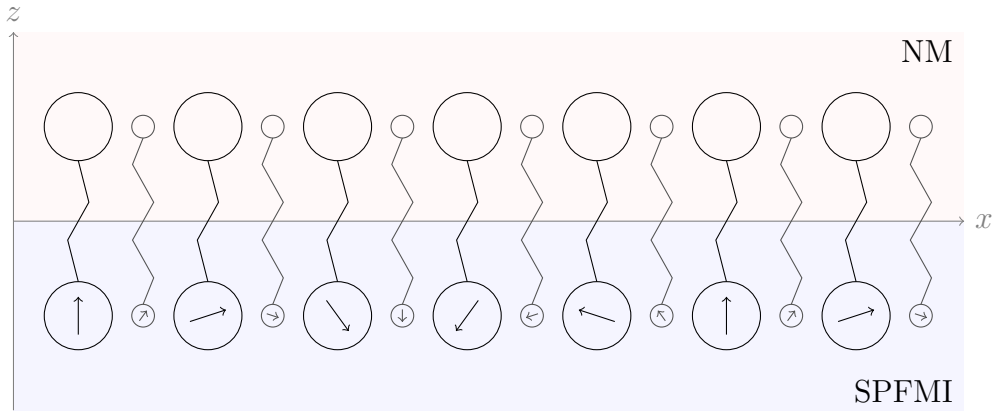

Figure 3.1: A simplified side-view of the bilayer of interest with NM as the top layer, and SPFMI as the bottom layer. Illustrated are the matched lattice sites illustrated as circles, with an exchange interaction across the interface illustrated as crooked lines. Every second site in each monolayer is drawn smaller to illustrate depth, necessary due to the triangular lattice structure. The $\hat{x}$-axis is indicated to the horisontal along the monolayers, while the $\hat{z}$-axis to the vertical transverse on the bilayer. The lattice site arrows in the SPFMI indicate the spiral-phase spin structure, and is obtained in section 5.2.

First, we introduce the NM layer in section 3.1 and present its Hamiltonian. We then derive the ground state energy, and the density of states. Second, we consider the SPFMI in section 3.2, eventually obtaining the Hamiltonian in terms of magnon operators. At last, we investigate the exchange interaction at the bilayer interface in section 3.3.

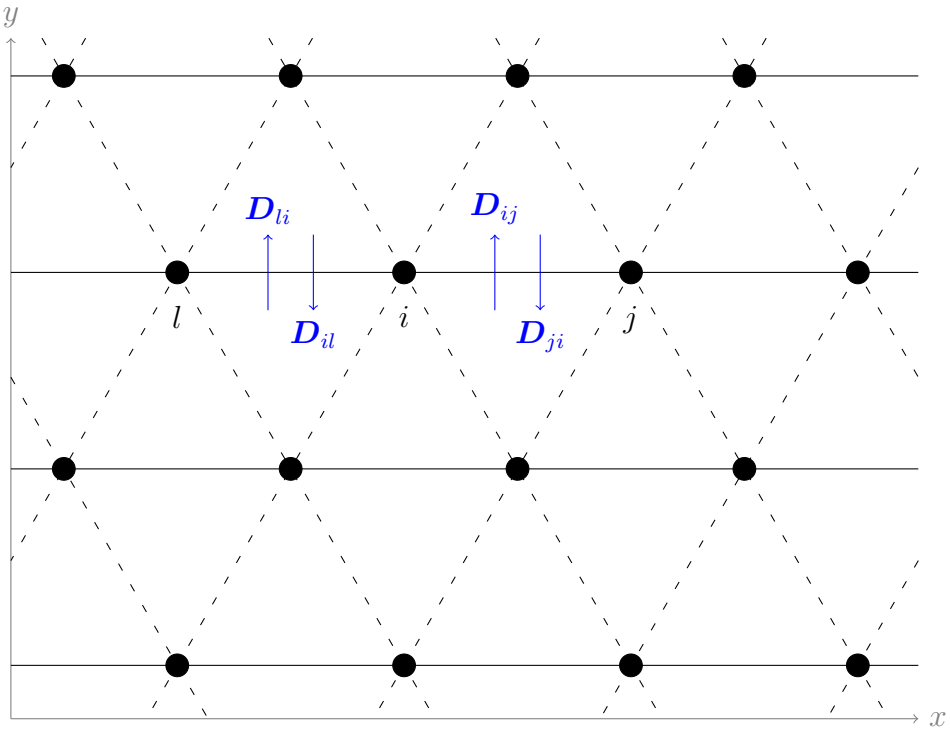

Figure 3.2: A simplified top-view of the SPFMI monolayer. Illustrated is the triangular lattice, with its sites drawn as filled circles. At each site is a spin, excluded from the illustration to minimise visual clutter. Three reference sites l, i, and j are denoted along the same chain parallel with the $\hat{x}$-axis. The DMI is between nearest neighbours along the same chain, pointing in the $\pm\hat{y}$-direction. The blue arrows illustrate the DMI-vector between the reference sites, given by $\boldsymbol{D}_{ij} = D\cos\varphi_{ij}\hat{y}$ for φ_{ij} the angle that the line parallel with $\hat{x}$ going through site i makes with the line connecting the neighbouring sites i and j. The dashed lines connecting the lattice sites indicate the presence of spin coupling, while the solid lines represent the additional presence of DMI. The lattice is periodic, and therefore the interaction lines continue beyond the delimited lattice view. The $\hat{x}$-axis is indicated to the horisontal, while the $\hat{y}$-axis is indicated to the vertical. The correspondence between the illustrated interactions and our system will become clear in chapter 5.

3.1 Normal metal model

Consider first the normal metal (NM) of the bilayer, described by the tight-binding model. In this model, the electrons at any lattice site i may only jump to the nearest neighbouring lattice site j. A simple model Hamiltonian for this NM is thus

$$\mathcal{H}_{\mathrm{NM}} = -\sum_{\langle i,j\rangle,\sigma} t_{ij} c_{i\sigma}^{\dagger} c_{j\sigma} - \mu \sum_{i,\sigma} c_{i\sigma}^{\dagger} c_{i\sigma}, \tag{3.1.1}$$

where t_{ij} is the hopping probability to lattice site i from j, and μ is the chemical potential. Here, the site energy $\epsilon_i = 0$ was set to be the reference energy.

The Hamiltonian in eq. (3.1.1) is diagonalised by a Fourier transformation to momentum space. With N lattice sites on each monolayer, let the fermion operators transform as follows

$$c_{i\sigma} = \frac{1}{\sqrt{N}} \sum_{\boldsymbol{k}} c_{\boldsymbol{k}\sigma} e^{-i\boldsymbol{k}\cdot\boldsymbol{r}_i}, \tag{3.1.2}$$

and correspondingly for the adjoint $c_{i\sigma}^{\dagger}$. After some algebra, the Hamiltonian in eq. (3.1.1) becomes

$$\mathcal{H}_{\mathrm{NM}} = \sum_{\boldsymbol{k},\sigma} \tilde{\epsilon}_{\boldsymbol{k}} c_{\boldsymbol{k}\sigma}^{\dagger} c_{\boldsymbol{k}\sigma}, \tag{3.1.3}$$

which is now diagonalised in terms of the fermion operators in momentum representation. The electron dispersion relation is given by

$$\tilde{\epsilon}_{\boldsymbol{k}} = \epsilon_{\boldsymbol{k}} - \mu, \tag{3.1.4}$$

in which

$$\epsilon_{\boldsymbol{k}} = -\frac{1}{N} \sum_{\langle i,j\rangle} t_{ij} \mathfrak{Re}(e^{-i\boldsymbol{k}\cdot\boldsymbol{\delta}_{ij}}), \tag{3.1.5}$$

for $\boldsymbol{\delta}_{ij}$ the nearest-neighbour vector from site i to any nearest neighbouring site j. For our triangular lattice, corresponding to that sketched in fig. 3.2 with lattice parameter a, the nearest-neighbour vector becomes

$$\boldsymbol{\delta}_{ij} = a\left(\cos\phi_{ij}\hat{x} + \sin\phi_{ij}\hat{y}\right), \tag{3.1.6}$$

for ϕ_{ij} the angle between the nearest-neighbour vector $\boldsymbol{\delta}_{ij}$ and the positive $\hat{x}$-axis.

Summing over nearest neighbours j for some i, eq. (3.1.5) becomes

$$\epsilon_{\boldsymbol{k}} = -\frac{1}{N}\sum_i \Bigg[\cos(k_x a)\,(t_{i,i-1} + t_{i,i+1}) + \cos\left(\frac{1}{2}k_x a\right)\cos\left(\frac{\sqrt{3}}{2}k_y a\right)(t_{i,i-N_x} + t_{i,i+N_x+1} + t_{i,i-N_x+1} + t_{i,i+N_x}) + \sin\left(\frac{1}{2}k_x a\right)\sin\left(\frac{\sqrt{3}}{2}k_y a\right)(t_{i,i-N_x} + t_{i,i+N_x+1} - t_{i,i-N_x+1} - t_{i,i+N_x})\Bigg], \tag{3.1.7}$$

for N_x number of lattice sites along $\hat{x}$. Note that the electron dispersion $\epsilon_{\boldsymbol{k}} = \epsilon_{-\boldsymbol{k}}$ is inversion symmetric in momentum due to its sinusoidal dependence on the momentum components.

We continue to derive the density of states (DoS) for electrons, starting with [1]

$$D(\epsilon) = 2\sum_{\boldsymbol{k}} \delta(\epsilon - \epsilon_{\boldsymbol{k}}), \tag{3.1.8}$$

where the factor 2 originates from the spin-independent electron dispersion. This expression may be rewritten to integral form, giving [1]

$$D(\epsilon) = \frac{2N}{A_{\text{eBZ}}}\int_{-\pi}^{\pi} \mathrm{d}\theta \int_0^{c(\theta)} \mathrm{d}k k \delta(\epsilon - \epsilon_{k,\theta}), \tag{3.1.9}$$

with our $\epsilon_{k,\theta}$ given in eq. (3.1.7), in which $k_x = k\cos\theta$ and $k_y = k\sin\theta$. Moreover, $c(\theta)$ is the cutoff-function ensuring that $\boldsymbol{k}$ is confined to the electron Brillouin zone (eBZ). Due to the triangular lattice structure, the eBZ is hexagonal. Thus, the cutoff-function is given by

$$c(\theta) = \frac{s}{1 + \frac{2/\sqrt{3}-1}{\sqrt{2}-1}\left(\left|\sin\frac{3\theta}{2}\right| + \left|\cos\frac{3\theta}{2}\right| - 1\right)}, \tag{3.1.10}$$

where $s = \frac{4\pi}{3}$ is the length of the eBZ edges, giving $A_{\text{eBZ}} = \frac{3\sqrt{3}}{2}s^2$ the area of the eBZ.

Analytically, we may solve the DoS as a function of momentum $\boldsymbol{k}$ by using $D(\epsilon)\,\mathrm{d}\epsilon = D(k)\,\mathrm{d}k$. Solving the integral in eq. (3.1.9) under this transformation gives

$$D(k) = \frac{\sqrt{3}}{2\pi}Nk, \tag{3.1.11}$$

after inserting for A_{eBZ}.

On the other hand, the DoS as a function of the energies ϵ must be solved numerically. We start with writing out the δ function. In general, any function $f(k)$ with roots $\{k_i\}$ such that $f'(k_i) \neq 0$ will satisfy

$$\delta[f(k)] = \sum_i \frac{\delta(k - k_i)}{|f'(k_i)|}. \tag{3.1.12}$$

By inspection of eq. (3.1.9), we note that $f(k) = \epsilon - \epsilon_{k,\theta}$. Thereby, insert the identity eq. (3.1.12) into the DoS eq. (3.1.9) to obtain

$$D(\epsilon) = \frac{2N}{A_{\text{eBZ}}} \int_0^{2\pi} \mathrm{d}\theta \sum_i \frac{k_i(\theta)}{|f'[k_i(\theta)]|}. \tag{3.1.13}$$

This quantity is solved and plotted for in section 5.1 after applying some simplifications.

3.2 Spiral-phase ferromagnetic insulator model

The magnet of the bilayer in consideration is a spiral-phase ferromagnetic insulator (SPFMI). In this system, the magnetic ground state spin-structure makes a spiral structure, determined by the interplay of various terms [1]: the Dzyaloshinskii-Moriya interaction (DMI), the exchange interaction, and the easy axis anisotropy. The DMI is a relativistic effect arising from spin-orbit coupling (SOC), i.e., the the crystal symmetry determines the nature of the DMI-vectors $\boldsymbol{D}_{ij}$ [41, 42]. In the presence of DMI, an anti-symmetric exchange interaction is introduced between neighbouring spins in the magnet, thus favouring a spin canting phase.

Moreover, the exchange interaction $J_{ij}^{\alpha\beta}$ couples spin at nearest-neighbouring lattice sites i, j, and is thus written as a Heisenberg exchange interaction [43, p. 226]. This coupling affects the orientation of the spins in various ways depending on its presence in the system.

The easy-axis anisotropy is a magnetic anisotropy promoting an alignment of magnetic moments along the easy-axis [44]. If the governing anisotropy constant K is sufficiently large, the easy-axis is the energetically favourable direction of spontaneous magnetisation.

Generally, the model Hamiltonian for this SPFMI may be written

$$\mathcal{H}_{\text{MF}} = \mathcal{H}_{\text{ex}} + \mathcal{H}_{\text{DMI}} + \mathcal{H}_{\text{ani}}, \tag{3.2.1}$$

in which

$$\mathcal{H}_{\text{ex}} = - \sum_{\substack{\langle i,j\rangle, \\ \alpha,\beta\in\{x,y,z\}}} J_{ij}^{\alpha\beta} S_i^\alpha S_j^\beta, \tag{3.2.2a}$$

$$\mathcal{H}_{\text{DMI}} = - \sum_{\langle i,j\rangle} \boldsymbol{D}_{ij} \cdot (\boldsymbol{S}_i \times \boldsymbol{S}_j), \tag{3.2.2b}$$

$$\mathcal{H}_{\text{ani}} = -K \sum_i (S_i^z)^2. \tag{3.2.2c}$$

It is clear from eq. (3.2.2) that the canting of spins in our SPFMI arise from an interplay of the DMI vectors $\boldsymbol{D}_{ij}$ favouring perpendicular neighbouring spins; and the easy-axis anisotropy favouring collinear spins. The effect of the exchange interaction depends on the coupling strength $J_{ij}^{\alpha\beta}$ for various indices.

The SPFMI Hamiltonian in eq. (3.2.1) may be written more compactly as follows

$$\mathcal{H}_{\mathrm{FM}} = -\sum_{\langle i,j\rangle} \boldsymbol{S}_i^T \mathbf{H}_{ij} \boldsymbol{S}_j - K \sum_i \left(S_i^z\right)^2, \tag{3.2.3}$$

with the interaction matrix

$$\mathbf{H}_{ij} = \begin{pmatrix} J_{ij}^x & D_{ij}^z + J_{ij}^{xy} & -D_{ij}^y + J_{ij}^{xz} \\ -D_{ij}^z + J_{ij}^{yx} & J_{ij}^y & D_{ij}^x + J_{ij}^{yz} \\ D_{ij}^y + J_{ij}^{zx} & -D_{ij}^x + J_{ij}^{zy} & J_{ij}^z \end{pmatrix}. \tag{3.2.4}$$

From inspection of this matrix, we note that the DMI is the anti-symmetric contribution to the exchange interaction $J_{ij}^{\alpha\beta}$.

Moreover, the SPFMI Hamiltonian is second quantized by the HP transformation in eqs. (2.3.11) and (2.3.13). However, due to the non-collinearity of spins, the HP transformation may only be applied after a rotation of each lattice-spin operator S_i^α from the global spin coordinate system, to the local spin coordinate system of the corresponding lattice site. The rotated spin operator for each lattice site i is written

$$\widetilde{\boldsymbol{S}}_i = \boldsymbol{U}_i \boldsymbol{S}_i, \tag{3.2.5}$$

for the components $\widetilde{S}_i^\alpha$ satisfying the HP transformations, such that

$$\begin{aligned} \widetilde{S}_i^z &= S - a_i^\dagger a_i, \\ \widetilde{S}_{i+} = \widetilde{S}_{i-}^\dagger &\approx \sqrt{2S} a_i, \end{aligned} \tag{3.2.6}$$

as was derived in section 2.3. Furthermore, the matrix $\boldsymbol{U}_i$ is the unitary rotation matrix

$$\boldsymbol{U}_i = \begin{pmatrix} \cos\vartheta_i \cos\psi_i & \cos\vartheta_i \sin\psi_i & -\sin\vartheta_i \\ -\sin\psi_i & \cos\psi_i & 0 \\ \sin\vartheta_i \cos\psi_i & \sin\vartheta_i \sin\psi_i & \cos\vartheta_i \end{pmatrix}, \tag{3.2.7}$$

with ϑ_i the polar angle and ψ_i the azimuthal angle of the spin at site i relative the global coordinate system. These angles are determined by the classical ground state.

Thereby, the SPFMI Hamiltonian in eq. (3.2.3) is written in terms of the rotated spins to give

$$\mathcal{H}_{\mathrm{FM}} = -\sum_{\langle i,j\rangle} \widetilde{\boldsymbol{S}}_i^T \boldsymbol{W}_{ij} \widetilde{\boldsymbol{S}}_j - K \sum_i \left(\boldsymbol{U}_i^T \widetilde{\boldsymbol{S}}_i\right)_z^2, \tag{3.2.8}$$

with the rotated interaction matrix

$$\boldsymbol{W}_{ij} = \left\{W_{ij}^{\alpha\beta}\right\} = \boldsymbol{U}_i \mathbf{H}_{ij} \boldsymbol{U}_j^T. \tag{3.2.9}$$

For later convenience, the lengthy elements $W_{ij}^{\xi\xi'}$ are presented in appendix A.1.

We may proceed to write the $\mathcal{H}_{\mathrm{FM}}$ in terms of the boson ladder operators $a_i^{(\dagger)}$. To achieve this, we begin to write out the matrix multiplication in eq. (3.2.8). Then, we insert for $S_i^{x/y}$ in terms of $S_{i+/-}$ as given in eq. (2.3.5). At last we use the

HP transformation in eq. (3.2.6). This procedure is easily done in mathematical computation softwares such as Maple [45] and Mathematica [46]. We write

$$\mathcal{H}_{\mathrm{FM}} \approx \mathcal{H}_{\mathrm{FM}}^{(0)} + \mathcal{H}_{\mathrm{FM}}^{(1)} + \mathcal{H}_{\mathrm{FM}}^{(2)}, \tag{3.2.10}$$

where $\mathcal{H}_{\mathrm{FM}}^{(n)}$ is of order n in the boson operators. We truncate at second order in boson operators as the scope of this report only includes linear spin-wave theory, and henceforth write the above approximation as an equality.

Constant term Hamiltonian

The classical ground state of the system is obtained by minimising the constant term Hamiltonian. This Hamiltonian is given by

$$\mathcal{H}_{\mathrm{FM}}^{(0)} = -S^2 \sum_{\langle i,j \rangle} W_{ij}^{zz} - KS^2 \sum_i \cos^2 \vartheta_i. \tag{3.2.11}$$

However, simplifications must be introduced to analytically derive the ground state. This is done in section 5.2, where we set the system to have null easy-axis anisotropy.

First order Hamiltonian

The first order Hamiltonian is linear in the boson operators $a_i^{(\dagger)}$, given by

$$\begin{aligned} \mathcal{H}_{\mathrm{FM}}^{(1)} = &- S\sqrt{\frac{S}{2}} \sum_{\langle i,j \rangle} \Big\{ W_{ij}^{xz} \left(a_i^\dagger + a_i \right) + W_{ij}^{zx} \left(a_j^\dagger + a_j \right) \\ &\qquad + i \left[W_{ij}^{yz} \left(a_i^\dagger - a_i \right) + W_{ij}^{zy} \left(a_j^\dagger - a_j \right) \right] \Big\} \\ &+ KS\sqrt{\frac{S}{2}} \sum_i \sin 2\vartheta_i \left(a_i^\dagger + a_i \right). \end{aligned} \tag{3.2.12}$$

Note that the ground state requirement implies that the derivative of $\mathcal{H}_{\mathrm{FM}}^{(1)}$ with respect to $a_i^{(\dagger)}$ must be null. Observe therefore that the derivative of eq. (3.2.12) with respect to either of the boson operators yield the same result. For this reason, consider only derivatives of $\mathcal{H}_{\mathrm{FM}}^{(1)}$ with respect to $a_i^\dagger$ for any one lattice site i. The real and imaginary parts of this derivative, respectively, gives

$$\underline{\mathfrak{Im}(\cdot):} \quad \sum_{\langle j \rangle} \left(W_{ij}^{yz} + W_{ji}^{zy} \right) = 0, \tag{3.2.13a}$$

$$\underline{\mathfrak{Re}(\cdot):} \quad \sum_{\langle j \rangle} \left(W_{ij}^{xz} + W_{ji}^{zx} \right) = K \sin 2\vartheta_i, \tag{3.2.13b}$$

which should be equivalent to ensuring that the spin angles ϑ_i, ψ_i correspond to the classical ground state. This is commented in chapter 5.

Second order Hamiltonian

The terms quadratic in the boson operators constitute the following expression

$$\begin{aligned}\mathcal{H}_{\mathrm{FM}}^{(2)} =& S\sum_{\langle i,j\rangle}\Big[C_{ij}^{1}a_i a_j + \left(C_{ij}^{1}\right)^{*} a_i^{\dagger}a_j^{\dagger} + C_{ij}^{2}a_i a_j^{\dagger} + \left(C_{ij}^{2}\right)^{*} a_i^{\dagger}a_j \\ &+ W_{ij}^{zz}\left(a_i^{\dagger}a_i + a_j^{\dagger}a_j\right)\Big] \\ &- \frac{1}{2}KS\sum_{i}\left[\left(a_i a_i + a_i^{\dagger}a_i^{\dagger} + a_i a_i^{\dagger}\right)\sin^2\vartheta_i + a_i^{\dagger}a_i\left(1-5\cos^2\vartheta_i\right)\right],\end{aligned} \tag{3.2.14}$$

in which the coefficients C_{ij}^{n} were defined accordingly

$$C_{ij}^{1} \equiv -\frac{1}{2}\left[W_{ij}^{xx} - W_{ij}^{yy} - i\left(W_{ij}^{xy} + W_{ij}^{yx}\right)\right], \tag{3.2.15}$$

$$C_{ij}^{2} \equiv -\frac{1}{2}\left[W_{ij}^{xx} + W_{ij}^{yy} + i\left(W_{ij}^{xy} - W_{ij}^{yx}\right)\right]. \tag{3.2.16}$$

The Hamiltonian in eq. (3.2.14) represents both spin-waves and localised spin fluctuations by the terms bilinear in $a_i^{\dagger},\ a_j$ or vice versa, and by the number operator $\eta_i = a_i^{\dagger}a_i$, respectively. Therefore, this formulation of the system will provide insight into the magnons of the SPFMI.

To obtain the magnon energy spectrum, the Hamiltonian $\mathcal{H}_{\mathrm{FM}}$ must be diagonalised. This is done in terms of the Bogoliubov transformationas presented in section 2.4. Therefore, we must first Fourier transform our Hamiltonian to a formulation in momentum space. Preceedingly, we exploit the symmetry of the triangular lattice structure to effectively analyse sub-lattices comprising solely of equally oriented spins.

Rewrite the lattice characterisation from site i to its position i' on the corresponding sub-lattice L. Similarly, the nearest neighbouring site j is characterised by its position j' on the corresponding sub-lattice T. Accordingly, the sum over $\langle i,j\rangle$ is replaced by summations over the nearest neighbouring positions $\langle i',j'\rangle$ and their corresponding sub-lattices $\langle L,T\rangle$, which must also be nearest-neighbours. Applying this transformation, gives

$$\begin{aligned}\mathcal{H}_{\mathrm{FM}}^{(2)} =& S\sum_{\langle i',j'\rangle}\sum_{\langle L,T\rangle}\Big[C_{i'j'LT}^{1}a_{i'L}a_{j'T} + \left(C_{i'j'LT}^{1}\right)^{*}a_{i'L}^{\dagger}a_{j'T}^{\dagger} \\ &+ C_{i'j'LT}^{2}a_{i'L}a_{j'T}^{\dagger} + \left(C_{i'j'LT}^{2}\right)^{*}a_{i'L}^{\dagger}a_{j'T} \\ &+ W_{ij}^{zz}\left(a_{i'L}^{\dagger}a_{i'L} + a_{j'T}^{\dagger}a_{j'T}\right)\Big] \\ &- \frac{1}{2}KS\sum_{i',L}\Big[\left(a_{i'L}a_{i'L} + a_{i'L}^{\dagger}a_{i'L}^{\dagger} + a_{i'L}a_{i'L}^{\dagger}\right)\sin^2\vartheta_L \\ &+ a_{i'L}^{\dagger}a_{i'L}\left(1-5\cos^2\vartheta_L\right)\Big],\end{aligned} \tag{3.2.17}$$

in which the angle $\vartheta_i \to \vartheta_L$ by the aforementioned definition of the sub-lattices: each site $i \in L$ exhibit equally oriented spin in the global spin coordinate system.

Moreover, we define the nearest-neighbour vector $\boldsymbol{\delta}_{LTj'}$ as the vector from any site on sub-lattice L to its nearest-neighbouring site positioned at j' on sub-lattice T. Note then that the coefficients $C^n_{i'j'LT} \to C^n_{LT}(\boldsymbol{\delta}_{LTj'})$ as neither the exchange coupling strength nor the DMI vector depends on the site within a sub-lattice, while the DMI vector does depend on the orientation of $\boldsymbol{\delta}_{LTj'}$.

Thus, we may continue to formulate the Hamiltonian in momentum space. The Fourier transformation of the boson operators is given by

$$a_{i'L} = \frac{1}{\sqrt{N_L}} \sum_{\boldsymbol{q}} a_{\boldsymbol{q}L} e^{-i\boldsymbol{q}\cdot\boldsymbol{r}_{i'}}, \tag{3.2.18}$$

for $\boldsymbol{q}$ the momentum state of bosons, and N_L the number of lattice sites in sub-lattice L. Under this transformation, the Hamiltonian in eq. (3.2.17) becomes

$$\begin{aligned}\mathcal{H}^{(2)}_{\mathrm{FM}} =& S \sum_{\langle L,T\rangle,\boldsymbol{q}} \Big[\Gamma^1_{LT}(\boldsymbol{q})\, a_{\boldsymbol{q}L} a_{-\boldsymbol{q}T} + \left(\Gamma^1_{LT}(\boldsymbol{q})\right)^* a^\dagger_{\boldsymbol{q}L} a^\dagger_{-\boldsymbol{q}T} \\ &\qquad + \Gamma^2_{LT}(\boldsymbol{q})\, a_{\boldsymbol{q}L} a^\dagger_{\boldsymbol{q}T} + \left(\Gamma^2_{LT}(\boldsymbol{q})\right)^* a^\dagger_{\boldsymbol{q}L} a_{\boldsymbol{q}T} + 2\zeta_{LT} a^\dagger_{\boldsymbol{q}L} a_{\boldsymbol{q}L} \Big] \\ &- \frac{1}{2} KS \sum_{\boldsymbol{q},L} \Big[\left(a_{\boldsymbol{q}L} a_{-\boldsymbol{q}L} + a^\dagger_{\boldsymbol{q}L} a^\dagger_{-\boldsymbol{q}L} + a_{\boldsymbol{q}L} a^\dagger_{\boldsymbol{q}L} \right) \sin^2\vartheta_L \\ &\qquad + a^\dagger_{\boldsymbol{q}L} a_{\boldsymbol{q}L} \left(1 - 5\cos^2\vartheta_L\right) \Big],\end{aligned} \tag{3.2.19}$$

after some algebra. The coefficients in eq. (3.2.19) are defined as

$$\Gamma^n_{LT}(\boldsymbol{q}) \equiv \sum_{j'} C^n_{LT}(\boldsymbol{\delta}_{LTj'})\, e^{i\boldsymbol{q}\cdot\boldsymbol{\delta}_{LTj'}}, \tag{3.2.20a}$$

$$\zeta_{LT} \equiv \sum_{j'} W^{zz}_{LT}(\boldsymbol{\delta}_{LTj'}), \tag{3.2.20b}$$

where we used that $W^{zz}_{ij} = W^{zz}_{ji}$ for $\boldsymbol{D}_{ij} = -\boldsymbol{D}_{ji}$.

We continue to write the Hamiltonian in eq. (3.2.19) more compactly on the form of a Bogoliubov Hamiltonian as presented in eq. (2.4.1). This is done using boson commutation relations, and expanding the sums to all lattice sites L, T. Thus, we get

$$\begin{aligned}\mathcal{H}^{(2)}_{\mathrm{FM}} = S \sum_{L,T,\boldsymbol{q}} \Big[&\nu_{LT}(\boldsymbol{q})\, a_{\boldsymbol{q}L} a_{-\boldsymbol{q}T} + \left(\nu_{LT}(\boldsymbol{q})\right)^* a^\dagger_{\boldsymbol{q}L} a^\dagger_{-\boldsymbol{q}T} \\ &+ \eta_{LT}(\boldsymbol{q})\, a_{\boldsymbol{q}L} a^\dagger_{\boldsymbol{q}T} + \left(\eta_{LT}(\boldsymbol{q})\right)^* a^\dagger_{\boldsymbol{q}L} a_{\boldsymbol{q}T} \Big],\end{aligned} \tag{3.2.21}$$

where the new coefficients were defined as

$$\nu_{LT}(\boldsymbol{q}) = \Gamma^1_{LT}(\boldsymbol{q})\, \delta_{T,\langle T\rangle_L} - \frac{1}{2} K \sin^2\vartheta_L \delta_{T,L}, \tag{3.2.22a}$$

$$\eta_{LT}(\boldsymbol{q}) = \Gamma^2_{LT}(\boldsymbol{q})\, \delta_{T,\langle T\rangle_L} + \delta_{T,L} \left(\sum_{\langle t\rangle_L} \zeta_{Lt} - \frac{1}{2} K \sin^2\vartheta_L \right). \tag{3.2.22b}$$

Moreover, the spin-wave Hamiltonian may be written on matrix form by $\boldsymbol{q} \to -\boldsymbol{q}$ in the first and third terms of eq. (3.2.21). Doing this gives

$$\mathcal{H}^{(2)}_{\mathrm{FM}} = \sum_{L,T,\boldsymbol{q}} \begin{pmatrix} a^{\dagger}_{\boldsymbol{q}L} & a_{-\boldsymbol{q}L} \end{pmatrix} \begin{pmatrix} \left(\eta_{LT}\left(\boldsymbol{q}\right)\right)^{*} & \left(\nu_{LT}\left(\boldsymbol{q}\right)\right)^{*} \\ \nu_{LT}\left(-\boldsymbol{q}\right) & \eta_{LT}\left(-\boldsymbol{q}\right) \end{pmatrix} \begin{pmatrix} a_{\boldsymbol{q}T} \\ a^{\dagger}_{-\boldsymbol{q}T} \end{pmatrix}. \tag{3.2.23}$$

We denote the vectors and matrix in this equation more compactly for any given $\boldsymbol{q}$ in the following

$$\mathcal{H}^{(2)}_{\mathrm{FM}}\left(\boldsymbol{q}\right) = \langle\alpha|\, \boldsymbol{\Lambda}_{\boldsymbol{q}}\, |\alpha\rangle\,, \tag{3.2.24}$$

in correspondence with eq. (2.4.2). Thus, $\boldsymbol{\Lambda}_{\boldsymbol{q}}$ is here the grand-dynamical matrix as introduced in section 2.4, defined as the block matrix in eq. (3.2.23) with elements $\boldsymbol{\eta}$, $\boldsymbol{\nu}$ and their conjugates. These elements were defined in eq. (3.2.22).

It remains to obtain the Bogoliubov transformation matrix that diagonalises the $\mathcal{H}^{(2)}_{\mathrm{FM}}$. Thus, this Hamiltonian is diagonalised in terms of new boson operators representing long-lived magnons. As in eq. (2.4.5), we write

$$\mathcal{H}^{(2)}_{\mathrm{FM}}\left(\boldsymbol{q}\right) = \langle\beta|\, \boldsymbol{\Omega}\, |\beta\rangle\,, \tag{3.2.25a}$$

$$|\beta\rangle = \boldsymbol{T}\, |\alpha\rangle\,, \tag{3.2.25b}$$

$$\boldsymbol{\Omega} = \boldsymbol{T}^{-\dagger} \boldsymbol{\Lambda} \boldsymbol{T}^{-1}, \tag{3.2.25c}$$

where $\boldsymbol{\Omega} = \frac{1}{2}\,\mathrm{diag}\left(\omega_{\boldsymbol{q},1}, \cdots, \omega_{\boldsymbol{q},2m}\right)$ contains the magnon dispersion relations for each band. We may insert for the elements of $|\beta\rangle$, as provided in eq. (2.4.7), to we write eq. (3.2.25a) in sum notation. Thus, we obtain

$$\mathcal{H}^{(2)}_{\mathrm{FM}} = \frac{1}{2} \sum_{\boldsymbol{q}} \sum_{L=1}^{m} \left[\omega_{\boldsymbol{q}L} b^{\dagger}_{\boldsymbol{q}L} b_{\boldsymbol{q}L} + \omega_{\boldsymbol{q},L+m} b_{-\boldsymbol{q}L} b^{\dagger}_{-\boldsymbol{q}L}\right], \tag{3.2.26}$$

for m number of sub-lattices of our SPFMI. This eq. (3.2.26) may be written more compactly. Apply bosonic commutation relations to eq. (3.2.26) to note that the band $\omega_{\boldsymbol{q},L+m} = \omega_{-\boldsymbol{q}L}$ is a positive magnon band $L+m$ equal to the negative magnon band L. Recall then that $\omega_{\boldsymbol{q}L} = \omega_{\boldsymbol{q},L+m}$ as concluded below eq. (2.4.6). We thereby conclude that the magnon dispersion relation displays inversion symmetry about the magnon momenta $\boldsymbol{q}$. Continue thus to rewrite the Hamiltonian in eq. (3.2.26) using this inversion symmetry and bosonic commutation relations. We obtain

$$\mathcal{H}^{(2)}_{\mathrm{FM}} = \sum_{\boldsymbol{q},L} \omega_{\boldsymbol{q}L} \left[b^{\dagger}_{\boldsymbol{q}L} b_{\boldsymbol{q}L} + \frac{1}{2}\right], \tag{3.2.27}$$

with $\omega_{\boldsymbol{q}L}$ the magnon dispersion. We understand that the second term in this Hamiltonian gives the ground state energy of magnons, while the first term gives the first order excitation energy.

3.3 Exchange interaction at the bilayer interface

We consider the magnon-mediated effective interactions between electrons to arise from one-to-one exchange interactions at the NM/SPFMI interface. Simplifications to this interaction model are introduced in section 5.3. In general, the exchange coupling strength $\bar{J}_i$ is site-dependent. We write this exchange interaction between spins $\boldsymbol{S}_i$ in the SPFMI and tightly bound electrons in the NM as the following

$$\mathcal{H}_{\text{e-m}} = -2\sum_i \bar{J}_i\Big(\langle c_i|\,\boldsymbol{\sigma}\,|c_i\rangle\Big)\cdot\boldsymbol{S}_i, \tag{3.3.1}$$

where the NM spin in eq. (2.3.7) was inserted for, resulting $c_{i\sigma}^{(\dagger)}$ the creation (annihilation) operator of a spin-σ electron. Moreover, the SPFMI spin operators must again be rotated to align with the local spin axes at each site. With this, the exchange Hamiltonian in eq. (3.3.1) at each sub-lattice L of the SPFMI may be expressed as

$$\mathcal{H}_{\text{e-m}}^{(L)} = -2\bar{J}_L\sum_{i\in L}\langle c_i|\,\boldsymbol{\sigma}\,|c_i\rangle\cdot\Big(\boldsymbol{U}\left(\vartheta_L,\psi_L\right)^T\widetilde{\boldsymbol{S}}_{iL}\Big), \tag{3.3.2}$$

where $\bar{J}_i \to \bar{J}_L$ as the magnon-electron interaction is solely determined by the orientation of the spins at each lattice site of the SPFMI. Note that this characterisation of sites and sub-lattices (i, L) is slightly different from (i', L) introduced in section 3.2: i now represents the lattice site indices which coincide with the sub-lattice L. This is important for the indexation of the NM spinors.

We seek to second quantise the interface interaction Hamiltonian. Thus, we expand the matrix and vector products of eq. (3.3.2) to have the electron operators explicit in our expression. Then we must apply the HP transformation to also have the boson operators explicit. This calculation is presented in appendix B.1, eventually giving

$$\begin{aligned}\mathcal{H}_{\text{e-m}}^{(L)} =& -\sqrt{2S}\bar{J}_L\cos\psi_L\sum_{i\in L,\sigma}\Big(a_{iL}\left(\cos\vartheta_L-\sigma\right)c_{i\sigma}^\dagger c_{i(-\sigma)}+\text{h.c}\Big)\\ &+\sqrt{2S}\bar{J}_L\sin\vartheta_L\sum_{i\in L,\sigma}\Big(\sigma a_{iL}c_{i\sigma}^\dagger c_{i\sigma}+\text{h.c}\Big)\\ &-2\bar{J}_L\sum_{i\in L,\sigma}\Big(S-a_{iL}^\dagger a_{iL}\Big)\Big[\sigma\cos\vartheta_L c_{i\sigma}^\dagger c_{i\sigma}+\sin\vartheta_L\cos\psi_L c_{i\sigma}^\dagger c_{i(-\sigma)}\Big],\end{aligned} \tag{3.3.3}$$

using the convention of σ as introduced in section 2.1. Furthermore, as we consider linear spin-wave theory, the second order terms in boson operators in eq. (3.3.3) are neglected.

We work towards analysing our system in the framework of the BCS theory. This is done in chapter 5. Preceedingly, we must Fourier transform the $\mathcal{H}_{\text{e-m}}^{(L)}$ to momentum space. From inspection of eq. (3.3.3), we may equivalently consider the transformation of the boson and fermion operators. These operators transform as

$$a_{iL} = \frac{1}{\sqrt{N_L}}\sum_{\boldsymbol{q}\in\text{mBZ}} a_{\boldsymbol{q}L}e^{-i\boldsymbol{q}\cdot\boldsymbol{r}_i}; \qquad c_{i\sigma} = \frac{1}{\sqrt{N}}\sum_{\boldsymbol{k}\in\text{mBZ}} c_{\boldsymbol{k}+\boldsymbol{Q}_\nu,\sigma}e^{-i(\boldsymbol{k}+\boldsymbol{Q}_\nu)\cdot\boldsymbol{r}_i}, \tag{3.3.4}$$

for which $\boldsymbol{k} \in \mathrm{mBZ}$, and $\{\boldsymbol{Q}_\nu\}$ is the set of magnon reciprocal lattice vectors. With this, Umklapp processes are explicitly included. Additionally, N is the number of lattice sites in our NM monolayer, while N_L is the number of sub-lattices in our SPFMI. Note therefore that $N_L = \frac{N}{m}$ for our system with m number of sub-lattices.

We may thus proceed to insert these Fourier transformed operators into the Hamiltonian in eq. (3.3.3) and simplify the expression. This calculation may be followed in appendix B.2. Following this calculation, we fint that the transformations in eq. (3.3.4) give rise to the following exchange Hamiltonian in momentum space

$$\begin{aligned}\mathcal{H}^{(L)}_{\text{e-m}} =& -\frac{\sqrt{2S}}{\sqrt{Nm}}\bar{J}_L \cos\psi_L \sum_{\boldsymbol{q},\boldsymbol{k},\nu,\sigma}\Big(e^{i\boldsymbol{Q}_\nu\cdot\boldsymbol{r}_L} a_{\boldsymbol{q}L}\left(\cos\vartheta_L - \sigma\right) c^\dagger_{\boldsymbol{k}+\boldsymbol{q}+\boldsymbol{Q}_\nu,\sigma} c_{\boldsymbol{k}(-\sigma)} + \text{h.c}\Big) \\ &+ \frac{\sqrt{2S}}{\sqrt{Nm}}\bar{J}_L \sin\vartheta_L \sum_{\boldsymbol{q},\boldsymbol{k},\nu,\sigma}\Big((\sigma e^{i\boldsymbol{Q}_\nu\cdot\boldsymbol{r}_L} a_{\boldsymbol{q}L} c^\dagger_{\boldsymbol{k}+\boldsymbol{q}+\boldsymbol{Q}_\nu,\sigma} c_{\boldsymbol{k}\sigma} + \text{h.c}\Big) \\ &- \frac{2S}{m}\bar{J}_L \sum_{\boldsymbol{k},\nu,\sigma} e^{i\boldsymbol{Q}_\nu\cdot\boldsymbol{r}_L}\Big(\sin\vartheta_L\cos\psi_L c^\dagger_{\boldsymbol{k}+\boldsymbol{Q}_\nu,\sigma} c_{\boldsymbol{k}(-\sigma)} + \sigma\cos\vartheta_L c^\dagger_{\boldsymbol{k}+\boldsymbol{Q}_\nu,\sigma} c_{\boldsymbol{k}\sigma}\Big).\end{aligned} \tag{3.3.5}$$

for $\boldsymbol{q} \in \mathrm{mBZ}$ and $\boldsymbol{k} \in \mathrm{eBZ}$. From inspection of this Hamiltonian, it is clear that the electron-magnon scattering processes may not only flip the electron spin, but also leave the electron spin unchanged. This spin-invariant scattering process is due to the breakdown of the magnon quantisation axis, as a consequence of the non-collinearity of the magnetic layer. For this reason, such a spin-invariant scattering process is not present in NM/SPFMI bilayer [47].

Note also that the last sum of eq. (3.3.5) is a free-electron contribution and may therefore influence the electron eigenstates of the NM. For this reason, this term should be excluded from $\mathcal{H}_{\text{e-m}}$ to instead be included in $\mathcal{H}_{\text{NM}}$. This is done in section 5.1.

With this, the interaction Hamiltonian for each sub-lattice L may be written

$$\mathcal{H}^{(L)}_{\text{e-m}} = \sum_{\boldsymbol{q}}^{\mathrm{mBZ}}\sum_{\boldsymbol{k}}^{\mathrm{eBZ}}\sum_{\nu,\sigma}\Big(g^1_{L\nu\sigma} a_{\boldsymbol{q}L} c^\dagger_{\boldsymbol{k}+\boldsymbol{q}+\boldsymbol{Q}_\nu,\sigma} c_{\boldsymbol{k}(-\sigma)} + g^2_{L\nu\sigma} a_{\boldsymbol{q}L} c^\dagger_{\boldsymbol{k}+\boldsymbol{q}+\boldsymbol{Q}_\nu,\sigma} c_{\boldsymbol{k}\sigma} + \text{h.c}\Big), \tag{3.3.6}$$

in which we defined

$$g^1_{L\nu\sigma} = -\frac{\sqrt{2S}}{\sqrt{Nm}}\bar{J}_L\cos\psi_L\left(\cos\vartheta_L - \sigma\right)e^{i\boldsymbol{Q}_\nu\cdot\boldsymbol{r}_L}, \tag{3.3.7a}$$

$$g^2_{L\nu\sigma} = \frac{\sqrt{2S}}{\sqrt{Nm}}\bar{J}_L\sigma\sin\vartheta_L e^{i\boldsymbol{Q}_\nu\cdot\boldsymbol{r}_L}, \tag{3.3.7b}$$

the electron-magnon coupling strengths for spin-flip and spin-invariant scattering processes, respectively.

We continue to diagonalise the exchange Hamiltonian in eq. (3.3.6) to study the model in terms of long-lived magnons. In the framework of the Bogoliubov transformation as presented in section 2.4, we transform the basis of eq. (3.3.6) into long-lived magnons using eq. (2.4.16). Note that only the boson operator $a_{\boldsymbol{q}L}$ is explicitly present in eq. (3.3.6). Thus, we may write

$$\mathcal{H}_{\text{e-m}} = \sum_{\boldsymbol{q}}^{\text{mBZ}} \sum_{\boldsymbol{k}}^{\text{eBZ}} \sum_{\nu,\sigma,\tilde{\sigma}} \sum_{L,\gamma=1}^{m} \left[g_{L\nu\sigma\tilde{\sigma}} \left(u_{\boldsymbol{q}L\gamma} b_{\boldsymbol{q}\gamma} + v_{\boldsymbol{q}L\gamma} b^{\dagger}_{-\boldsymbol{q}\gamma} \right) c^{\dagger}_{\boldsymbol{k}+\boldsymbol{q}+\boldsymbol{Q}_{\nu},\sigma} c_{\boldsymbol{k}\tilde{\sigma}} + \text{h.c} \right], \quad (3.3.8)$$

where the new coefficient is defined in the following

$$g_{L\nu\sigma\tilde{\sigma}} = g^{1}_{L\nu\sigma}\delta_{\tilde{\sigma},-\sigma} + g^{2}_{L\nu\sigma}\delta_{\tilde{\sigma},\sigma}, \quad (3.3.9)$$

for $g^{1}_{L\nu\sigma}$ and $g^{2}_{L\nu\sigma}$ defined in eq. (3.3.7). We study this Hamiltonian to understand that the interface interactions present in our system include two types of scattering between electrons and magnons, represented by the two operator product terms. This is concluded as the hermitian conjugate term embeds operator products that may be written on the form of those explicit in eq. (3.3.8) by appropriately rescaling dummy indices by ± 1. Regarding the two types of scattering processes, both involve the annihilation of an electron to create a new electron. Additionally for each process, one type also involves the annihilation of a magnon, whereas the other type results in the creation of a magnon. Note thus that by writing out the hermitian conjugate term and collecting operator products in eq. (3.3.8), the coefficients of each scattering term will represent the coupling strength of interaction.

4 Effective electron-electron interaction

With the theory of our bilayer model at hand, we may proceed to study the effective electron-electron interactions within our system. We use the system Hamiltonian under the Schrieffer-Wolff transformation presented in section 2.5 to obtain a formulation purely in terms of electrons. Thus, the effective interaction potential is obtained.

We begin with collecting the models in chapter 3 to state the total system Hamiltonian; $\mathcal{H} = \mathcal{H}_{\text{NM}} + \mathcal{H}_{\text{FM}} + \mathcal{H}_{\text{e-m}}$, giving

$$\begin{aligned}\mathcal{H} =& \sum_{\boldsymbol{k},\sigma} \epsilon_{\boldsymbol{k}} c^\dagger_{\boldsymbol{k}\sigma} c_{\boldsymbol{k}\sigma} + \sum_{\boldsymbol{q},\gamma} \omega_{\boldsymbol{q}\gamma} b^\dagger_{\boldsymbol{q}\gamma} b_{\boldsymbol{q}\gamma} \\ &+ \sum_{\boldsymbol{q}}^{\text{mBZ}} \sum_{\boldsymbol{k}}^{\text{eBZ}} \sum_{\nu,\sigma,\tilde{\sigma}} \sum_{L,\gamma=1}^{m} \left[g_{L\nu\sigma\tilde{\sigma}} \left(u_{\boldsymbol{q}L\gamma} b_{\boldsymbol{q}\gamma} + v_{\boldsymbol{q}L\gamma} b^\dagger_{-\boldsymbol{q}\gamma} \right) c^\dagger_{\boldsymbol{k}+\boldsymbol{q}+\boldsymbol{Q}_\nu,\sigma} c_{\boldsymbol{k}\tilde{\sigma}} + \text{h.c} \right].\end{aligned} \tag{4.0.1}$$

with each term derived in sections 3.1 to 3.3, respectively. The pair interaction (last term) describes interactions between electrons and magnons, represented by the field operators $c_{\boldsymbol{k}}$ and $b_{\boldsymbol{q}}$, respectively. As previously noted in section 3.3, these interactions may result both spin-conserving and -flipped scattering of electrons. Moreover, these interactions may include Umklapp scattering, explicitly denoted by the boson reciprocal lattice vector $\boldsymbol{Q}_\nu$, reaching all magnon Brillouin zones (mBZs) filling the first electron Brillouin zone (eBZ1). If Umklapp scattering is not necessitated, one may simply set $\boldsymbol{Q}_\nu = 0$ and disregard any indices ν, both primed and unprimed.

The tedious Schrieffer-Wolff transformation of this system Hamiltonian is presented in appendix B.3 for completeness. This calculation results the pair interaction Hamiltonian eq. (B.3.21), restated here for completeness

$$\mathcal{H}_{\text{pair}} = \sum_{\boldsymbol{q},\boldsymbol{k},\nu} \sum_{\boldsymbol{k}',\nu'} \sum_{\{\sigma_i\}} V^{\sigma_1\sigma_2\sigma_3\sigma_4}_{\boldsymbol{k}\boldsymbol{q}\nu\nu'} c^\dagger_{\boldsymbol{k}+\boldsymbol{q}+\boldsymbol{Q}_\nu,\sigma_1} c_{\boldsymbol{k}\sigma_2} c^\dagger_{\boldsymbol{k}'-\boldsymbol{q}+\boldsymbol{Q}_{\nu'},\sigma_3} c_{\boldsymbol{k}'\sigma_4}, \tag{4.0.2}$$

with $\boldsymbol{q} \in$ mBZ and $\boldsymbol{k}, \boldsymbol{k}' \in$ eBZ as previously. The effective interaction potential from eq. (B.3.22) is

$$V^{\sigma_1\sigma_2\sigma_3\sigma_4}_{\boldsymbol{k}\boldsymbol{q}\nu\nu'} = -\frac{1}{2} \sum_\gamma \left[\frac{A^{\sigma_1\sigma_2\sigma_3\sigma_4}_{\boldsymbol{q}\gamma\nu\nu'}}{\epsilon_{\boldsymbol{k}} - \epsilon_{\boldsymbol{k}+\boldsymbol{q}+\boldsymbol{Q}_\nu} + \omega_{\boldsymbol{q}\gamma}} - \frac{A^{\sigma_3\sigma_4\sigma_1\sigma_2}_{-\boldsymbol{q}\gamma\nu'\nu}}{\epsilon_{\boldsymbol{k}} - \epsilon_{\boldsymbol{k}+\boldsymbol{q}+\boldsymbol{Q}_\nu} - \omega_{\boldsymbol{q}\gamma}} \right]. \tag{4.0.3}$$

with the coefficients $A^{\sigma_1\sigma_2\sigma_3\sigma_4}_{\boldsymbol{q}\gamma\nu\nu'}$ from eq. (B.3.23), given by

$$A^{\sigma_1\sigma_2\sigma_3\sigma_4}_{\boldsymbol{q}\gamma\nu\nu'} = \sum_{L,L'} \Big(g_{L\nu\sigma_1\sigma_2} g_{L'\nu'\sigma_3\sigma_4} u_{\boldsymbol{q}L\gamma} v_{-\boldsymbol{q}L'\gamma} + g_{L\nu\sigma_1\sigma_2} g^*_{L'\bar{\nu}'\sigma_4\sigma_3} u_{\boldsymbol{q}L\gamma} u^*_{\boldsymbol{q}L'\gamma} + g^*_{L\bar{\nu}\sigma_2\sigma_1} g_{L'\nu'\sigma_3\sigma_4} v^*_{-\boldsymbol{q}L\gamma} v_{-\boldsymbol{q}L'\gamma} + g^*_{L\bar{\nu}\sigma_2\sigma_1} g^*_{L'\bar{\nu}'\sigma_4\sigma_3} v^*_{-\boldsymbol{q}L\gamma} u^*_{\boldsymbol{q}L'\gamma} \Big), \tag{4.0.4}$$

as a function of $g_{L\nu\sigma_1\sigma_2}$, given by eq. (3.3.9).

It remains to verify that the effective electron-electron potential is independent of any arbitrary phase factor originating from the inverse Bogoliubov transformation, as discussed previously when presenting eq. (2.4.15). Note that each term of eq. (4.0.4) is accompanied by the product of some element of the γ^{th} column of the inverse Bogoliubov transformation matrix and the complex conjugate of some other element of the same eigenvector $|\tau_\gamma\rangle$. Thus, any arbitrary phase factor of $|\tau_\gamma\rangle$ indeed cancels out in the effective electron-electron interaction potential.

Continue to express the electron operator products of eq. (4.0.2) in terms of Cooper pairs. In doing so, utilise fermion commutation relations and disregard second-order operator terms. The latter is valid as these operators do not contribute to the effective pair interaction. This procedure leads the following

$$c^\dagger_{\boldsymbol{k}+\boldsymbol{q}+\boldsymbol{Q}_\nu,\sigma_1} c_{\boldsymbol{k}\sigma_2} c^\dagger_{\boldsymbol{k}'-\boldsymbol{q}+\boldsymbol{Q}_{\nu'},\sigma_3} c_{\boldsymbol{k}'\sigma_4} \quad \Rightarrow \quad c^\dagger_{\boldsymbol{k}+\boldsymbol{q}+\boldsymbol{Q}_\nu,\sigma_1} c^\dagger_{\boldsymbol{k}'-\boldsymbol{q}+\boldsymbol{Q}_{\nu'},\sigma_3} c_{\boldsymbol{k}'\sigma_4} c_{\boldsymbol{k}\sigma_2}. \tag{4.0.5}$$

Inserting the Cooper pair formulation into the pair interaction Hamiltonian, we may write

$$\mathcal{H}_{\text{pair}} \equiv \sum_{\boldsymbol{q},\boldsymbol{k},\nu} \sum_{\boldsymbol{k}',\nu'} \sum_{\{\sigma_i\}} V^{\sigma_1\sigma_2\sigma_3\sigma_4}_{\boldsymbol{k}\boldsymbol{q}\nu\nu'} c^\dagger_{\boldsymbol{k}+\boldsymbol{q}+\boldsymbol{Q}_\nu,\sigma_1} c^\dagger_{\boldsymbol{k}'-\boldsymbol{q}+\boldsymbol{Q}_{\nu'},\sigma_2} c_{\boldsymbol{k}'\sigma_3} c_{\boldsymbol{k}\sigma_4}, \tag{4.0.6}$$

where the effective pair interaction potential was redefined to $V^{\sigma_1\sigma_2\sigma_3\sigma_4}_{\boldsymbol{k}\boldsymbol{q}\nu\nu'} \equiv V^{\sigma_1\sigma_4\sigma_2\sigma_3}_{\boldsymbol{k}\boldsymbol{q}\nu\nu'}$ to match the order of spin-indices appearing in the operator product.

At last, simplifying the redefined potential from eq. (4.0.3), we get

$$V^{\sigma_1\sigma_2\sigma_3\sigma_4}_{\boldsymbol{k}\boldsymbol{q}\nu\nu'} = -\frac{1}{2} \sum_\gamma \frac{1}{\left(\epsilon_{\boldsymbol{k}} - \epsilon_{\boldsymbol{k}+\boldsymbol{q}+\boldsymbol{Q}_\nu}\right) - \omega^2_{\boldsymbol{q}\gamma}} \left[\omega_{\boldsymbol{q}\gamma} \mathcal{A}^{\sigma_1\sigma_2\sigma_3\sigma_4}_{\boldsymbol{q}\gamma\nu\nu'} + \left(\epsilon_{\boldsymbol{k}} - \epsilon_{\boldsymbol{k}+\boldsymbol{q}+\boldsymbol{Q}_\nu}\right) \mathcal{B}^{\sigma_1\sigma_2\sigma_3\sigma_4}_{\boldsymbol{q}\gamma\nu\nu'} \right], \tag{4.0.7}$$

with the enhancement factors defined as

$$\mathcal{A}^{\sigma_1\sigma_2\sigma_3\sigma_4}_{\boldsymbol{q}\gamma\nu\nu'} = -A^{\sigma_1\sigma_4\sigma_2\sigma_3}_{\boldsymbol{q}\gamma\nu\nu'} - A^{\sigma_2\sigma_3\sigma_1\sigma_4}_{-\boldsymbol{q}\gamma\nu'\nu}, \tag{4.0.8a}$$

$$\mathcal{B}^{\sigma_1\sigma_2\sigma_3\sigma_4}_{\boldsymbol{q}\gamma\nu\nu'} = A^{\sigma_1\sigma_4\sigma_2\sigma_3}_{\boldsymbol{q}\gamma\nu\nu'} - A^{\sigma_2\sigma_3\sigma_1\sigma_4}_{-\boldsymbol{q}\gamma\nu'\nu}, \tag{4.0.8b}$$

and $A^{\sigma_1\sigma_4\sigma_2\sigma_3}_{\boldsymbol{q}\gamma\nu\nu'}$ as provided in eq. (4.0.4). This concludes the general derivation of the pair interaction Hamiltonian for our relevance.

5 Implementing the model simplifications

The model Hamiltonian presented in the previous sections may be studied in more detail by implementing simplifications. For this purpose, let all interaction strengths be uniform, such that the hopping amplitude in the NM $t_{ij} = t$ for j nearest neighbour of i; the DMI vector components of the SPFMI $\left|D_{ij}^{\alpha}\right| = D$; the exchange coupling strength of the SPFMI $J_{ij}^{\alpha\beta} = J$; and the interface exchange coupling $\bar{J}_i = \bar{J}$. With the latter simplification, we have fully compensated coupling. This is a widely used and accepted simplification among the literature. Moreover, we introduce some simplifications for the SPFMI only. First, the off-diagonal symmetric exchange coupling is assumed negligible compared to the diagonal when considering impact on the spin structure. Second, let the spin structure be coplanar, meaning the spins $\boldsymbol{S}_i$ only span a plane. We let this be the global xz-plane, such that the polar rotation angle $\vartheta_i \in [0, \pi]$ while the azimuthal rotation angle $\psi_i \in \{0, \pi\}$, or equivalently, $\vartheta_i \in [0, 2\pi]$ and $\psi_i = 0$. Consequently, the DMI-vector is only finite along the global $\hat{y}$-axis, and only present between nearest neighbours along the global $\hat{x}$-axis. For this reason, we may write $\boldsymbol{D}_{ij} = D \cos\varphi_{ij}\hat{y}$ for φ_{ij} the angle that a line through the sites i and j makes to the line $\parallel \hat{x}$ through site i. Effectively, we are then dealing with one-dimensional spin-rotating chains connected by the exchange coupling. These interactions are indicated in fig. 3.2. Third, consider the case of no easy axis anisotropy, i.e., let $K = 0$. This simplifies the system greatly as the spins may then evolve with a constant angle along the chains. At last, we study the effective electron-electron interaction Hamiltonian in the framework of the BCS theory.

The plots and other results in this chapter and the following are obtained from a Python code written as a part of this thesis. This code is available online at github.com/saratomris/master-thesis to cover any curiosity.

5.1 Simplifying the normal metal Hamiltonian

The normal metal (NM) model Hamiltonian as presented in eq. (3.1.3) is unaffected by the aforementioned simplifications. However, the additional term from eq. (3.3.5) needs closer inspection. For completeness and enhanced readability, we restate this term here

$$-\frac{2S}{m}\bar{J}_L \sum_{\boldsymbol{k}}^{\text{eBZ}} \sum_{\nu,\sigma} e^{i\boldsymbol{Q}_\nu \cdot \boldsymbol{r}_L} \left(\sin\vartheta_L \cos\psi_L c^\dagger_{\boldsymbol{k}+\boldsymbol{Q}_\nu,\sigma} c_{\boldsymbol{k}(-\sigma)} + \sigma \cos\vartheta_L c^\dagger_{\boldsymbol{k}+\boldsymbol{Q}_\nu,\sigma} c_{\boldsymbol{k}\sigma} \right). \tag{5.1.1}$$

Generally, the operator products here describe scattering of electrons within the first electron Brillouin zone (eBZ1). In the $K = 0$ approximation, the spiral spin-phase of the magnetic layer leads no net magnetization (of the SPFMI). Consequently, the sinusoidal dependence on the global spin-angle of each site gives null when summing over all sub-lattices L. Note however that the exponential prefactor of this term is sub-lattice dependent, so this reasoning is only valid for $\boldsymbol{Q}_\nu = 0$, i.e., for electron momenta within the first magnon Brillouin zone (mBZ1). Therefore, the terms in eq. (5.1.1) become significant for scattering at any Fermi surface extending beyond the mBZ1. However, the inclusion of these terms requires a new diagonalisation of the NM Hamiltonian, leading new terms in the electron dispersion up to order $\bar{J}$. This would lead higher order perturbative terms in the effective potential, and are therefore discarded. For this reason, we limit any Fermi surface of interest to stay within mBZ1 when concentric, so that the term in eq. (5.1.1) may safely be disregarded up to second order in $\bar{J}$.

Resultingly, we may continue to simplify the NM system presented in section 3.1. The electron dispersion relation in $\mathcal{H}_{\text{NM}}$ is affected by the simplification to uniform interaction strengths: letting all $t_{ij} = t$ in eq. (3.1.7), gives the following electron dispersion

$$\tilde{\epsilon}_{\boldsymbol{k}} = -2t \left[\cos(k_x a) + 2\cos\left(\frac{1}{2}k_x a\right) \cos\left(\frac{\sqrt{3}}{2}k_y a\right) \right] - \mu. \tag{5.1.2}$$

The smallest possible relative chemical potential is at the Fermi surface $\tilde{\epsilon}_{\boldsymbol{k}} = 0$, giving $\mu/t = -6$. We investigate the system for $\mu/t \in \{-5.9,\ -5.43\}$, chosen to compare a Fermi surface within the mBZ1 with good margin, and a Fermi surface near the mBZ1 edges. The shifted dispersion relation in eq. (5.1.2) is shown in fig. 5.1 as a gradient colour plot of k_x and k_y for these chosen values of μ/t. The corresponding colour bar maps these colours to the relative energy dispersion for each μ/t. This plot also shows the eBZ (black) and mBZ (red) concentric with the two Fermi surfaces for $\mu/t \in \{-5.9,\ -5.43\}$ in solid and dashed white, respectively. Moreover, note the periodicity of $\tilde{\epsilon}_{\boldsymbol{k}}$ with the eBZ, arising from the periodicity of the Brillouin zone itself.

Moreover, the simplified electron dispersion in eq. (5.1.2) may be used to calculate the density of states (DoS) using eq. (3.1.13). Our function $f(k) = \epsilon - \epsilon_{k,\theta}$ thus becomes

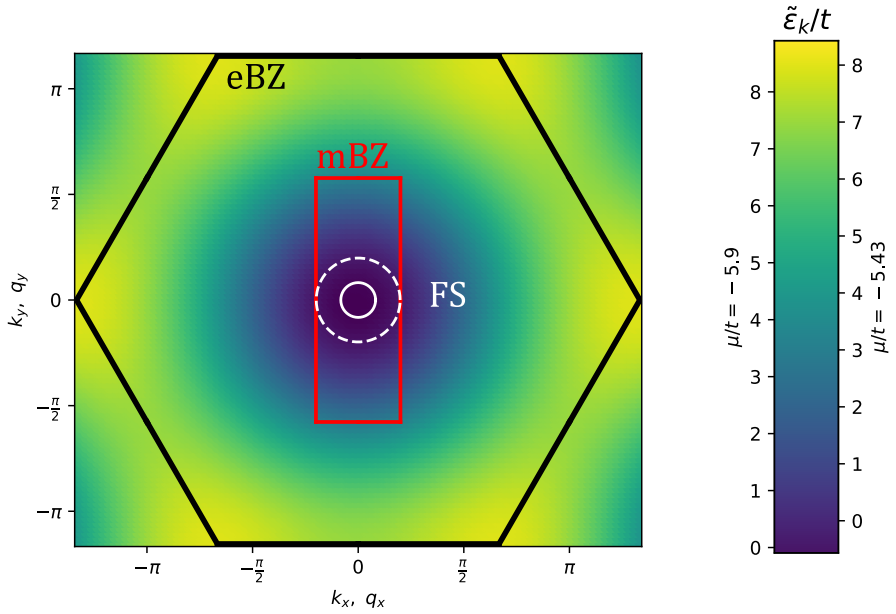

Figure 5.1: Primary plot (leftmost) and corresponding colour bar (rightmost). Illustrates a gradient colour plot representing the shifted electron dispersion $\tilde{\epsilon}_{\boldsymbol{k}}$. The eBZ1 and mBZ1 are drawn in black and red, respectively, along with the representation of two Fermi surfaces in white. The dashed Fermi surface corresponds to that for $\mu/t = -5.43$, while that in solid corresponds to $\mu/t = -5.9$. The colour bar indicates values of the electron energies for each case, relative the hopping amplitude. Plotted for lattice parameter $a = 1$.

$$f(k) = \epsilon + 2t\Big[\cos(k_x a) + 2\cos\left(\frac{1}{2}k_x a\right)\cos\left(\frac{\sqrt{3}}{2}k_y a\right)\Big]. \tag{5.1.3}$$

We may thereby numerically solve the DoS by inserting this function into eq. (3.1.13). The result is plotted in fig. 5.2. Note that the DoS diverges at $\epsilon_{\boldsymbol{k}} = 2t$. This is due to the van Hove instability [48, 49] at the high-symmetry $\boldsymbol{M}$-point, indicated by the dashed line. Moreover, we may compare the dispersion relation in the rightmost fig. 5.2 with the colour plot in fig. 5.1 to note the correspondences in maxima and minima.

5.2 Simplifying the spiral-phase ferromagnetic insulator Hamiltonian

Under the simplifications mentioned introductory to this chapter, the SPFMI Hamiltonian will transform such that various quantites may be studied in more detail. Here, we continue the study from section 3.2 to investigate the simplified zeroth, first, and second order Hamiltonians.

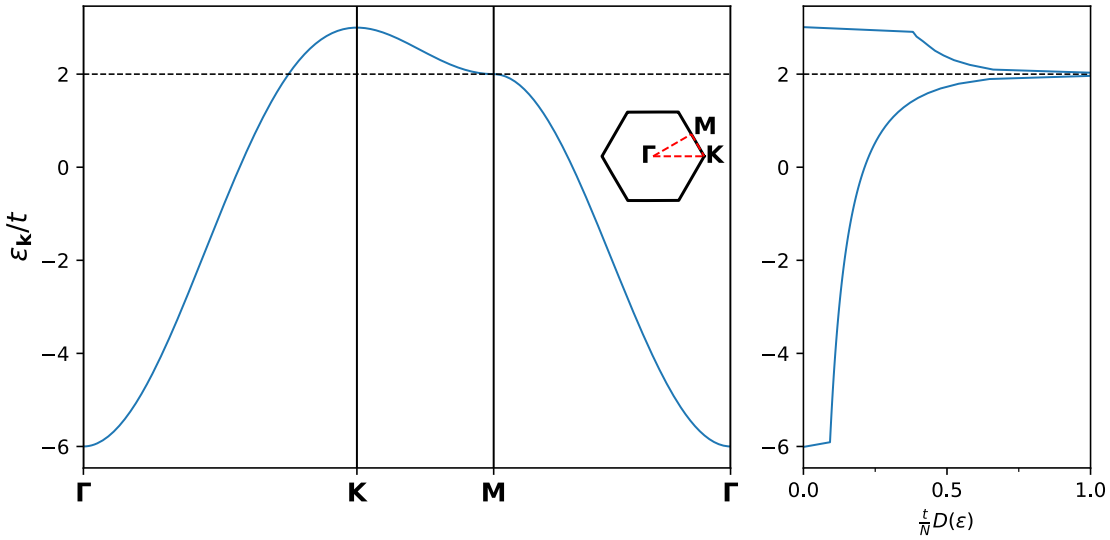

Figure 5.2: Two subplots. The leftmost graphs the electron dispersion on the eBZ surface. Embedded within this plot is also the eBZ indicating the high-symmetry points. The rightmost shows the electron dispersion as a function of DoS; or rather, the DoS on the horisontal axis as a function of the electron dispersion on the vertical axis. This choice is made to obtain correspondence between the vertical axes.

Constant term SPFMI Hamiltonian

Implementing the aforementioned simplifications in $\mathcal{H}^{(0)}_{\text{FM}}$ lets us derive the ground state energy analytically. The constant term Hamiltonian may thus written as

$$\mathcal{H}^{(0)}_{\text{FM}} = -S^2 \sum_{\langle i,j \rangle} W^{zz}_{ij}. \tag{5.2.1}$$

In this case, a uniform change in spin angle by $\Delta\vartheta$ along a given chain is reliably assumed. The corresponding energy of site i thus becomes

$$\begin{aligned} E_i = &-2S^2 J \left[2\cos\Delta\vartheta + \cos\phi_{ij} + \cos\phi'_{ij} + \cos\left(\phi_{ij} - \Delta\vartheta\right) + \cos\left(\phi'_{ij} - \Delta\vartheta\right)\right] \\ &- 4S^2 D \sin\Delta\vartheta \end{aligned} \tag{5.2.2}$$

in which we have defined the angles $\phi^{(\prime)}_{ij} = \vartheta_i - \vartheta_{j^{(\prime)}}$ for j, j' on different neighbouring chains. The three angles present in the single-site energy in eq. (5.2.2) are determined by the ground state of this energy, as obtained by minimising this equation with respect to each angle. Minimising with respect to ϕ_{ij} and ϕ'_{ij} are easily solved, giving $\phi_{ij} = \phi'_{ij} = \frac{\Delta\vartheta}{2}$. A direct consequence is thus that our system has $m = 2n$ sub-lattices for a spiral-periodicity of n. Inserting for $\phi^{(\prime)}_{ij}$ into eq. (5.2.2) before minimising the energy with respect to $\Delta\vartheta$ gives

$$\frac{D}{J} = \frac{\sin\Delta\vartheta + \sin\frac{\Delta\vartheta}{2}}{\cos\Delta\vartheta}. \tag{5.2.3}$$

Solving this equation for finite coupling strengths gives the smallest spiral periodicity of 5 atoms.

First order SPFMI Hamiltonian

Recall that the first order Hamiltonian in section 3.2 simply gave requirements for the angles ψ_i and ϑ_i which were to be satisfied by the ground state of the system. This can now be confirmed. Implementing the four simplifications to $\mathcal{H}_{\text{FM}}^{(1)}$, gives

$$\begin{aligned}\mathcal{H}_{\text{FM}}^{(1)} = -S\sqrt{\frac{S}{2}}\sum_{\langle i,j\rangle}\Big[&W_{ij}^{xz}\left(a_i^\dagger + a_i\right) + W_{ij}^{zx}\left(a_j^\dagger + a_j\right) \\ &+ iW_{ij}^{yz}\left(a_i^\dagger - a_i\right) + iW_{ij}^{zy}\left(a_j^\dagger - a_j\right)\Big],\end{aligned} \tag{5.2.4}$$

with the requirements

$$\underline{\mathfrak{Im}(\cdot):} \quad \sum_{\langle j\rangle}\left(W_{ij}^{yz} + W_{ji}^{zy}\right) = 0, \tag{5.2.5a}$$

$$\underline{\mathfrak{Re}(\cdot):} \quad \sum_{\langle j\rangle}\left(W_{ij}^{xz} + W_{ji}^{zx}\right) = 0. \tag{5.2.5b}$$

Inserting for the coefficients $W_{ij}^{\alpha\beta}$ as provided in appendix A.1, we may see that the requirements eq. (5.2.5) correspond to those of the ground state .

Second order SPFMI Hamiltonian

The four simplifications will not impact the derived expression for $\mathcal{H}_{\text{FM}}^{(2)}$ as presented in eq. (3.2.27). However, implementing these simplifications will let us calculate the magnon spectrum of our SPFMI. This was done numerically in Python. For a periodicity of $n = 5$, giving $m = 10$ magnon modes, the plot is shown in fig. 5.3 Note that all bands cross or overlap some other band at least once. This is clear for instance between the $\boldsymbol{X}$ and $\boldsymbol{S}$-points, where the 10 bands appear as 5 distinct bands. Note also that the lowest energy at the $\boldsymbol{\Gamma}$-point is finite, compared to the null minimum $\boldsymbol{\Gamma}$-point energy of an ordered FMI. This is due to the DMI creating the spiral-phase spin structure of higher energy state than an ordered FMI.
The main challenge encountered in plotting the magnon spectrum shown in fig. 5.3 involved band sorting, which can be regarded as an assignment problem.

Several importable Python packages provide various functions to handle assignment problems; for instance, the `linear_sum_assignment()` function in the `scipy.optimize` package [50, 51]. However, the sorting algorithm occasionally failed to accurately sort the bands, leading unphysical peaks in energy for random momenta, or path-dependent values. The latter was apparent as some bands would have different energies at the same high-symmetry point, depending on the path taken. This sorting issue likely arose from the overlapping of bands in specific momentum regions, although the choice of momentum range and sampling points

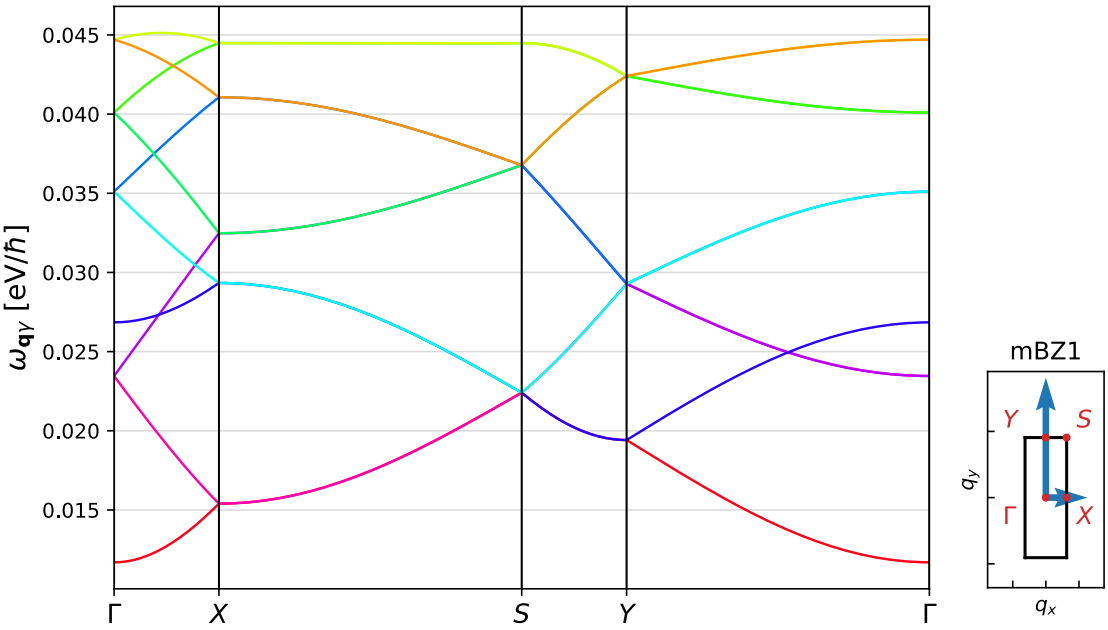

Figure 5.3: Two plots: the main plot (leftmost) is the magnon spectrum plotted for $\boldsymbol{q}$-values through high-symmetry points of mBZ1; while the right plot indicates these high-symmetry points of the mBZ1, along with the blue arrows illustrating the reciprocal lattice vectors. The magnon spectrum is plotted for $n = 5$, leading $m = 10$ magnon modes. Each colour represents a different band. In some regions of momenta, the distinction of bands are limited by their overlap. Plotted for parameter $J = 50$meV.

presumably also contributed to this problem. It was also observed that the initial ordering of magnon modes affected the unphysicality of the plot.

The sorting of bands was verified by plotting two points of the same high-symmetry point in the same plot, and requiring continuity across this point. This is done with the **Γ**-point in fig. 5.3.

Initially, only the path-dependency of magnon modes was present. Then, the array of magnon momenta `q_array` spanned the path through high-symmetry points as indicated in the plot: from the **Γ**-point, through $\boldsymbol{X}$, $\boldsymbol{S}$, and $\boldsymbol{Y}$, and back to the **Γ**-point. For this `q_array`, the sorting of bands was highly dependent on the momentum sampling points. This dependency was clear by the path-dependent values of the modes changing path as the sampling points was varied. The solution to this issue involved extending the data of `q_array` to span the entire mBZ1.

By extending the array of magnon momenta `q_array` to span the entire mBZ1, the unphysical peaks in magnon modes appeared. The cause of unphysical peaks in magnon modes was initially nontrivial to determine. Eventually, experimenting with the plot revealed that manipulating the array of magnon momenta (`q_array`) could eliminate the undesired peaks. The first manipulation of `q_array` was to exclude the bottom and leftmost edges of the mBZ1. This change is intuitive in that these edges correspond to the top and rightmost edges by symmetry of the Brillouin zone. However, understanding why including these edges would lead several

peaks in the magnon modes is vague. It was concluded that numerical limitations might have caused the issue. Nevertheless, only a few unphysical peaks remained after implementing this change in the range of `q_array`. Thus, the second and last manipulation included the momentum sampling points: too few points might potentially have lead numerical issues related to the sorting. The sorting was complete after increasing this number of sampling points. This was confirmed by implementing a hovering ability, allowing to check whether each band γ indeed approach the same $\omega_{\boldsymbol{q}}$-value at both $\boldsymbol{\Gamma}$-points.

5.3 Simplifying the effective electron-electron interaction potential

First, we investigate the importance of Umklapp scattering to determine whether this must be included in our calculations. We must therefore conclude whether the Fermi surfaces extend beyond the mBZ1 centered around some $\boldsymbol{k}$-point of interest on the said Fermi surface. Figure 5.4 illustrates this at the two Fermi surfaces with $\mu/t \in \{-5.9,\ -5.43\}$. It is clear that Umklapp processes are needed to reach the entire $\mu/t = -5.43$ Fermi surface for $\boldsymbol{q} \in$ mBZ, while regular processes are sufficient at the $\mu/t = -5.9$ Fermi surface. Indeed, numerical calculations indicate that values $\mu/t \gtrsim -5.853$ require Umklapp processes to stay within the mBZ1.

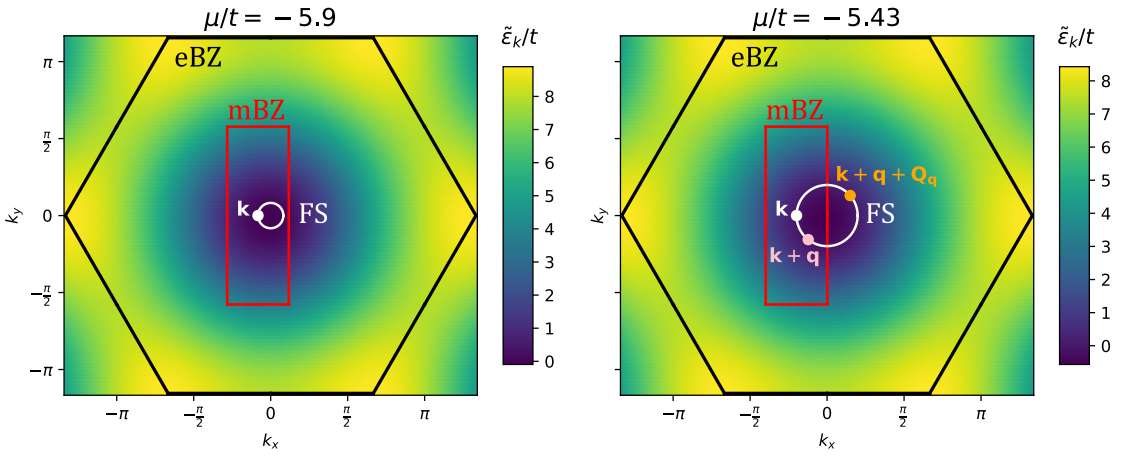

Figure 5.4: Two subplots with energy dispersion for Fermi surface $\mu/t = -5.9$ (leftmost) and Fermi surface $\mu/t = -5.43$ (rightmost). In each plot, the mBZ (red) is now centred at a chosen $\boldsymbol{k}$-value at the Fermi surface. Scattering processes are only drawn for the $\mu/t = -5.43$ Fermi surface, where the requirement for scattering is extended to $\boldsymbol{k}+\boldsymbol{q}+\boldsymbol{Q}_\nu \in$ FS. It is clear that regular processes are sufficient for the $\mu/t = -5.9$ Fermi surface.

Consequently, the effective electron-electron interactions must account for Umklapp processes for a sufficiently large Fermi surface. The reciprocal lattice vectors $\boldsymbol{Q}_\nu$ are obtained in the following: fill the eBZ1 with mBZs, and define $\{\boldsymbol{Q}_\nu\}$ as the set of vectors from point $\boldsymbol{k} = 0$ to the centre of each mBZ. Figure 5.5 is an

illustration of this situation, such that $\{\boldsymbol{Q}_\nu\}$ is the set of vectors from the centre of the eBZ to the centre of each mBZ marked with a green point.

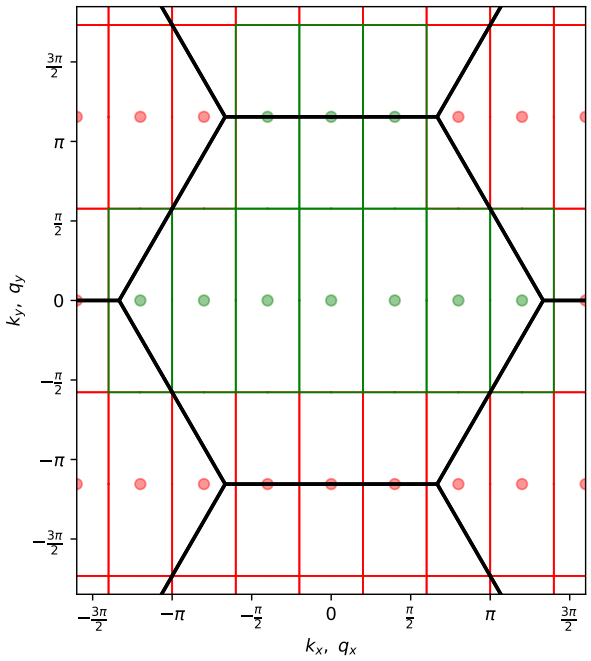

Figure 5.5: Several mBZs for spin-spiral periodicity $n = 5$ filling the eBZ1. The eBZ is illustrated in solid black line, while the mBZs are either red or green. Due to periodicity of the BZ, the green mBZs fill the eBZ1 entirely. The green and red points indicate the centre of each mBZ.

As seen in fig. 5.5, $\{\boldsymbol{Q}_\nu\}$ is of order 10. This is confirmed by the ratio of areas $A_{\text{eBZ}}/A_{\text{mBZ}} = 10$. Altogether, we get the following set of reciprocal lattice vectors

$$\{\boldsymbol{Q}_\nu\} = 2\pi \left\{ (0,0)\,, \left(\pm\frac{1}{5}, 0\right), \left(\pm\frac{2}{5}, 0\right), \left(\pm\frac{3}{5}, 0\right), \left(0, \frac{1}{\sqrt{3}}\right), \left(\pm\frac{1}{5}, \frac{1}{\sqrt{3}}\right) \right\}. \quad (5.3.1)$$

Furthermore, we simplify the pair interaction Hamiltonian $\mathcal{H}_{\text{pair}}$ from eq. (4.0.6) in the BCS formalism. First, require opposite momenta of the Cooper pairs. Thus, let $\boldsymbol{k}' = -\boldsymbol{k}$ to satisfy this requirement for the annihilated Cooper pair. For the remaining Cooper pair, let $\nu' \to \bar{\nu}$: $\boldsymbol{Q}_{\nu'} \to \boldsymbol{Q}_{\bar{\nu}} = -\boldsymbol{Q}_\nu$, and define the new variable $\boldsymbol{k}' \equiv \boldsymbol{k} + \boldsymbol{q} + \boldsymbol{Q}_\nu$. The electron operator product of $\mathcal{H}_{\text{pair}}$ becomes

$$\Rightarrow c^\dagger_{\boldsymbol{k}'\sigma_1} c^\dagger_{-\boldsymbol{k}'\sigma_3} c_{-\boldsymbol{k}\sigma_4} c_{\boldsymbol{k}\sigma_2}, \quad (5.3.2)$$

while the effective interaction potential in eq. (4.0.7) transforms as

$$\begin{aligned} V^{\sigma_1\sigma_2\sigma_3\sigma_4}_{\boldsymbol{k}\boldsymbol{q}\nu\nu'} \Rightarrow & -\frac{1}{2}\sum_\gamma \frac{1}{(\epsilon_{\boldsymbol{k}} - \epsilon_{\boldsymbol{k}'}) - \omega^2_{\boldsymbol{q}\gamma}} \left[\omega_{\boldsymbol{q}\gamma} \mathcal{A}^{\sigma_1\sigma_2\sigma_3\sigma_4}_{\boldsymbol{q}\gamma\nu} + (\epsilon_{\boldsymbol{k}} - \epsilon_{\boldsymbol{k}'})\, \mathcal{B}^{\sigma_1\sigma_2\sigma_3\sigma_4}_{\boldsymbol{q}\gamma\nu} \right] \\ & \equiv V^{\sigma_1\sigma_2\sigma_3\sigma_4}_{\boldsymbol{k}\boldsymbol{k}'}, \end{aligned} \quad (5.3.3)$$

where ν is determined from which $\boldsymbol{Q}_\nu$ is closest to $\boldsymbol{k}' - \boldsymbol{k}$ to ensure $\boldsymbol{q} \in \mathrm{mBZ}$; and $\boldsymbol{q}$ is determined from the presented definition of $\boldsymbol{k}'$. The enhancement factors are given by eq. (4.0.8) for ν' as defined above. At the Fermi surface, the effective potential in eq. (5.3.3) reduces to eq. (5.3.4) by $\epsilon_{\boldsymbol{k}} = \epsilon_{\boldsymbol{k}'}$. For completeness, this expression is written in terms of the enhancement factors; the coefficients $A^{\sigma_1\sigma_2\sigma_3\sigma_4}_{\boldsymbol{q}\gamma\nu}$ of the enhancement factors given by eq. (4.0.8); and the functions $g_{L\nu\sigma_1\sigma_2}$ of the coefficients $A^{\sigma_1\sigma_2\sigma_3\sigma_4}_{\boldsymbol{q}\gamma\nu}$. We write

$$V^{\sigma_1\sigma_2\sigma_3\sigma_4}_{\boldsymbol{k}\boldsymbol{k}'}\Big|_{\mathrm{FS}} = -\sum_\gamma \frac{1}{2\omega_{\boldsymbol{q}\gamma}} \mathcal{A}^{\sigma_1\sigma_2\sigma_3\sigma_4}_{\boldsymbol{q}\gamma\nu} \tag{5.3.4a}$$

$$= \sum_\gamma \frac{1}{2\omega_{\boldsymbol{q}\gamma}} \left(A^{\sigma_1\sigma_4\sigma_2\sigma_3}_{\boldsymbol{q}\gamma\nu} + A^{\sigma_2\sigma_3\sigma_1\sigma_4}_{-\boldsymbol{q}\gamma\bar{\nu}} \right) \tag{5.3.4b}$$

$$\begin{aligned} = \sum_{\gamma,L,L'} \frac{1}{2\omega_{\boldsymbol{q}\gamma}} \Big(& g_{L\nu\sigma_1\sigma_4} g_{L'\bar{\nu}\sigma_2\sigma_3} u_{\boldsymbol{q}L\gamma} v_{-\boldsymbol{q}L'\gamma} + g_{L\nu\sigma_1\sigma_4} g^*_{L'\nu\sigma_3\sigma_2} u_{\boldsymbol{q}L\gamma} u^*_{\boldsymbol{q}L'\gamma} \\ & + g^*_{L\bar{\nu}\sigma_4\sigma_1} g_{L'\bar{\nu}\sigma_2\sigma_3} v^*_{-\boldsymbol{q}L\gamma} v_{-\boldsymbol{q}L'\gamma} + g^*_{L\bar{\nu}\sigma_4\sigma_1} g^*_{L'\nu\sigma_3\sigma_2} v^*_{-\boldsymbol{q}L\gamma} u^*_{\boldsymbol{q}L'\gamma} \\ & + g_{L\bar{\nu}\sigma_2\sigma_3} g_{L'\nu\sigma_1\sigma_4} u_{-\boldsymbol{q}L\gamma} v_{\boldsymbol{q}L'\gamma} + g_{L\bar{\nu}\sigma_2\sigma_3} g^*_{L'\bar{\nu}\sigma_4\sigma_1} u_{-\boldsymbol{q}L\gamma} u^*_{-\boldsymbol{q}L'\gamma} \\ & + g^*_{L\nu\sigma_3\sigma_2} g_{L'\nu\sigma_1\sigma_4} v^*_{\boldsymbol{q}L\gamma} v_{\boldsymbol{q}L'\gamma} + g^*_{L\nu\sigma_3\sigma_2} g^*_{L'\bar{\nu}\sigma_4\sigma_1} v^*_{\boldsymbol{q}L\gamma} u^*_{-\boldsymbol{q}L'\gamma} \Big) \end{aligned} \tag{5.3.4c}$$

This effective interaction potential is plotted at the Fermi surfaces for $\mu/t \in \{-5.9, -5.43\}$ in figs. 5.6 and 5.7, respectively. In these figures, overlapping lines are not distinguished. This choice aims to enhance figure clarity by reducing visual clutter. For completeness, the plots in which all lines are distinguished may be seen in appendix C.1.

Note that in general, the potentials with null real part have finite imaginary parts and vice versa: the effective potentials are not complex.

Moreover, by comparison of the two plots for Fermi surfaces $\mu/t = -5.9$ and $\mu/t = -5.43$, we note that the maximum or minimum of amplitudes are increased.

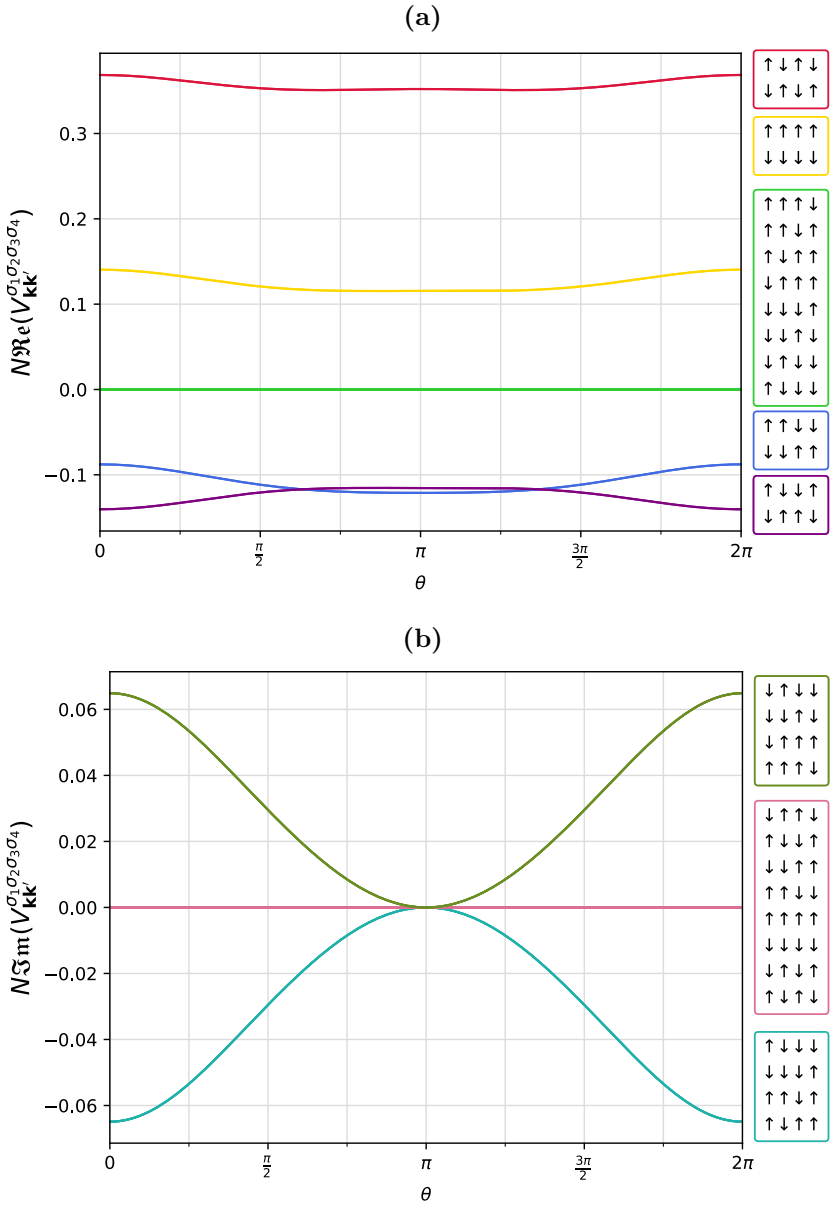

Figure 5.6: Two subplots: real (a) and imaginary (b) part of the effective interaction potential at the $\mu/t = -5.9$ Fermi surface, plotted as a function of the angle θ spanning the Fermi surface. The $\boldsymbol{k}'$ point is chosen for angle $\theta' = \pi$, and $\boldsymbol{k}$ is located at the various θs. The plot in (a) shows five distinct lines; from largest to smallest values at $\theta = 0$, these are red, yellow, green, blue, and purple. The red line represents spin-conserving scattering of spin-unpolarised electrons giving $\sigma_1\sigma_2\sigma_3\sigma_4 = \uparrow\downarrow\uparrow\downarrow$ and opposite. This scattering potential is largest, followed by the yellow line representing spin-invariant scattering between spin-polarised electron pairs. The green line represents scattering between spin-unpolarised Cooper pairs and spin-polarised Cooper pairs. The blue line represents spin-flip scattering of spin-polarised electrons, i.e., with spin-combination $\uparrow\uparrow\downarrow\downarrow$ and opposite. At last, the purple line represents the remaining spin-conserving scattering of spin-unpolarised electrons ($\uparrow\downarrow\downarrow\uparrow$ and opposite). The plot in (b) show three distinct lines: the dark green, faded pink, and teal. The dark green and teal lines represent scattering between spin-unpolarised Cooper pairs and spin-polarised Cooper pairs, while the pink line represents the remaining.

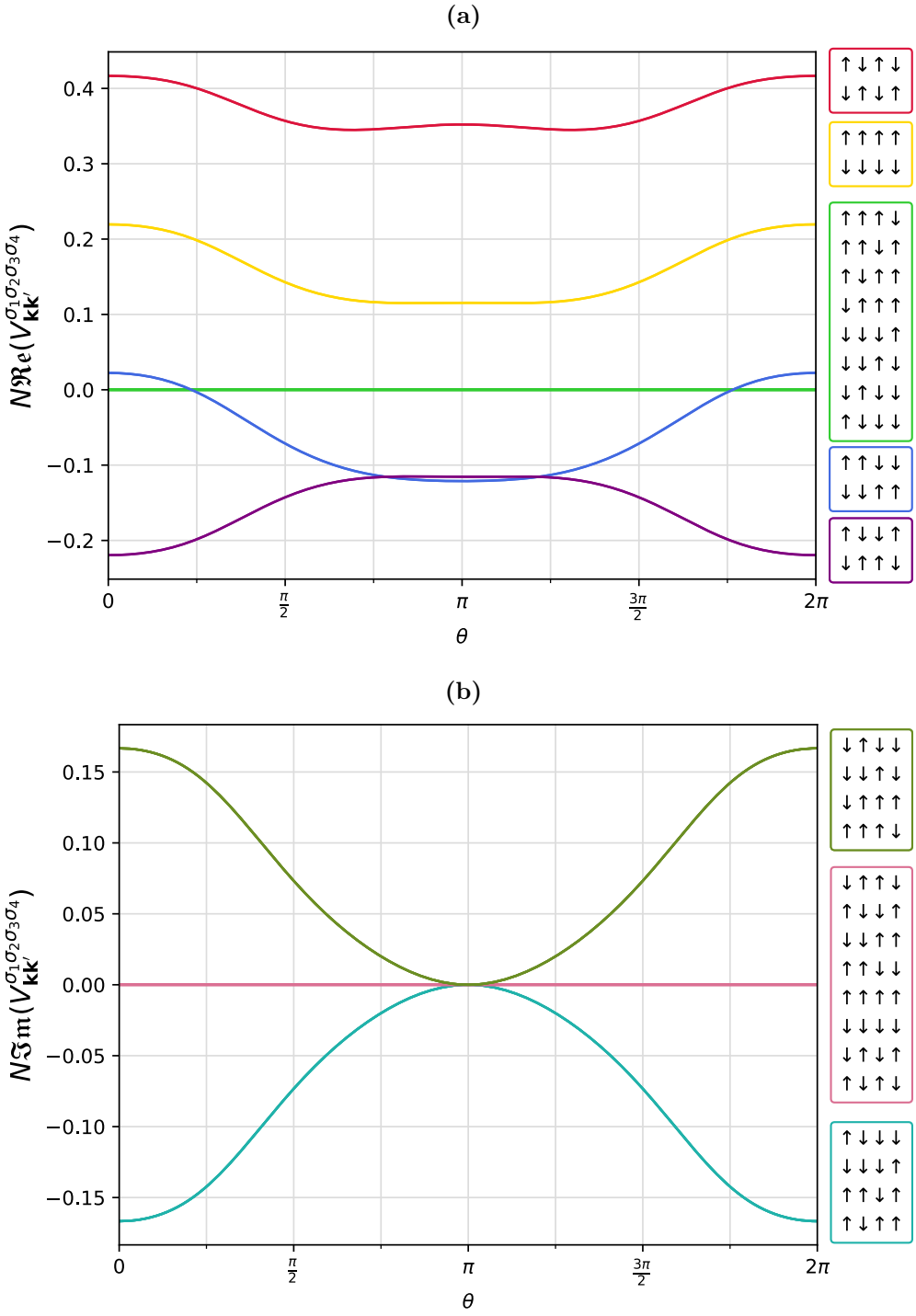

Figure 5.7: Corresponds to the plot in fig. 5.6 for a larger Fermi surface: two subplots for the real (a) and imaginary (b) parts of the effective interaction potential at the $\mu/t = -5.43$ Fermi surface including Umklapp scattering, plotted as a function of the angle θ spanning the Fermi surface. The $\boldsymbol{k}'$ point is chosen for angle $\theta' = \pi$, and $\boldsymbol{k}$ is located at the various θs. The potentials at this Fermi surface are similar to those on the $\mu/t = -5.9$ Fermi surface shown in fig. 5.6, only with an increased amplitude.

Note that for both Fermi surfaces, the real part of the scattering potential for the $\uparrow\downarrow\uparrow\downarrow$ spin-combination (and opposite) are largest. This magnitude dominates all potentials, both real and imaginary values. On the other hand, the imaginary value of these potentials is null. Altogether, this suggests that these spin-conserving scattering between spin-unpolarised Cooper pairs are the largest contributor to the scattering in our system. Despite this observation, it is too soon to conclude whether the system is a conventional s-wave superconductor. The remaining spin-conserving scattering between spin-unpolarised Cooper pairs are shown in purple in figs. 5.6a and 5.7a. The reason for the two different magnitudes of the spin-conserving scattering of spin-unpolarised Cooper pairs lies in the definitions of the coefficients $g^{(n)}_{L\nu\sigma_1\sigma_2}$ as defined in eq. (3.3.7). Moreover, we may compare the real and imaginary parts to note that the scattering from spin-unpolarised to spin-polarised Cooper pairs and vice versa is finite for $\boldsymbol{k}' \neq \boldsymbol{k}$. We interpret that this scattering necessitates a change in momentum of the involved Cooper pairs. Note also the symmetry of each pair potential across $\theta = \pi$. This is interpreted to originate from the momentum inversion symmetry of the magnon dispersion.

Moreover, we observe that several lines may cross for various angles. Such a crossing is not unlikely to occur due to the many terms constructing the effective potential, and no specific physical interpretation is associated with this behaviour.

We proceed to rewrite the pair interaction Hamiltonian in eq. (4.0.6). With the electron operator product in eq. (5.3.2) and reduced effective interaction potential as defined in eq. (5.3.3), the $\mathcal{H}_{\text{pair}}$ may be written as follows

$$\mathcal{H}_{\text{pair}} = \sum_{\boldsymbol{k},\boldsymbol{k}'} \sum_{\{\sigma_i\}} V^{\sigma_1\sigma_2\sigma_3\sigma_4}_{\boldsymbol{k}\boldsymbol{k}'} c^\dagger_{\boldsymbol{k}'\sigma_1} c^\dagger_{-\boldsymbol{k}'\sigma_2} c_{-\boldsymbol{k}\sigma_3} c_{\boldsymbol{k}\sigma_4}. \tag{5.3.5}$$

We continue to rewrite the effective interaction potential such that the pair interaction Hamiltonian may instead be written

$$\mathcal{H}_{\text{pair}} = \frac{1}{2} \sum_{\boldsymbol{k},\boldsymbol{k}'} \sum_{\{\sigma_i\}} \bar{V}^{\sigma_1\sigma_2\sigma_3\sigma_4}_{\boldsymbol{k}\boldsymbol{k}'} c^\dagger_{\boldsymbol{k}'\sigma_1} c^\dagger_{-\boldsymbol{k}'\sigma_2} c_{-\boldsymbol{k}\sigma_3} c_{\boldsymbol{k}\sigma_4}, \tag{5.3.6}$$

with the new effective interaction potential obeying the following symmetries

$$\bar{V}^{\sigma_1\sigma_2\sigma_3\sigma_4}_{\boldsymbol{k}\boldsymbol{k}'} = \bar{V}^{\sigma_2\sigma_1\sigma_4\sigma_3}_{(-\boldsymbol{k})(-\boldsymbol{k}')} = -\bar{V}^{\sigma_1\sigma_2\sigma_4\sigma_3}_{(-\boldsymbol{k})\boldsymbol{k}'} = -\bar{V}^{\sigma_2\sigma_1\sigma_3\sigma_4}_{\boldsymbol{k}(-\boldsymbol{k}')}, \tag{5.3.7}$$

in addition to $\bar{V}^{\sigma_1\sigma_2\sigma_3\sigma_4}_{\boldsymbol{k}\boldsymbol{k}'} = \left(\bar{V}^{\sigma_4\sigma_3\sigma_2\sigma_1}_{\boldsymbol{k}'\boldsymbol{k}}\right)^*$ as a result of Hermicity of the Hamiltonian. In accordance, we conclude that $(\bar{V}^{\sigma_1\sigma_2\sigma_3\sigma_4}_{\boldsymbol{k}\boldsymbol{k}'})^T = \bar{V}^{\sigma_4\sigma_3\sigma_2\sigma_1}_{\boldsymbol{k}'\boldsymbol{k}}$. To obtain an expression for $\bar{V}^{\sigma_1\sigma_2\sigma_3\sigma_4}_{\boldsymbol{k}\boldsymbol{k}'}$, consider the sum in eq. (5.3.6). Collect then the coefficients of the operator structure as present in eq. (5.3.2), up to some commutation. Rewriting these operator products to be on the stated form, gives the following expression for the new reduced effective interaction potential

$$\bar{V}^{\sigma_1\sigma_2\sigma_3\sigma_4}_{\boldsymbol{k}\boldsymbol{k}'} = \frac{1}{2}\left(V^{\sigma_1\sigma_2\sigma_3\sigma_4}_{\boldsymbol{k}\boldsymbol{k}'} + V^{\sigma_2\sigma_1\sigma_4\sigma_3}_{(-\boldsymbol{k})(-\boldsymbol{k}')} - V^{\sigma_1\sigma_2\sigma_4\sigma_3}_{(-\boldsymbol{k})\boldsymbol{k}'} - V^{\sigma_2\sigma_1\sigma_3\sigma_4}_{\boldsymbol{k}(-\boldsymbol{k}')}\right), \tag{5.3.8}$$

and it is clear that $\bar{V}^{\sigma_1\sigma_2\sigma_3\sigma_4}_{\boldsymbol{k}\boldsymbol{k}'}$ satisfies the symmetries in eq. (5.3.7). The motivation for the effective potential to possess this symmetry, is embedded in a requirement

of consistency [52]: the interaction potential for a given operator structure should remain when commuting and changing indices such that the operator structure remains.

Altogether, the effective Hamiltonian becomes

$$\mathcal{H}_{\text{eff}} = \sum_{\boldsymbol{k},\sigma} \epsilon_{\boldsymbol{k}} c^\dagger_{\boldsymbol{k}\sigma} c_{\boldsymbol{k}\sigma} + \frac{1}{2} \sum_{\boldsymbol{k},\boldsymbol{k}'}^{\text{eBZ}} \sum_{\{\sigma_i\}} \bar{V}^{\sigma_1\sigma_2\sigma_3\sigma_4}_{\boldsymbol{k}\boldsymbol{k}'} c^\dagger_{\boldsymbol{k}'\sigma_1} c^\dagger_{-\boldsymbol{k}'\sigma_2} c_{-\boldsymbol{k}\sigma_3} c_{\boldsymbol{k}\sigma_4}, \tag{5.3.9}$$

a many-body problem in the BCS formalism, purely described in terms of electron operators. Moreover, the barred effective potential as defined in eq. (5.3.8) is plotted in figs. 5.8 and 5.9 for $\mu \in \{-5.9, -5.43\}$, respectively. In similar with the plot for the unbarred effective potentials, these plots do not display overlapping lines either. Instead, the plots in which all lines are distinguished may be found in appendix C.1. Note that comparing the plots for the two different Fermi surfaces, we observe that the larger Fermi surface with $\mu/t = -5.43$ plotted in fig. 5.9 resembles that for $\mu/t = -5.9$ plotted in fig. 5.8 though with larger amplitudes. Furthermore, note again that the potentials are not complex: those with null real part have finite imaginary parts and vice versa.

Nonetheless, it remains to formulate the many-body problem in eq. (5.3.9) as a self-consistent one-particle problem.

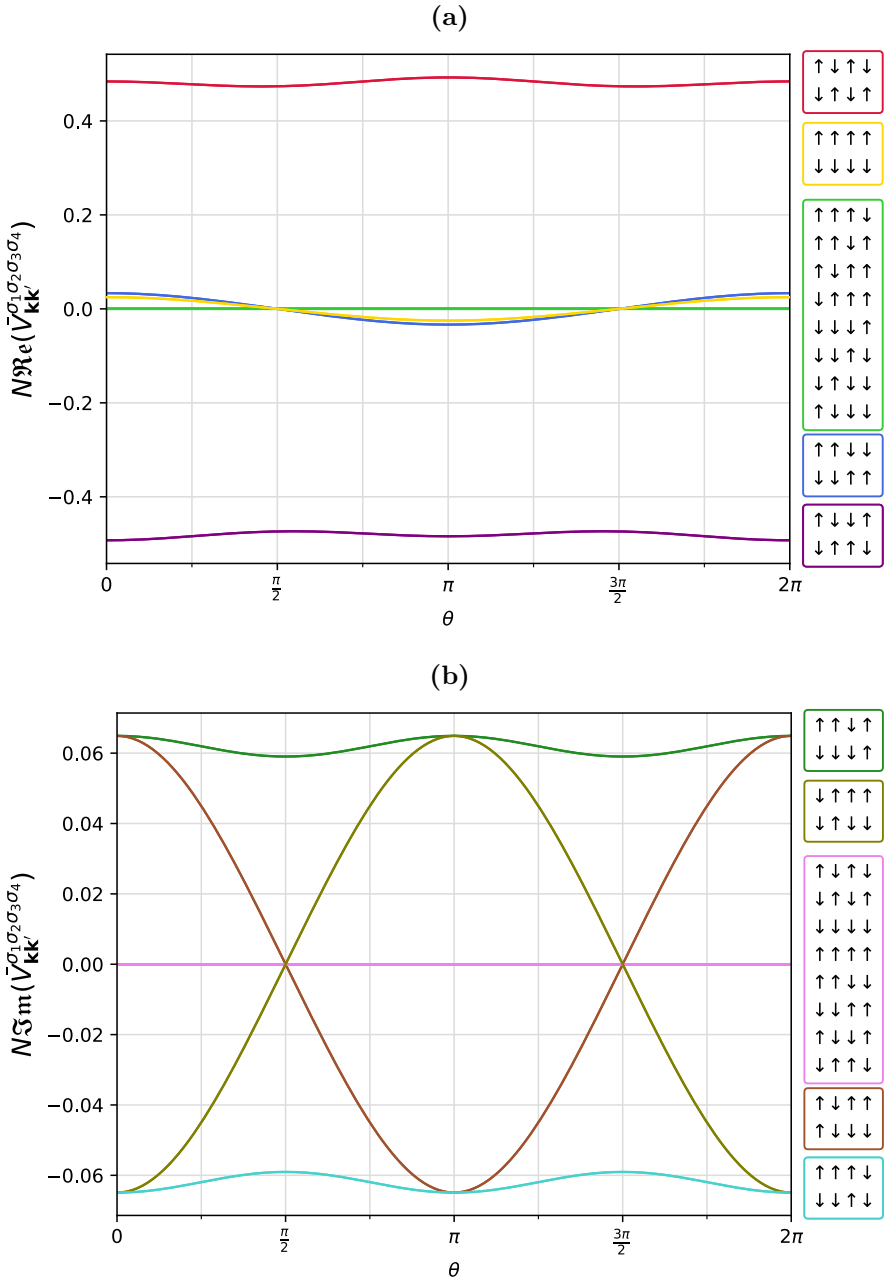

Figure 5.8: Two subplots of the barred effective interaction potential at the $\mu/t = -5.9$ Fermi surface, plotted as a function of the angle θ spanning the Fermi surface. The $\boldsymbol{k}'$ point is chosen for angle $\theta' = \pi$, and $\boldsymbol{k}$ is located at the various θs. In (a) the real part of the barred potential is shown, while the imaginary part is shown in (b). The plot in (a) shows five distinct lines; from largest to smallest values at $\theta = 0$, these are red, blue, yellow, green, and purple. The colours here represent the same scattering processes as in fig. 5.6a. However, the shape of the potentials differ. The plot in (b) also shows five distinct lines; from largest to smallest values at $\theta = 0$, these are light blue, olive green, brown, light green, and gold. The blue, gold, and both green lines represent scattering between spin-unpolarised Cooper pairs and spin-polarised Cooper pairs, corresponding to the green null-line in a. The brown null-line represents the remaining scatterings, which should be noted, have finite real parts.

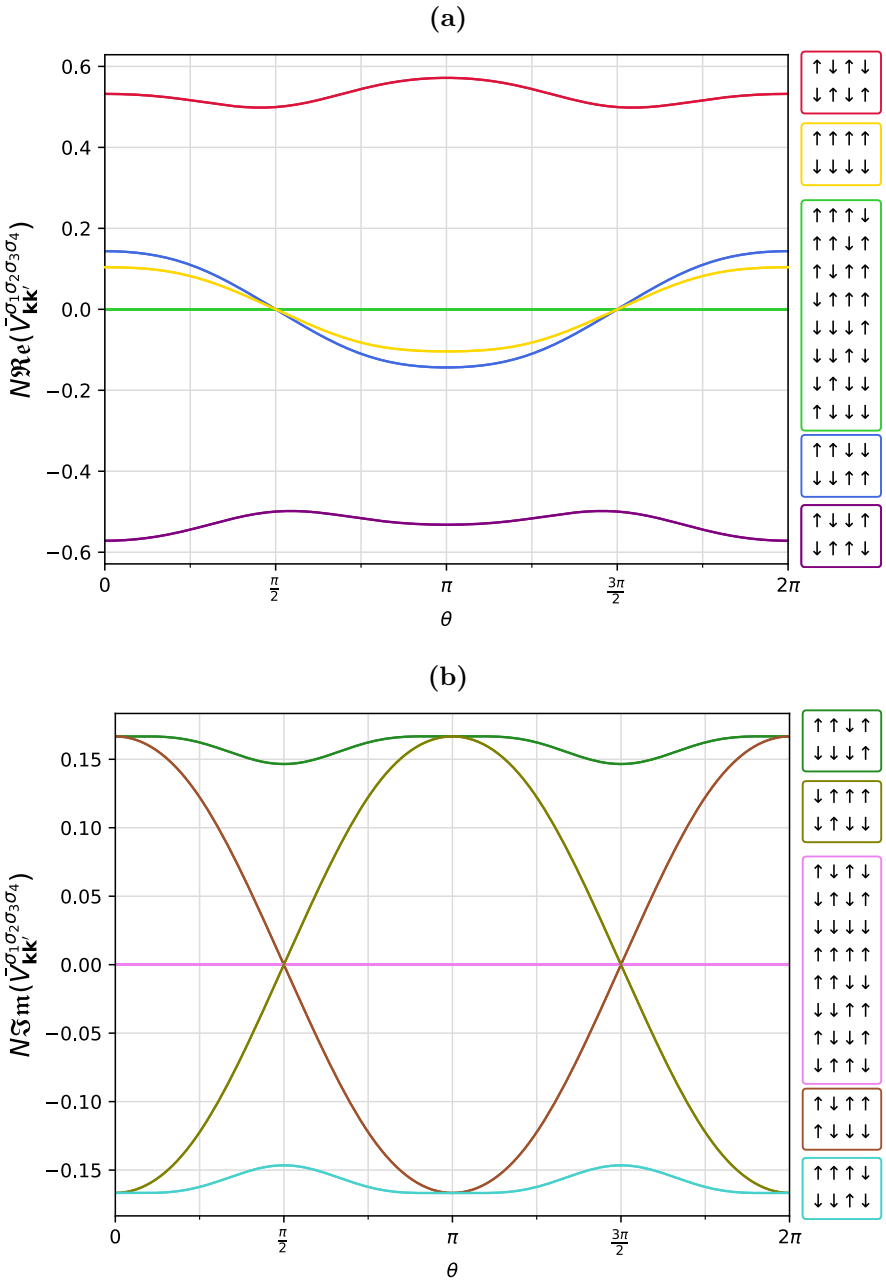

Figure 5.9: Corresponds to the plot in fig. 5.8 for a larger Fermi surface: two subplots for the real (a) and imaginary (b) parts of the barred effective interaction potential at the $\mu/t = -5.43$ Fermi surface including Umklapp scattering, plotted as a function of the angle θ spanning this Fermi surface. The $\boldsymbol{k}'$ point is chosen for angle $\theta' = \pi$, and $\boldsymbol{k}$ is located at the various θs. The potentials at this Fermi surface are similar to those on the $\mu/t = -5.9$ Fermi surface shown in fig. 5.8, only with an increased amplitude.

6 Superconductivity

In this chapter, we investigate the simplified model to further reduce the many-body problem described in eq. (5.3.9) into a self-consistent one-particle problem for detailed system analysis. This simplification is obtained using the mean-field approximation, incorporating statistical averages of the Cooper-pair operators. From this, we obtain the superconducting gap equation, which is proceedingly solved in the linearised limit.

6.1 Mean-field approximation

The effective Hamiltonian in eq. (5.3.9) is reduced into a one-particle problem by first introducing ensemble averages for the Cooper pair mean field. Define thus

$$b_{\boldsymbol{k}\sigma_1\sigma_2} = \langle c_{-\boldsymbol{k}\sigma_1} c_{\boldsymbol{k}\sigma_2} \rangle; \qquad b^\dagger_{\boldsymbol{k}\sigma_2\sigma_1} = \langle c^\dagger_{\boldsymbol{k}\sigma_1} c^\dagger_{-\boldsymbol{k}\sigma_2} \rangle, \tag{6.1.1}$$

such that $(b_{\boldsymbol{k}\sigma_1\sigma_2})^\dagger = b^\dagger_{\boldsymbol{k}\sigma_1\sigma_2}$. The mean-field elements must not be confused with the elements of the basis that diagonalised $\mathcal{H}^{(2)}_{\mathrm{FM}}$ in section 3.2. Moreover, the Fourier transform of this statistical average gives the wave function of Cooper-pairs [26, p. 162]. Note then that finite $b_{\boldsymbol{k}\sigma_1\sigma_2}$ indicates a fluctuating number of Cooper pairs in our condensate, i.e., the particle number is no longer a conserved quantity, and our system is grand canonical. From Noether's theorem, it follows that some symmetry must then be broken: a finite value of the ensemble average results a spontaneous $U(1) \to Z_2$ symmetry breaking [53, p. 284]. We say that the ensemble averages $b_{\boldsymbol{k}\sigma_1\sigma_2}$ are the order parameters of the superconducting state [54].

Nonetheless, write the electron operator products in eq. (5.3.9) in terms of these ensemble averages such that

$$c_{-\boldsymbol{k}\sigma_1} c_{\boldsymbol{k}\sigma_2} = b_{\boldsymbol{k}\sigma_1\sigma_2} + \delta b_{\boldsymbol{k}\sigma_1\sigma_2}, \tag{6.1.2a}$$

$$c^\dagger_{\boldsymbol{k}\sigma_1} c^\dagger_{-\boldsymbol{k}\sigma_2} = b^\dagger_{\boldsymbol{k}\sigma_2\sigma_1} + \delta b^\dagger_{\boldsymbol{k}\sigma_2\sigma_1}. \tag{6.1.2b}$$

Assume small fluctuations around the mean-field, such that $\mathcal{O}(\delta b^2)$ are negligible. Insert the mean-field operators into the operator product in eq. (5.3.9) to obtain

$$c^\dagger_{\boldsymbol{k}'\sigma_1} c^\dagger_{-\boldsymbol{k}'\sigma_2} c_{-\boldsymbol{k}\sigma_3} c_{\boldsymbol{k}\sigma_4} = -b_{\boldsymbol{k}\sigma_3\sigma_4} b^\dagger_{\boldsymbol{k}'\sigma_2\sigma_1} + b_{\boldsymbol{k}\sigma_3\sigma_4} c^\dagger_{\boldsymbol{k}'\sigma_1} c^\dagger_{-\boldsymbol{k}'\sigma_2} + b^\dagger_{\boldsymbol{k}'\sigma_2\sigma_1} c_{-\boldsymbol{k}\sigma_3} c_{\boldsymbol{k}\sigma_4}. \tag{6.1.3}$$

We use this mean field formulation to write the pair interaction Hamiltonian as follows

$$\mathcal{H}_{\text{pair}} = \frac{1}{2}\sum_{\boldsymbol{k},\sigma_1,\sigma_2} \Delta_{\boldsymbol{k}\sigma_1\sigma_2} b^\dagger_{\boldsymbol{k}\sigma_2\sigma_1} - \frac{1}{2}\sum_{\boldsymbol{k},\sigma_1,\sigma_2} \left(\Delta_{\boldsymbol{k}\sigma_1\sigma_2} c^\dagger_{\boldsymbol{k}\sigma_1} c^\dagger_{-\boldsymbol{k}\sigma_2} + \Delta^\dagger_{\boldsymbol{k}\sigma_2\sigma_1} c_{-\boldsymbol{k}\sigma_1} c_{\boldsymbol{k}\sigma_2}\right), \tag{6.1.4}$$

in which we defined the gap parameters

$$\Delta_{\boldsymbol{k}\sigma_1\sigma_2} \equiv -\sum_{\boldsymbol{k}',\sigma_3,\sigma_4} \bar{V}^{\sigma_1\sigma_2\sigma_3\sigma_4}_{\boldsymbol{k}'\boldsymbol{k}} b_{\boldsymbol{k}'\sigma_3\sigma_4}, \tag{6.1.5a}$$

$$\Delta^\dagger_{\boldsymbol{k}\sigma_2\sigma_1} \equiv -\sum_{\boldsymbol{k}',\sigma_3,\sigma_4} \bar{V}^{\sigma_3\sigma_4\sigma_1\sigma_2}_{\boldsymbol{k}\boldsymbol{k}'} b_{\boldsymbol{k}'\sigma_4\sigma_3}. \tag{6.1.5b}$$

Note then that

$$\Delta_{-\boldsymbol{k}\sigma_1\sigma_2} = -\Delta_{\boldsymbol{k}\sigma_2\sigma_1} \tag{6.1.6}$$

from the symmetries of the potential, given in eq. (5.3.7).

Continue to insert eq. (6.1.5) into the effective Hamiltonian in eq. (5.3.9) to obtain

$$\mathcal{H}_{\text{MF}} = \sum_{\boldsymbol{k},\sigma} \epsilon_{\boldsymbol{k}} c^\dagger_{\boldsymbol{k}\sigma} c_{\boldsymbol{k}\sigma} + \frac{1}{2}\sum_{\boldsymbol{k},\sigma_1,\sigma_2} \Delta_{\boldsymbol{k}\sigma_1\sigma_2} b^\dagger_{\boldsymbol{k}\sigma_2\sigma_1} - \frac{1}{2}\sum_{\boldsymbol{k},\sigma_1,\sigma_2} \left(\Delta_{\boldsymbol{k}\sigma_1\sigma_2} c^\dagger_{\boldsymbol{k}\sigma_1} c^\dagger_{-\boldsymbol{k}\sigma_2} + \Delta^\dagger_{\boldsymbol{k}\sigma_2\sigma_1} c_{-\boldsymbol{k}\sigma_1} c_{\boldsymbol{k}\sigma_2}\right), \tag{6.1.7}$$

the mean-field Hamiltonian.

It remains to write this Hamiltonian more compactly in terms of new quasi-particles and their energies: we must diagonalise the system. Therefore, continue to write $\mathcal{H}_{\text{MF}}$ in matrix form to obtain

$$\mathcal{H}_{\text{MF}} = \mathcal{H}_0 + \frac{1}{2}\sum_{\boldsymbol{k}} \langle c_{\boldsymbol{k}}| \, \mathbf{H}_{\boldsymbol{k}} \, |c_{\boldsymbol{k}}\rangle, \tag{6.1.8}$$

with $\langle c_{\boldsymbol{k}}| = \left(c^\dagger_{\boldsymbol{k}\uparrow},\ c^\dagger_{\boldsymbol{k}\downarrow},\ c_{-\boldsymbol{k}\uparrow},\ c_{-\boldsymbol{k}\downarrow}\right) = |c_{\boldsymbol{k}}\rangle^\dagger$; while $\mathcal{H}_0$ and $\mathbf{H}_{\boldsymbol{k}}$ are determined by writing out the sum over spins in eq. (6.1.7). This gives

$$\mathcal{H}_0 = \sum_{\boldsymbol{k}} \epsilon_{\boldsymbol{k}} + \frac{1}{2}\sum_{\boldsymbol{k},\sigma_1,\sigma_2} \Delta_{\boldsymbol{k}\sigma_1\sigma_2} b^\dagger_{\boldsymbol{k}\sigma_2\sigma_1}, \tag{6.1.9}$$

$$\mathbf{H}_{\boldsymbol{k}} = \begin{pmatrix} \epsilon_{\boldsymbol{k}} & 0 & \Delta_{\boldsymbol{k}\uparrow\uparrow} & \Delta_{\boldsymbol{k}\uparrow\downarrow} \\ 0 & \epsilon_{\boldsymbol{k}} & \Delta_{\boldsymbol{k}\downarrow\uparrow} & \Delta_{\boldsymbol{k}\downarrow\downarrow} \\ \Delta^\dagger_{\boldsymbol{k}\uparrow\uparrow} & \Delta^\dagger_{\boldsymbol{k}\downarrow\uparrow} & -\epsilon_{-\boldsymbol{k}} & 0 \\ \Delta^\dagger_{\boldsymbol{k}\uparrow\downarrow} & \Delta^\dagger_{\boldsymbol{k}\downarrow\downarrow} & 0 & -\epsilon_{-\boldsymbol{k}} \end{pmatrix}, \tag{6.1.10}$$

$$= \begin{pmatrix} \epsilon_{\boldsymbol{k}}\mathbb{1}_2 & \boldsymbol{\Delta}_{\boldsymbol{k}} \\ \boldsymbol{\Delta}^\dagger_{\boldsymbol{k}} & -\epsilon_{\boldsymbol{k}}\mathbb{1}_2 \end{pmatrix}. \tag{6.1.11}$$

In which the last equation was obtained by defining the $\boldsymbol{\Delta}_{\boldsymbol{k}}$ matrix, and using $\epsilon_{-\boldsymbol{k}} = \epsilon_{\boldsymbol{k}}$ as observed from eq. (3.1.7).

Proceed to diagonalise $\mathbf{H}_{\boldsymbol{k}}$ in eq. (6.1.10). In accordance with the form of the original basis $\langle c_{\boldsymbol{k}}|$, define

$$\begin{aligned} \boldsymbol{E}_{\boldsymbol{k}} &= \boldsymbol{U}_{\boldsymbol{k}}^{\dagger}\mathbf{H}_{\boldsymbol{k}}\boldsymbol{U}_{\boldsymbol{k}}, \\ &\equiv \operatorname{diag}\left(E_{\boldsymbol{k}}^{+},\ E_{\boldsymbol{k}}^{-},\ -E_{-\boldsymbol{k}}^{+}, -E_{-\boldsymbol{k}}^{-}\right) \end{aligned} \tag{6.1.12}$$

for $\boldsymbol{U}_{\boldsymbol{k}}$ unitary matrix. Thus, let the corresponding diagonalised operators be

$$\langle \gamma_{\boldsymbol{k}}| = \left(\gamma_{\boldsymbol{k}}^{+\dagger},\ \gamma_{\boldsymbol{k}}^{-\dagger},\ \gamma_{-\boldsymbol{k}}^{+},\ \gamma_{-\boldsymbol{k}}^{-}\right), \tag{6.1.13}$$

consisting of electron and hole states. Note that $\gamma_{\boldsymbol{k}}^{-\dagger} = (\gamma_{\boldsymbol{k}}^{-})^{\dagger} \neq (\gamma_{\boldsymbol{k}})^{-\dagger}$ and should be understood from the context.

Moreover, obtain expressions for the new particle energies $\boldsymbol{E}_{\boldsymbol{k}}$ from the characteristic equation (linear algebra). Using Mathematica [46], this gives

$$E_{\boldsymbol{k}}^{\eta} = \sqrt{\epsilon_{\boldsymbol{k}}^{2} + \frac{1}{2}\sum_{\sigma,\sigma'}\left|\Delta_{\boldsymbol{k}\sigma\sigma'}\right|^{2} + \frac{\eta}{2}\sqrt{A_{\boldsymbol{k}}}}, \tag{6.1.14}$$

in which $A_{\boldsymbol{k}}$ was defined for readability. Observe that $E_{\boldsymbol{k}}^{\eta} = E_{-\boldsymbol{k}}^{\eta}$ if $A_{\boldsymbol{k}} = A_{-\boldsymbol{k}}$, as $\epsilon_{\boldsymbol{k}} = \epsilon_{-\boldsymbol{k}}$, and $\sum_{\sigma,\sigma'}\left|\Delta_{-\boldsymbol{k}\sigma\sigma'}\right|^{2} = \sum_{\sigma,\sigma'}\left|-\Delta_{\boldsymbol{k}\sigma'\sigma}\right|^{2}$ from eq. (6.1.6). Furthermore, $A_{\boldsymbol{k}}$ is defined as follows

$$\begin{aligned} A_{\boldsymbol{k}} = &\left(\left|\Delta_{\boldsymbol{k}\uparrow\uparrow}\right|^{2} - \left|\Delta_{\boldsymbol{k}\downarrow\downarrow}\right|^{2}\right)^{2} + \left(\left|\Delta_{\boldsymbol{k}\uparrow\downarrow}\right|^{2} - \left|\Delta_{\boldsymbol{k}\downarrow\uparrow}\right|^{2}\right)^{2} \\ &+ 2\left(\left|\Delta_{\boldsymbol{k}\uparrow\uparrow}\right|^{2} + \left|\Delta_{\boldsymbol{k}\downarrow\downarrow}\right|^{2}\right)\left(\left|\Delta_{\boldsymbol{k}\uparrow\downarrow}\right|^{2} + \left|\Delta_{\boldsymbol{k}\downarrow\uparrow}\right|^{2}\right) \\ &+ 4\Delta_{\boldsymbol{k}\uparrow\uparrow}^{\dagger}\Delta_{\boldsymbol{k}\downarrow\downarrow}^{\dagger}\Delta_{\boldsymbol{k}\uparrow\downarrow}\Delta_{\boldsymbol{k}\downarrow\uparrow} + 4\Delta_{\boldsymbol{k}\uparrow\uparrow}\Delta_{\boldsymbol{k}\downarrow\downarrow}\Delta_{\boldsymbol{k}\uparrow\downarrow}^{\dagger}\Delta_{\boldsymbol{k}\downarrow\uparrow}^{\dagger}. \end{aligned} \tag{6.1.15}$$

Indeed we observe that $A_{\boldsymbol{k}} = A_{-\boldsymbol{k}}$ from the behaviour of the gap parameter under inversion of momentum, given in eq. (6.1.6). This leads $E_{\boldsymbol{k}}^{\eta} = E_{-\boldsymbol{k}}^{\eta}$ as well. Thus, the matrix product of the effective Hamiltonian in eq. (6.1.8) is diagonalised and may be written in sum notation as

$$\langle \gamma_{\boldsymbol{k}}|\, \boldsymbol{E}_{\boldsymbol{k}}\, |\gamma_{\boldsymbol{k}}\rangle = \sum_{\eta}\left(2E_{\boldsymbol{k}}^{\eta}\gamma_{\boldsymbol{k}}^{\eta\dagger}\gamma_{\boldsymbol{k}}^{\eta} - E_{\boldsymbol{k}}^{\eta}\right). \tag{6.1.16}$$

Resultingly, the mean field Hamiltonian becomes

$$\mathcal{H}_{\mathrm{MF}} = E_{0} + \sum_{\boldsymbol{k},\eta} E_{\boldsymbol{k}}^{\eta}\gamma_{\boldsymbol{k}}^{\eta\dagger}\gamma_{\boldsymbol{k}}^{\eta}, \tag{6.1.17}$$

with the constant

$$\begin{aligned} E_{0} &= \mathcal{H}_{0} - \frac{1}{2}\sum_{\boldsymbol{k},\eta} E_{\boldsymbol{k}}^{\eta}, \\ &= \sum_{\boldsymbol{k}}\epsilon_{\boldsymbol{k}} + \frac{1}{2}\sum_{\boldsymbol{k},\sigma_1,\sigma_2}\Delta_{\boldsymbol{k}\sigma_1\sigma_2}b_{\boldsymbol{k}\sigma_2\sigma_1}^{\dagger} - \frac{1}{2}\sum_{\boldsymbol{k},\eta} E_{\boldsymbol{k}}^{\eta}. \end{aligned} \tag{6.1.18}$$

Equation (6.1.17) is the diagonalised mean-field Hamiltonian, with the ground state energy given by the constant E_0.

Note also that $\mathcal{H}_{\text{MF}}$ has been rewritten in terms of free quasi-particles with excitation energy $E^{\eta}_{\boldsymbol{k}}$, defined in eq. (6.1.14). In this equation, we note that the elements $A_{\boldsymbol{k}}$ may be interpreted as an effect arising from the co-existence of spin-singlet and spin-triplet gaps. Furthermore, it is clear that the gap parameter $\Delta_{\boldsymbol{k}\sigma_1\sigma_2}$ indeed appears as a gap in the quasi-particle energy spectrum at the Fermi surface. This gap appears as a direct consequence of the finite statistical averages $b^{\dagger}_{\boldsymbol{k}\sigma_1\sigma_2}$; hence it is a *superconducting gap*.

Furthermore, these quasi-particles are referred to as Bogoliubov quasi-particles, or *Bogoliubons* [55, 56, 38]. Bogoliubons are superpositions of electron and hole states, such that exciting a Bogoliubon from the ground state corresponds to destroying a Cooper pair in the condensate below the Fermi level. In the case of topological superconductivity, these quasi-particles have equal electron and hole components, and are thus classified as Majorana fermions [12, 57]. We continue to study the energy spectrum $E^{\eta}_{\boldsymbol{k}}$ of the Bogoliubons. From its definition in eq. (6.1.14), we must first determine the gap equation. Thus, we proceed to determine $\Delta_{\boldsymbol{k}\sigma_1\sigma_2}$ by minimising the corresponding Helmholtz free energy of the system.

6.2 Gap equation

The gap equation is derived by initially postulating finite values for $\Delta_{\boldsymbol{k}\sigma_1\sigma_2}$ and subsequently determining them through the minimisation of the Helmholtz free energy F associated with our specific system. Our system provided by the free-Bogoliubon Hamiltonian in eq. (6.1.17) is grand canonical, and we obtain F from the corresponding grand partition function Z. We obtain Z following the general procedure presented in appendix D.1. By comparison with our Hamiltonian in eq. (6.1.17), we get

$$Z = e^{-\beta E_0} \prod_{\boldsymbol{k},\eta} \left(1 + e^{-\beta E^{\eta}_{\boldsymbol{k}}}\right). \tag{6.2.1}$$

$$F = E_0 - \frac{1}{\beta} \sum_{\boldsymbol{k},\eta} \ln\left(1 + e^{-\beta E^{\eta}_{\boldsymbol{k}}}\right), \tag{6.2.2}$$

with E_0 and $E^{\eta}_{\boldsymbol{k}}$ functions of $\Delta_{\boldsymbol{k}\sigma_1\sigma_2}$ as given by eq. (6.1.14). Note that $\beta = (k_B T)^{-1}$ is the inverse energy with k_B the Boltzmann constant and T the system temperature. Continue to minimise the Helmholtz free energy F in terms of $\Delta_{\boldsymbol{k}\sigma_1\sigma_2}$ for some $\boldsymbol{k}, \sigma_1, \sigma_2$. After some algebra, this gives the following expression for $b^{\dagger}_{\boldsymbol{k}\sigma_2\sigma_1}$

$$b^{\dagger}_{\boldsymbol{k}\sigma_2\sigma_1} = \sum_{\eta} \left(\frac{1}{2}\Delta^{\dagger}_{\boldsymbol{k}\sigma_1\sigma_2} + \eta B^{\dagger}_{\boldsymbol{k}\sigma_1\sigma_2}\right) \chi^{\eta}_{\boldsymbol{k}}, \tag{6.2.3}$$

with $B^{\dagger}_{\boldsymbol{k}\sigma_1\sigma_2} = \frac{1}{4\sqrt{A_{\boldsymbol{k}}}} \frac{\partial A_{\boldsymbol{k}}}{\partial \Delta_{\boldsymbol{k}\sigma_1\sigma_2}}$, and $\chi^{\eta}_{\boldsymbol{k}} = \frac{1}{2E^{\eta}_{\boldsymbol{k}}} \tanh\left(\frac{\beta E^{\eta}_{\boldsymbol{k}}}{2}\right)$. The full calculation may be followed in appendix D.2. Note however that $B_{\boldsymbol{k}\sigma_1\sigma_2}$ changes as $\Delta_{\boldsymbol{k}\sigma_1\sigma_2}$ under inversion of $\boldsymbol{k}$, following from the observation that $A_{\boldsymbol{k}} = A_{-\boldsymbol{k}}$ from its definition in eq. (6.1.15). Moreover, $\chi^{\eta}_{\boldsymbol{k}}$ is inversion symmetric with momentum, as $E^{\eta}_{\boldsymbol{k}}$.

Inserting the statistical average in eq. (6.2.3) into the gap function in eq. (6.1.5a) gives

$$\Delta_{\boldsymbol{k}\sigma_1\sigma_2} = -\sum_{\boldsymbol{k}',\sigma_3,\sigma_4} \bar{V}^{\sigma_1\sigma_2\sigma_3\sigma_4}_{\boldsymbol{k}'\boldsymbol{k}} \sum_{\eta} \left(\frac{1}{2}\Delta_{\boldsymbol{k}'\sigma_4\sigma_3} + \eta B_{\boldsymbol{k}'\sigma_4\sigma_3} \right) \chi^{\eta}_{\boldsymbol{k}'}, \tag{6.2.4}$$

the gap equation applying to this superconductor at the mean-field level. The factor $B_{\boldsymbol{k}\sigma_1\sigma_2}$ may be interpreted as $A_{\boldsymbol{k}}$; an effect arising from the co-existence of spin-triplet and spin-singlet gaps. We also note that this factor effectively may act as a shift in the gap parameter. Moreover, $\chi^{\eta}_{\boldsymbol{k}}$ may be interpreted as the ability of the system to create Cooper pairs; the Cooper pair susceptibility [54].

To eventually determine the symmetries of the superconducting state, it is convenient to define gap parameters with certain spin- and momentum symmetries. Define therefore the gap parameter odd and even in spin, respectively

$$\Delta^{O(s)}_{\boldsymbol{k}\uparrow\downarrow} \equiv \frac{\Delta_{\boldsymbol{k}\uparrow\downarrow} - \Delta_{\boldsymbol{k}\downarrow\uparrow}}{2}, \tag{6.2.5a}$$

$$\Delta^{E(s)}_{\boldsymbol{k}\uparrow\downarrow} \equiv \frac{\Delta_{\boldsymbol{k}\uparrow\downarrow} + \Delta_{\boldsymbol{k}\downarrow\uparrow}}{2}, \tag{6.2.5b}$$

corresponding to the gap for spin polarised singlet and triplet. Note that these parameters are respectively even and odd in momentum. This symmetry is a direct consequence of the behaviour of $\Delta_{\boldsymbol{k}\sigma_1\sigma_2}$ under inversion of momentum, as given in eq. (6.1.6).

Accordingly, define parameters with corresponding symmetries for $B_{\boldsymbol{k}\sigma_1\sigma_2}$

$$B^{O(s)}_{\boldsymbol{k}\uparrow\downarrow} \equiv \frac{B_{\boldsymbol{k}\uparrow\downarrow} - B_{\boldsymbol{k}\downarrow\uparrow}}{2}, \tag{6.2.6a}$$

$$B^{E(s)}_{\boldsymbol{k}\uparrow\downarrow} \equiv \frac{B_{\boldsymbol{k}\uparrow\downarrow} + B_{\boldsymbol{k}\downarrow\uparrow}}{2}. \tag{6.2.6b}$$

6.2.1 Matrix notation

For later convenience, we rewrite the gap equation in eq. (6.2.4) to matrix form. We write this in bra-ket notation, giving

$$|\Delta_{\boldsymbol{k}}\rangle \equiv -\sum_{\boldsymbol{k}'} \boldsymbol{\mathcal{V}}_{\boldsymbol{k}'\boldsymbol{k}} \sum_{\eta} \left(\frac{1}{2} |\Delta_{\boldsymbol{k}'}\rangle + \eta |B_{\boldsymbol{k}'}\rangle \right) \chi^{\eta}_{\boldsymbol{k}'}, \tag{6.2.7}$$

where $|\Delta_{\boldsymbol{k}}\rangle = \left(\Delta^{O(s)}_{\boldsymbol{k}\uparrow\downarrow},\ \Delta_{\boldsymbol{k}\uparrow\uparrow},\ \Delta_{\boldsymbol{k}\downarrow\downarrow},\ \Delta^{E(s)}_{\boldsymbol{k}\uparrow\downarrow}\right)^T$ and similarly for $|B_{\boldsymbol{k}}\rangle$. It remains to determine $\boldsymbol{\mathcal{V}}_{\boldsymbol{k}'\boldsymbol{k}}$ the matrix of coupling functions. For this purpose, write out the sum over spins in the gap equation in eq. (6.2.4). Then, for each element in $|\Delta_{\boldsymbol{k}}\rangle$, collect the coefficients of each element in $|\Delta_{\boldsymbol{k}'}\rangle$. This calculation may be followed in appendix D.3, leading

$$\boldsymbol{\mathcal{V}}_{\boldsymbol{k}'\boldsymbol{k}} = \begin{pmatrix} \widetilde{V}^{E(\boldsymbol{k}')E(\boldsymbol{k})}_{\boldsymbol{k}'\boldsymbol{k}} & \bar{V}^{\uparrow\downarrow\uparrow\uparrow E(\boldsymbol{k})}_{\boldsymbol{k}'\boldsymbol{k}} & \bar{V}^{\uparrow\downarrow\downarrow\downarrow E(\boldsymbol{k})}_{\boldsymbol{k}'\boldsymbol{k}} & \widetilde{V}^{O(\boldsymbol{k}')E(\boldsymbol{k})}_{\boldsymbol{k}'\boldsymbol{k}} \\ -2\bar{V}^{\uparrow\uparrow\uparrow\downarrow E(\boldsymbol{k}')}_{\boldsymbol{k}'\boldsymbol{k}} & \bar{V}^{\uparrow\uparrow\uparrow\uparrow}_{\boldsymbol{k}'\boldsymbol{k}} & \bar{V}^{\uparrow\uparrow\downarrow\downarrow}_{\boldsymbol{k}'\boldsymbol{k}} & 2\bar{V}^{\uparrow\uparrow\uparrow\downarrow O(\boldsymbol{k}')}_{\boldsymbol{k}'\boldsymbol{k}} \\ -2\bar{V}^{\downarrow\downarrow\uparrow\downarrow E(\boldsymbol{k}')}_{\boldsymbol{k}'\boldsymbol{k}} & \bar{V}^{\downarrow\downarrow\uparrow\uparrow}_{\boldsymbol{k}'\boldsymbol{k}} & \bar{V}^{\downarrow\downarrow\downarrow\downarrow}_{\boldsymbol{k}'\boldsymbol{k}} & 2\bar{V}^{\downarrow\downarrow\uparrow\downarrow O(\boldsymbol{k}')}_{\boldsymbol{k}'\boldsymbol{k}} \\ \widetilde{V}^{E(\boldsymbol{k}')O(\boldsymbol{k})}_{\boldsymbol{k}'\boldsymbol{k}} & \bar{V}^{\uparrow\downarrow\uparrow\uparrow O(\boldsymbol{k})}_{\boldsymbol{k}'\boldsymbol{k}} & \bar{V}^{\uparrow\downarrow\downarrow\downarrow O(\boldsymbol{k})}_{\boldsymbol{k}'\boldsymbol{k}} & \widetilde{V}^{O(\boldsymbol{k}')O(\boldsymbol{k})}_{\boldsymbol{k}'\boldsymbol{k}} \end{pmatrix}. \tag{6.2.8}$$

For brevity of notation, we refer the coupling matrix elements as $\boldsymbol{\mathcal{V}}_{\boldsymbol{k}'\boldsymbol{k}}[r, c]$ for some row and column $r, c \in \{1, 2, 3, 4\}$. These coupling functions are plotted in figs. 6.1 to 6.4 for $\mu/t = -5.9$ and $\mu/t = -5.43$, each when as a function of both $\boldsymbol{k}$ and $\boldsymbol{k}'$. We may compare fig. 6.1 with fig. 6.2 for $\mu/t = -5.9$, or fig. 6.3 with fig. 6.4 for $\mu/t = -5.43$, to confirm the symmetries in $\boldsymbol{k}$ and $\boldsymbol{k}'$ as indicated by the coupling function definitions in eq. (6.2.8). Moreover, we note that a comparison of the plots for $\mu/t = -5.9$ with $\mu/t = -5.43$ indicates that the magnitude of the coupling functions has increased in absolute value.

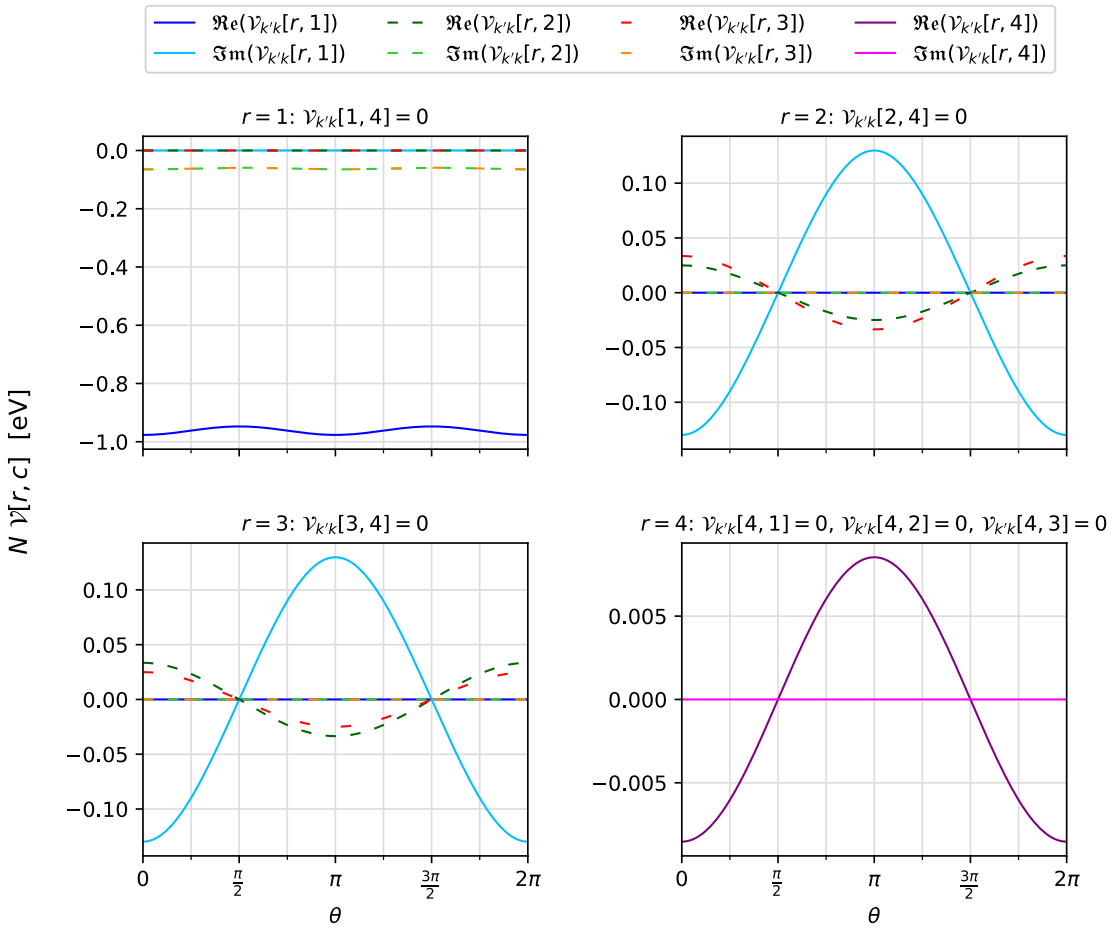

Figure 6.1: Coupling functions varying with the angle that $\boldsymbol{k}$ makes with the $\hat{\boldsymbol{k}}_x$ axis on the Fermi surface for $\mu/t = -5.9$. The figure shows five illustrations, whereas the topmost legends the plots of the following four graphs. Each graph plots the coupling functions of some row r of the coupling matrix $\boldsymbol{\mathcal{V}}_{\boldsymbol{k}'\boldsymbol{k}}$; in left-to-right reading conventions from $r = 1$ to $r = 4$. The title of each graph gives r and any null elements of the gap vector $\boldsymbol{\Delta}_{\boldsymbol{k}'\boldsymbol{k}}$. Other parameters are $\theta' = \pi$, $\bar{J}/J = 50$, $\bar{J}/t = 0.05$ and $S = 1$.

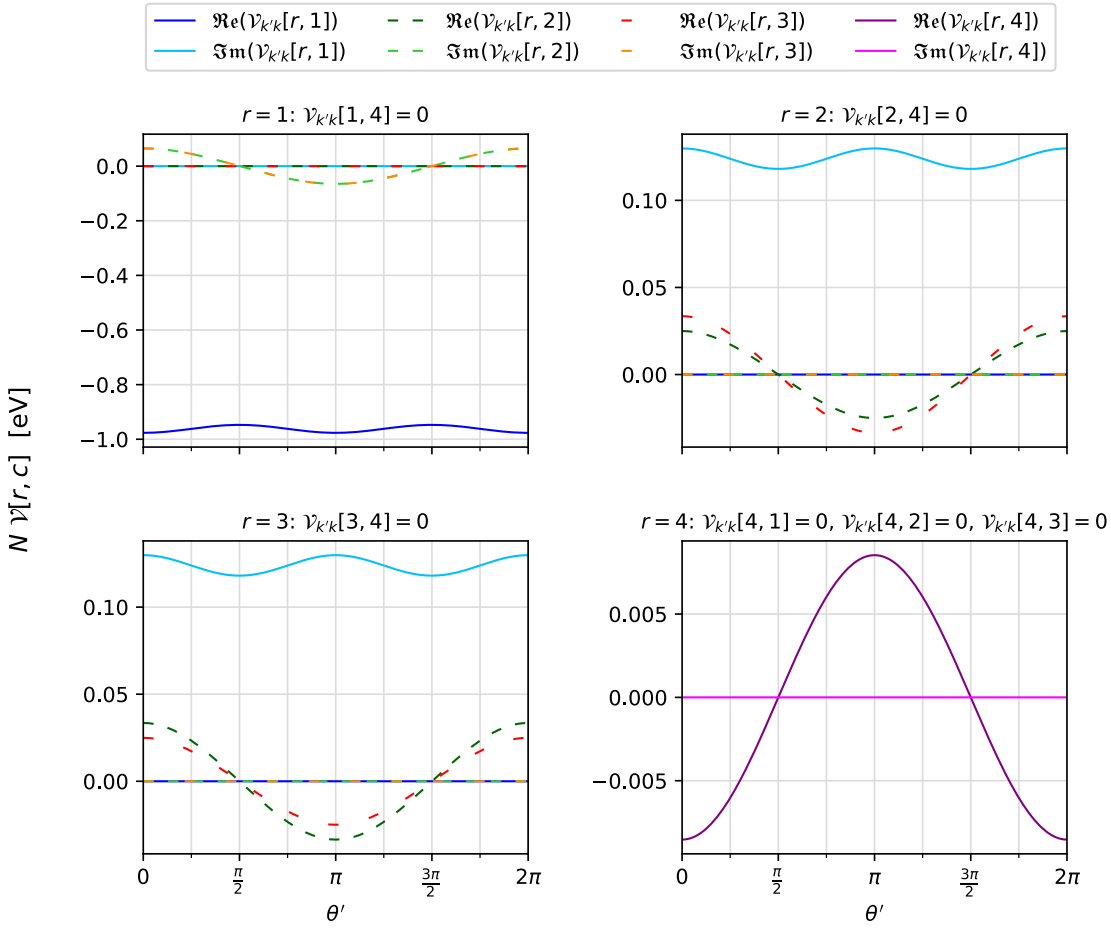

Figure 6.2: Coupling functions varying with the angle that $\boldsymbol{k}'$ makes with the $\hat{\boldsymbol{k}}_x$ axis on the Fermi surface for $\mu/t = -5.9$. The figure shows five illustrations, whereas the topmost legends the plots of the following four graphs. Each graph plots the coupling functions of some row r of the coupling matrix $\boldsymbol{\mathcal{V}}_{\boldsymbol{k}'\boldsymbol{k}}$; in left-to-right reading conventions from $r = 1$ to $r = 4$. The title of each graph gives r and any null elements of the gap vector $\boldsymbol{\Delta}_{\boldsymbol{k}'\boldsymbol{k}}$. Other parameters are $\theta = \pi$, $\bar{J}/J = 50$, $\bar{J}/t = 0.05$ and $S = 1$.

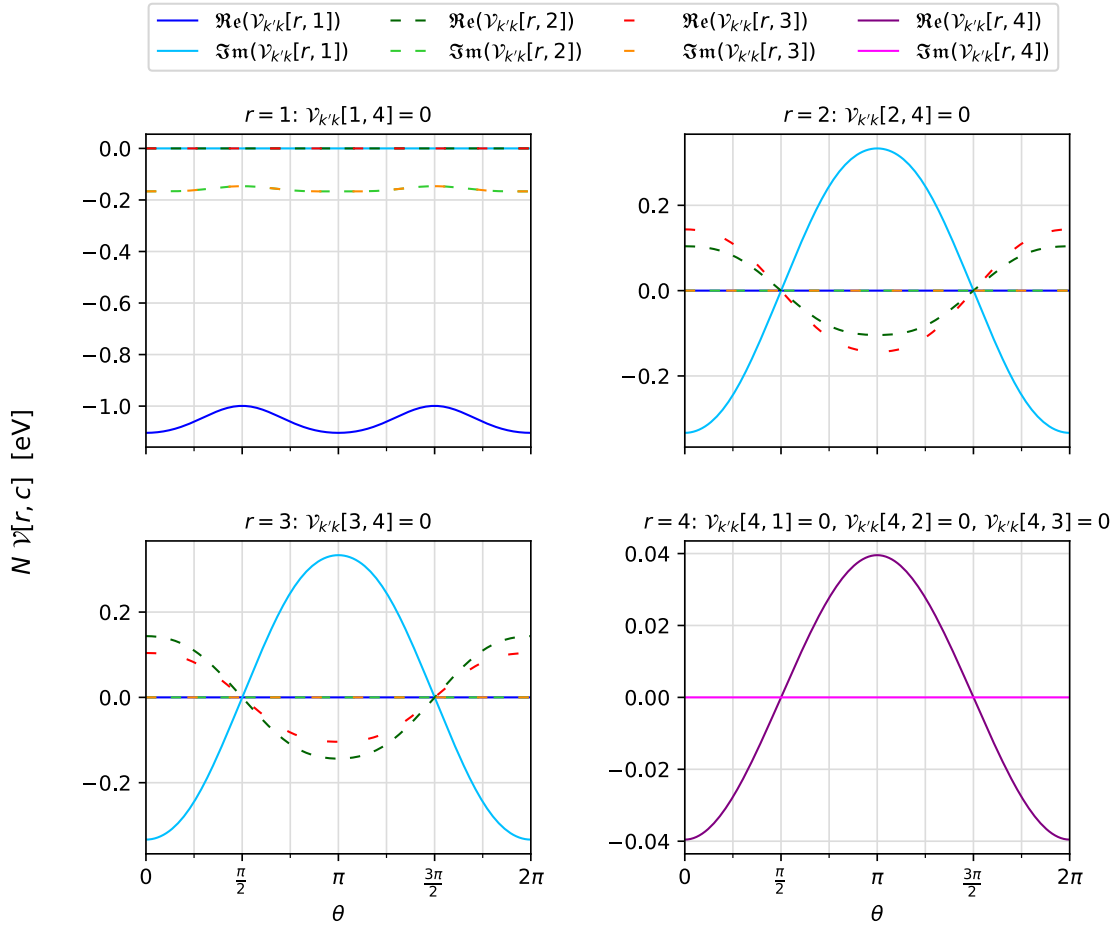

Figure 6.3: Corresponds to the plot in fig. 6.1 for a larger Fermi surface: coupling functions at the $\mu/t = -5.43$ Fermi surface plotted as a function of the angle θ spanning this surface. The figure shows five illustrations, whereas the topmost legends the plots of the following four graphs. Each graph plots the coupling functions of some row r of the coupling matrix $\boldsymbol{\mathcal{V}}_{\boldsymbol{k}'\boldsymbol{k}}$; in left-to-right reading conventions from $r = 1$ to $r = 4$. The title of each graph gives r and any null elements of the gap vector $\boldsymbol{\Delta}_{\boldsymbol{k}'\boldsymbol{k}}$. Other parameters are $\theta' = \pi$, $\bar{J}/J = 50$, $\bar{J}/t = 0.05$ and $S = 1$.

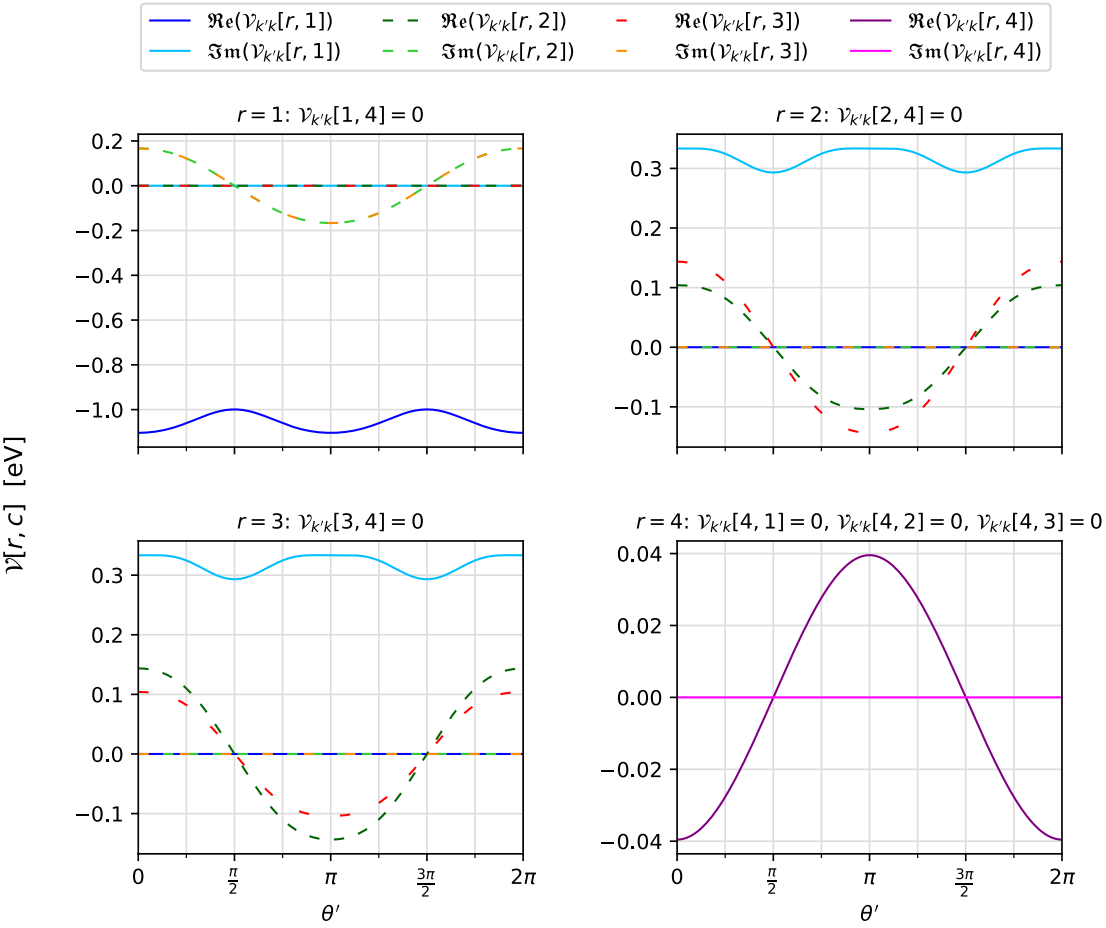

Figure 6.4: Corresponds to the plot in fig. 6.2 for a larger Fermi surface: coupling functions at the $\mu/t = -5.43$ Fermi surface plotted as a function of the angle θ' spanning this surface. The figure shows five illustrations, whereas the topmost legends the plots of the following four graphs. Each graph plots the coupling functions of some row r of the coupling matrix $\boldsymbol{\mathcal{V}}_{\boldsymbol{k'k}}$; in left-to-right reading conventions from $r = 1$ to $r = 4$. The title of each graph gives r and any null elements of the gap vector $\boldsymbol{\Delta}_{\boldsymbol{k'k}}$. Other parameters are $\theta = \pi$, $\bar{J}/J = 50$, $\bar{J}/t = 0.05$ and $S = 1$.

6.2.2 Linearised gap equation

To determine the superconducting gap, we consider the system at the superconducting state: let the temperature approach criticality from below $T \to T_c^-$ such that the Bogoliubon energy gap is small. Thus, we may approximate $E_{\boldsymbol{k}}^{\eta} \approx |\epsilon_{\boldsymbol{k}}|$ and thereby $\chi_{\boldsymbol{k}}^{\eta} \approx \chi_{\boldsymbol{k}} = (2|\epsilon_{\boldsymbol{k}}|)^{-1} \tanh(\beta_c |\epsilon_{\boldsymbol{k}}|/2)$. Thus, the integrand only depends on $\eta \in \{+,-\}$ in the second term $\eta \left| B_{\boldsymbol{k}}^{\dagger} \right\rangle$, leading this term at null and a factor 2 otherwise. Therefore, the linearised gap equation from eq. (6.2.4) may be written

$$\Delta_{\boldsymbol{k}\sigma_1\sigma_2} = -\sum_{\boldsymbol{k}',\sigma_3,\sigma_4} \bar{V}_{\boldsymbol{k}'\boldsymbol{k}}^{\sigma_1\sigma_2\sigma_3\sigma_4} \Delta_{\boldsymbol{k}'\sigma_4\sigma_3} \frac{1}{2|\epsilon_{\boldsymbol{k}'}|} \tanh\left(\frac{\beta_c |\epsilon_{\boldsymbol{k}'}|}{2}\right), \tag{6.2.9}$$

in which the pair-susceptibility was inserted for. Continue to write this equation more compactly, using the matrix notation in eq. (6.2.7). We write

$$|\Delta_{\boldsymbol{k}}\rangle [r] = -\sum_{\boldsymbol{k}',c} \boldsymbol{\mathcal{V}}_{\boldsymbol{k}'\boldsymbol{k}}[r,c] \, |\Delta_{\boldsymbol{k}'}\rangle [c] \frac{1}{2|\epsilon_{\boldsymbol{k}'}|} \tanh\left(\frac{\beta_c |\epsilon_{\boldsymbol{k}'}|}{2}\right), \tag{6.2.10}$$

in which $|\Delta_{\boldsymbol{k}}\rangle [r]$ is the rth element of $|\Delta_{\boldsymbol{k}}\rangle$. For brevity of notation, we let $|\Delta_{\boldsymbol{k}}\rangle [r] \equiv \Delta_{\boldsymbol{k}}$, and $\boldsymbol{\mathcal{V}}_{\boldsymbol{k}'\boldsymbol{k}}[r,c] \equiv V_{\boldsymbol{k}'\boldsymbol{k}}$ to write

$$\Delta_{\boldsymbol{k}} = -\sum_{\boldsymbol{k}'} V_{\boldsymbol{k}'\boldsymbol{k}} \Delta_{\boldsymbol{k}'} \frac{1}{2|\epsilon_{\boldsymbol{k}'}|} \tanh\left(\frac{\beta_c |\epsilon_{\boldsymbol{k}'}|}{2}\right). \tag{6.2.11}$$

Note that the elements $V_{\boldsymbol{k}'\boldsymbol{k}} = \boldsymbol{\mathcal{V}}_{\boldsymbol{k}'\boldsymbol{k}}[r,c]$ go as some linear combination of the effective interaction potential in eq. (5.3.3). As is, the effective interaction potentials are too complicated to solve the gap equation. For this reason, approximate the radial dependence of $V_{\boldsymbol{k}'\boldsymbol{k}}$ to be that at the Fermi surface: $V_{\boldsymbol{k}'\boldsymbol{k}} = V(k_F, \theta', \theta)$. Moreover, in accordance with the BCS theory, approximate to finite coupling functions only within region Ω covering a thin shell of width $2\omega_c$ around the Fermi surface. Here, ω_c is the maximum magnon energy: we study the range of energies for which the electrons may be excited by the magnons. The coupling functions are written

$$V_{\boldsymbol{k}'\boldsymbol{k}} \approx V(\theta', \theta) \Theta(\omega_c - |\epsilon_{\boldsymbol{k}}|) \Theta(\omega_c - |\epsilon_{\boldsymbol{k}'}|), \tag{6.2.12}$$

with $\Theta(x < 0) = 0$, $\Theta(x > 0) = 1$ the unit step function [58]. Additionally, $\theta = \arctan(k_y/k_x)$ the angle $\boldsymbol{k}$ makes with the $\hat{k}_x$-axis.

Assume a similar form of $\Delta_{\boldsymbol{k}}$, such that

$$\Delta_{\boldsymbol{k}} \approx \Delta(\theta) \Theta(\omega_c - |\epsilon_{\boldsymbol{k}}|). \tag{6.2.13}$$

In accordance with the aforementioned approximations, we must rewrite the sum over $\boldsymbol{k}'$ in eq. (6.2.11) into an integral

$$\sum_{\boldsymbol{k}'} \to \frac{N}{A_{\mathrm{eBZ}}} \int \mathrm{d}^2 k' \equiv \frac{N}{A_{\mathrm{eBZ}}} \int_0^{2\pi} \mathrm{d}\theta' \int k' \, \mathrm{d}k', \tag{6.2.14}$$

in which we may use $D(\epsilon)\,\mathrm{d}\epsilon = D(k')\,\mathrm{d}k'$ to transform the momentum-integral into an energy integral bounded at $\pm\omega_c$.

Thus, for any $\boldsymbol{k}, \boldsymbol{k}' \in \Omega$, the gap equation in eq. (6.2.11) on integral form becomes

$$\Delta(\theta) = -\frac{N}{A_{\mathrm{eBZ}}} \int_0^{2\pi} \mathrm{d}\theta' V(\theta', \theta)\Delta(\theta') \int_{-\omega_c}^{\omega_c} \mathrm{d}\epsilon \frac{k' D(\epsilon)}{D(k')} \frac{1}{2\,|\epsilon|} \tanh\left(\frac{\beta_c\,|\epsilon|}{2}\right). \tag{6.2.15}$$

Furthermore, we may approximate the density of states $D(\epsilon) \approx D(\mu) \equiv D_0$ by its value at the Fermi surface. Approximating the angular integral by a Fermi surface average gives

$$\int_0^{2\pi} \mathrm{d}\theta' V(\theta', \theta)\Delta(\theta') = 2\pi \langle V(\theta', \theta)\Delta(\theta')\rangle_{FS,\theta'} \tag{6.2.16a}$$

$$= \frac{2\pi}{N_\theta} \sum_i V(\theta_i', \theta)\Delta(\theta_i'), \tag{6.2.16b}$$

in which the last equality is used in numerical calculations for N_θ sampling points on the Fermi surface. We set $N_{\theta'} = N_\theta$ for simpler calculations. The integral form of the gap equation may then be written as

$$\Delta(\theta) = -\frac{N}{A_{\mathrm{eBZ}}} 2\pi \frac{k' D_0}{D(k')} \langle V(\theta', \theta)\Delta(\theta')\rangle_{FS,\theta'} \int_{-\omega_c}^{\omega_c} \mathrm{d}\epsilon \frac{1}{2\,|\epsilon|} \tanh\left(\frac{\beta_c\,|\epsilon|}{2}\right) \tag{6.2.17a}$$

$$= -N_0 \langle V(\theta', \theta)\Delta(\theta')\rangle_{FS,\theta'} \int_{-\omega_c}^{\omega_c} \mathrm{d}\epsilon \frac{1}{2\,|\epsilon|} \tanh\left(\frac{\beta_c\,|\epsilon|}{2}\right), \tag{6.2.17b}$$

in which the density of states per spin $N_0 = D_0/2$ was defined by inserting for $D(k')$ as given in eq. (3.1.11).

Continue to define the dimensionless coupling constant λ

$$\frac{1}{\lambda} = \int_{-\omega_c}^{\omega_c} \mathrm{d}\epsilon \frac{1}{2\,|\epsilon|} \tanh\left(\frac{\beta_c\,|\epsilon|}{2}\right). \tag{6.2.18}$$

In the weak-coupling limit $\lambda \ll 1$, we approximate [3]

$$\frac{1}{\lambda} = \ln\left(\frac{2}{\pi} e^\gamma \beta_c \omega_c\right), \tag{6.2.19}$$

in which $\gamma = 0.57721$ is the Euler–Mascheroni constant [59].From this relation, the critical temperature for superconductivity may be obtained $k_B T_c = \frac{2}{\pi} e^\gamma \omega_c e^{-1/\lambda}$.

Inserting the coupling constant into eq. (6.2.17b), we arrive at

$$\lambda\Delta(\theta) = -N_0 \langle V(\theta', \theta)\Delta(\theta')\rangle_{FS,\theta'}, \tag{6.2.20}$$

the linearised gap equation averaged over the Fermi surface. Numerically, we solve the eigenproblem

$$\left(-\frac{N_0}{N_\theta}\boldsymbol{\mathcal{V}} - \lambda \mathbb{1}_{4N_\theta}\right) |\Delta(\theta)\rangle = 0, \tag{6.2.21}$$

to obtain the coupling constant λ as the largest of the eigenvalues, and the corresponding eigenvectors $\Delta(\theta)$. Note that $\boldsymbol{\mathcal{V}}$ is now a $4N_\theta \times 4N_\theta$ matrix evolving in θ and θ'.

6.2.3 Solution of the linearised gap equation

The normalised gaps on the $\mu/t = -5.9$ and $\mu/t = -5.43$ Fermi surfaces are plotted in figs. 6.5 and 6.6, respectively. These figures illustrate the gaps relative the maximum absolute value of the imaginary and real part of the gap functions; defined as $\Delta_{\max} = \max\left(\mathfrak{Im}|\Delta_{\boldsymbol{k}}\rangle, \mathfrak{Re}|\Delta_{\boldsymbol{k}}\rangle\right)$. We may compare the gaps for $\mu/t = -5.9$ with those for $\mu/t = -5.43$ to note that the amplitudes of each gap is larger in the latter figure.

Moreover, it is clear from the figures that $\Delta^{O(s)}_{\uparrow\downarrow}$ dominates with an s-wave symmetry as it is nearly constant. However, the spin-triplet gap $\Delta^{E(s)}_{\uparrow\downarrow}$, comprising unpolarised (spinfull) electrons, is null. Nevertheless, the remaining spin-triplet gaps $\Delta_{\uparrow\uparrow}, \Delta_{\downarrow\downarrow}$, comprising spin-polarised (spinless) electrons, are ip_x-wave symmetric. This symmetry is identical to p_x- or p_y-wave symmetry. This similarity originates from the invariance of the gap functions under a phase shift. Furthermore, the imaginary nature of the spin-polarised gaps $\Delta_{\uparrow\uparrow}$ and $\Delta_{\downarrow\downarrow}$ may be transformed to real values by applying a phase shift, which concludes the argument.

Furthermore, a direct consequence of the purely real or imaginary gaps with the relation given in eq. (6.1.6), it is clear that the time reversal symmetry operator $\mathcal{T} = i\boldsymbol{\sigma}^y K$, for K the complex conjugation operator, leaves the gaps invariant.

We direct our attention to the dominant $\Delta^{O(s)}_{\boldsymbol{k}\uparrow\downarrow}$ gap function for spin-singlet Cooper pairs. The s-wave symmetry of this gap suggests that our superconductor shares notable similarities with the conventional BCS superconductor [3, 23]. Furthermore, the s-wave symmetry of this spin-singlet gap parameter indicates that the spin-singlet Cooper pairs have a uniform phase across the Fermi surface. This uniform phase suggests that the energy gap is isotropic: approximately the same amount of energy is required to break a spin-singlet Cooper pair across the entire Fermi surface.

Moreover, the spin-polarised gaps are imaginary, though not complex, displaying p-wave symmetry. Thus, it is clear that closing the polarised s-wave gap will leave the superconducting gap with nodes. This is sufficient information to conclude the topological characterisation of our superconductor: our system does not display strong topological superconductivity.

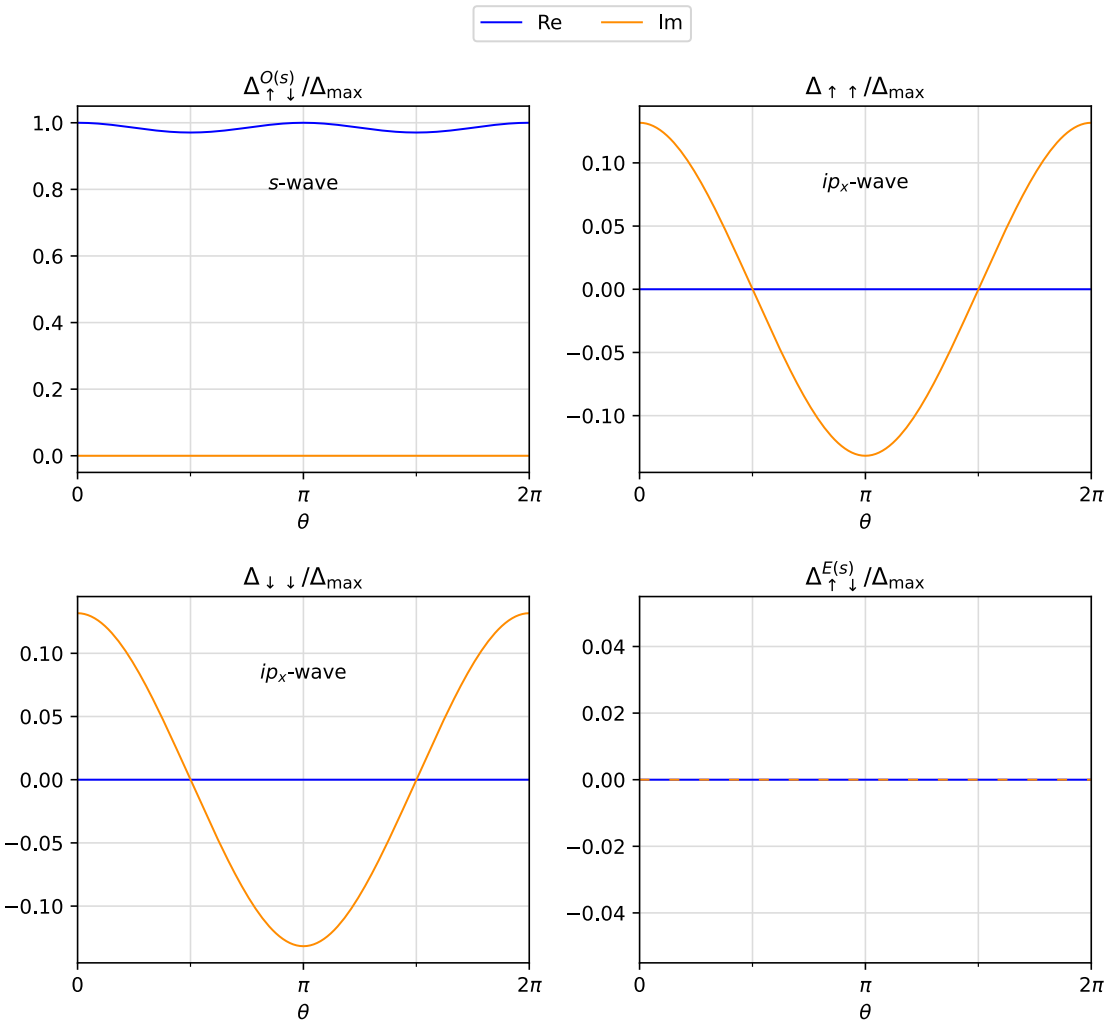

Figure 6.5: Four subplots of the gap functions at the at $\mu/t = -5.9$ Fermi surface plotted as a function of the angle θ spanning the surface. In left-to-right reading convention, we present $\Delta^{O(s)}_{\boldsymbol{k}\uparrow\downarrow}$, $\Delta_{\uparrow\uparrow}$, $\Delta_{\downarrow\downarrow}$, and $\Delta^{E(s)}_{\boldsymbol{k}\uparrow\downarrow}$ relative $\Delta_{\max}$. The gap function related to spin-singlet Cooper pairs $\Delta^{O(s)}_{\boldsymbol{k}\uparrow\downarrow}$ exhibits s-wave symmetry with maximum relative value (1). Moreover, the gap function for polarised spin-triplet Cooper pairs $\Delta_{\uparrow\uparrow}, \Delta_{\downarrow\downarrow}$ display ip_x-wave symmetry with relative amplitude just above 0.1. The last subplot shows the null gap function for the unpolarised spin-triplet Cooper pair $\Delta^{E(s)}_{\boldsymbol{k}\uparrow\downarrow}$. Thereby, the $\Delta^{O(s)}_{\boldsymbol{k}\uparrow\downarrow}$ gap manifests the dominating s-wave symmetry of the superconductor. The graphs are plotted with parameters $\mu/t = -5.9$, $\bar{J}/J = 50$, and $\bar{J}/t = 0.05$.

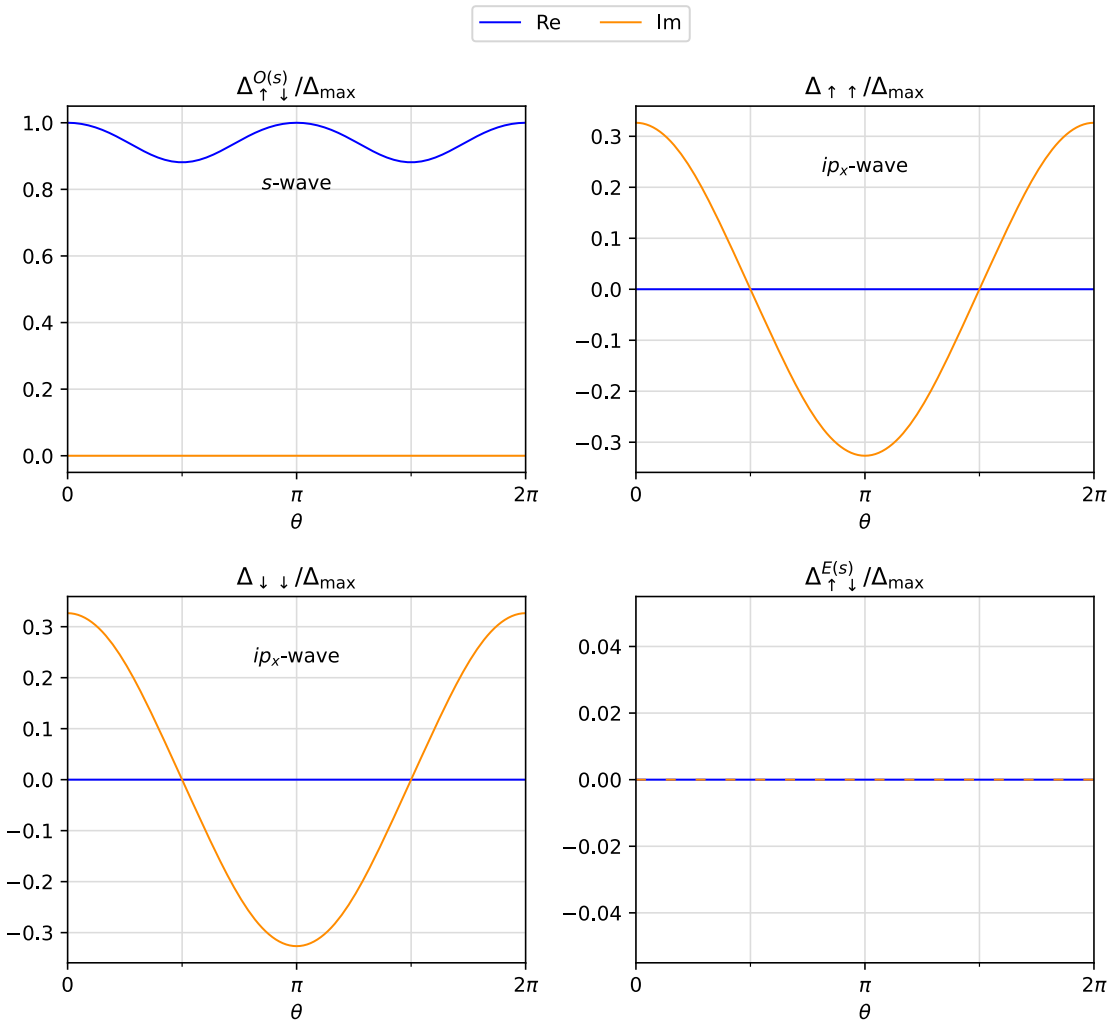

Figure 6.6: Corresponds to the plot in fig. 6.5 for a larger Fermi surface: four subplots of the gap functions at the at $\mu/t = -5.43$ Fermi surface plotted as a function of the angle θ spanning the surface. In left-to-right reading convention, we present $\Delta^{O(s)}_{\boldsymbol{k}\uparrow\downarrow}$, $\Delta_{\uparrow\uparrow}$, $\Delta_{\downarrow\downarrow}$, and $\Delta^{E(s)}_{\boldsymbol{k}\uparrow\downarrow}$ relative $\Delta_{\max}$. Each gap function display the same wave-symmetry as for the smaller Fermi surface in fig. 6.5, though with larger maximum amplitude. The graphs are plotted with parameters $\mu/t = -5.9$, $\bar{J}/J = 50$, and $\bar{J}/t = 0.05$, giving coupling constant $\lambda \approx 0.044$ and corresponding critical temperature $T_c \approx 0.094$mK.

6.2.4 Discussing possible origins of the results

It is worth noting that the parameters chosen for this thesis results a significantly low temperature of criticality at $T_c \approx 0.094$mK. Thus, various parameters must be adjusted to obtain an experimentally measurable temperature of criticality: we may note that the transition temperature $T_c \sim e^{-1/\lambda}$ increases with $\lambda \sim \bar{J}^2/J$. Nevertheless, we cannot choose these parameters blindly to obtain a higher T_c; we are afterall working on a physical system. For instance, increasing the ratio $\bar{J}/J$ could result in destabilising the ferromagnetic order, leading various of our previous assumptions invalid (for instance in the HP-transformation). On the other hand, literature has found the inclusion of a finite easy-axis anisotropy constant along the global spin $\hat{z}$-axis to reduce the magnon gap, thus effectively increasing the coupling of spins along that axis [1]. We may therefore speculate whether this would also apply for our SPFMI, such that a finite K possibly could increase our T_c. Note, however, that using a material with $K \neq 0$ changes the ground state of our SPFMI. Therefore, a recreation of these calculations with finite K could be of interest.

Moreover, a study of larger Fermi surfaces could also be of interest, though this would require more advanced calculations including the discarded terms in eq. (5.1.1).

We continue to investigate the nonexistence of strong topological superconductivity in our system. Specifically, we aim to understand the underlying factors responsible for yielding $\mathfrak{Re}\Delta_{\boldsymbol{k}\uparrow\uparrow} = 0$ and $\mathfrak{Re}\Delta_{\boldsymbol{k}\downarrow\downarrow} = 0$ by retracing our calculations of the gap functions. In the following discussion, we focus on retracing the calculations of $\Delta_{\boldsymbol{k}\uparrow\uparrow}$ to promote readability and ease of comprehension. As this discussion unfolds, we will comment on whether the results of this retracing will apply to that of $\Delta_{\boldsymbol{k}\downarrow\downarrow}$ as well.

First, recall that the gap functions were obtained from the eigenproblem of the matrix of coupling functions $\boldsymbol{\mathcal{V}}$ in eq. (6.2.21). We must therefore analyse the coupling functions to gain insight into the absence of strong topological superconductivity. The relevant coupling function connects $\Delta_{\boldsymbol{k}\uparrow\uparrow}$ to the dominant spin-singlet gap parameter $\Delta^{O(s)}_{\boldsymbol{k}\uparrow\downarrow}$. These functions correspond to the matrix element $\boldsymbol{\mathcal{V}}_{\boldsymbol{k}'\boldsymbol{k}}[2,1] \sim \bar{V}^{\uparrow\uparrow\uparrow\downarrow E(\boldsymbol{k}')}_{\boldsymbol{k}'\boldsymbol{k}}$ as obtained from eq. (6.2.8). Note that we are interested in the coupling function for various momenta $\boldsymbol{q}$ for scattering on the Fermi surface, so we must study the element $\boldsymbol{\mathcal{V}}_{\boldsymbol{k}'\boldsymbol{k}}[2,1]$ for varying $\boldsymbol{k}, \boldsymbol{k}' \in$ FS. As we may see in figs. 6.1 and 6.2, the coupling function $\boldsymbol{\mathcal{V}}_{\boldsymbol{k}'\boldsymbol{k}}[2,1]$ have negligible real part compared to the imaginary part. This was also confirmed numerically by comparing the maximum of real and imaginary parts of the coupling function, giving the real parts at a factor 10^{-30} of the imaginary part. In other words, the coupling function of interest $\boldsymbol{\mathcal{V}}_{\boldsymbol{k}'\boldsymbol{k}}[2,1]$ connecting $\Delta_{\boldsymbol{k}\uparrow\uparrow}$ to $\Delta^{O(s)}_{\boldsymbol{k}\uparrow\downarrow}$, is also purely imaginary. This result may be generalised to the coupling function $\boldsymbol{\mathcal{V}}_{\boldsymbol{k}'\boldsymbol{k}}[3,1]$ connecting $\Delta_{\boldsymbol{k}\downarrow\downarrow}$ to $\Delta^{O(s)}_{\boldsymbol{k}\uparrow\downarrow}$.

We continue to retrace our calculations by considering the definition of the coupling function $\boldsymbol{\mathcal{V}}_{\boldsymbol{k}'\boldsymbol{k}}[2,1]$. In the derivation of the coupling matrix in appendix D.3, we defined $\boldsymbol{\mathcal{V}}_{\boldsymbol{k}'\boldsymbol{k}}[2,1] = \bar{V}^{\uparrow\uparrow\downarrow\uparrow}_{\boldsymbol{k}'\boldsymbol{k}} - \bar{V}^{\uparrow\uparrow\uparrow\downarrow}_{\boldsymbol{k}'\boldsymbol{k}}$ in eq. (D.3.16b). Studying the real parts of barred effective potential in figs. 5.8a and 5.9a and the imaginary parts in figs. 5.8b and 5.9b, we note that the real parts $\mathfrak{Re}\bar{V}^{\uparrow\uparrow\downarrow\uparrow}_{\boldsymbol{k}'\boldsymbol{k}} \approx \mathfrak{Re}\bar{V}^{\uparrow\uparrow\uparrow\downarrow}_{\boldsymbol{k}'\boldsymbol{k}} \approx 0$ are both negligible

compared to the imaginary components. Numerical analysis confirms the smallness of the real parts at an order 10^{-12} compared to the imaginary parts. We contemplate whether larger values of these real parts would give rise to complex coupling functions, or if the real parts are equal and thus cancel to maintain the imaginary nature of the coupling functions. For this reason, we investigate the potential cancellation of $\mathfrak{Re}\bar{V}^{\uparrow\uparrow\downarrow\uparrow}_{\boldsymbol{k}'\boldsymbol{k}}$ and $\mathfrak{Re}\bar{V}^{\uparrow\uparrow\uparrow\downarrow}_{\boldsymbol{k}'\boldsymbol{k}}$. Through numerical analysis we ascertain that the real parts of these barred effective potentials are equal and thus cancel in the coupling function. Corresponding analysis for the imaginary parts of these terms imply that these are equal in magnitude though opposite in sign. These findings explain the imaginary nature of the $\boldsymbol{\mathcal{V}}_{\boldsymbol{k}'\boldsymbol{k}}[2,1]$ coupling function. In summary, the terms of the coupling function $\bar{V}^{\uparrow\uparrow\downarrow\uparrow}_{\boldsymbol{k}'\boldsymbol{k}}$ and $\bar{V}^{\uparrow\uparrow\uparrow\downarrow}_{\boldsymbol{k}'\boldsymbol{k}}$ are dominated by the imaginary part, while the real parts equate and thus cancel to leave an imaginary coupling function. This result also applies to the case for $\Delta_{\boldsymbol{k}\downarrow\downarrow}$.

Proceed to investigate the cancelling real parts of the coupling function by analysing the terms of the two barred effective potentials. Each of these potentials are defined by combining four variations of the unbarred effective potentials $V^{\sigma_1\sigma_2\sigma_3\sigma_4}_{\boldsymbol{k}\boldsymbol{k}'}$ in a linear manner, as provided in eq. (5.3.8). Thus, our curiosity is directed towards $8+8=16$ different unbarred potentials. For the sake of completeness, we present these definitions of the barred potentials

$$\bar{V}^{\uparrow\uparrow\downarrow\uparrow}_{\boldsymbol{k}\boldsymbol{k}'} \sim V^{\uparrow\uparrow\downarrow\uparrow}_{\boldsymbol{k}\boldsymbol{k}'} + V^{\uparrow\uparrow\uparrow\downarrow}_{(-\boldsymbol{k})(-\boldsymbol{k}')} - V^{\uparrow\uparrow\uparrow\downarrow}_{(-\boldsymbol{k})\boldsymbol{k}'} - V^{\uparrow\uparrow\downarrow\uparrow}_{\boldsymbol{k}(-\boldsymbol{k}')}, \tag{6.2.22a}$$

$$\bar{V}^{\uparrow\uparrow\uparrow\downarrow}_{\boldsymbol{k}\boldsymbol{k}'} \sim V^{\uparrow\uparrow\uparrow\downarrow}_{\boldsymbol{k}\boldsymbol{k}'} + V^{\uparrow\uparrow\downarrow\uparrow}_{(-\boldsymbol{k})(-\boldsymbol{k}')} - V^{\uparrow\uparrow\downarrow\uparrow}_{(-\boldsymbol{k})\boldsymbol{k}'} - V^{\uparrow\uparrow\uparrow\downarrow}_{\boldsymbol{k}(-\boldsymbol{k}')}. \tag{6.2.22b}$$

Flipping each spin gives the barred effective potentials embedded in $\Delta_{\boldsymbol{k}\downarrow\downarrow}$. Note that the terms of $\bar{V}^{\uparrow\uparrow\downarrow\uparrow}_{\boldsymbol{k}\boldsymbol{k}'}$ in eq. (6.2.22a) also appear in $\bar{V}^{\uparrow\uparrow\uparrow\downarrow}_{\boldsymbol{k}\boldsymbol{k}'}$ in eq. (6.2.22b) after an inversion of $\boldsymbol{q}$ $(\boldsymbol{k},\boldsymbol{k}')$. We analyse the relevant unbarred potentials numerically to study their nature. From this we find a notable resemblance between the barred effective potential and each of its unbarred terms: the real parts are again at an order 10^{-12} compared to the imaginary parts. Additionally, we observe that the real parts of the unbarred potentials are inversion symmetric about $\boldsymbol{q}$, i.e., under $(\boldsymbol{k},\boldsymbol{k}') \to (-\boldsymbol{k},-\boldsymbol{k}')$. Meanwhile, the imaginary parts of the unbarred potentials are odd under the inversion of $\boldsymbol{q}$. Further analysis requires consideration of the barred potentials in eq. (6.2.22) (and those with flipped spins), and that the coupling function $\boldsymbol{\mathcal{V}}_{\boldsymbol{k}'\boldsymbol{k}}[2,1]$ goes as the difference between these barred potentials. With the above results, we thereby understand that the real (imaginary) part of each term in $\bar{V}^{\uparrow\uparrow\downarrow\uparrow}_{\boldsymbol{k}\boldsymbol{k}'}$ is cancelled (doubled) by its momentum-inverted counterpart in $\bar{V}^{\uparrow\uparrow\uparrow\downarrow}_{\boldsymbol{k}\boldsymbol{k}'}$ when studying the coupling function. This is analogous to the case for $\Delta_{\boldsymbol{k}\downarrow\downarrow}$.

We may continue our quest to gain insight into the symmetries of the unbarred effective potential to understand why their real (imaginary) parts are inversion (anti)symmetric. Thereby, we study the definition of the unbarred effective potential at the Fermi surface, given in eq. (5.3.4). One might be inclined to proceed by analysing the enhancement factor $\mathcal{A}^{\sigma_1\sigma_2\sigma_3\sigma_4}_{\boldsymbol{q}\gamma\nu}$ as present in eq. (5.3.4a). However, note that these factors depend on the magnon-modes, and therefore rely on the numerical solutions to correctly sort the bands. Although the magnon dispersion relation along the high-symmetry points on the Billouin zone (fig. 5.3) is correctly

sorted, the method used cannot be generalised to any degenerate dispersion relation. This is due to the trial and fail procedure of obtaining the sorted bands. For this reason, studying the behaviour of the enhancement factor $\mathcal{A}^{\sigma_1\sigma_2\sigma_3\sigma_4}_{\boldsymbol{q}\gamma\nu}$ as it appears in the unbarred effective potential, is left beyond the scope of this paper and an encouraged outlook for future studies.

Consequently, we retrace the calculations further to study the unbarred effective potential as written in eq. (5.3.4c). This expression constitutes a sum over two sub-lattice indices L and L' in addition to the magnon modes γ. Therefore, consider first the unbarred effective potential for various sub-lattices L, i.e., $V^{\sigma_1\sigma_2\sigma_3\sigma_4}_{\boldsymbol{k}\boldsymbol{k}'}(L)\Big|_{\mathrm{FS}}$. In plotting these, we observe that the real parts are no longer negligible compared to the imaginary parts. On the other hand, the plots imply that there always exists a sub-lattice $\bar{L}$ for each sub-lattice L such that $V^{\sigma_1\sigma_2\sigma_3\sigma_4}_{\boldsymbol{k}\boldsymbol{k}'}(L)\Big|_{\mathrm{FS}} = -\,V^{\sigma_1\sigma_2\sigma_3\sigma_4}_{\boldsymbol{k}\boldsymbol{k}'}(\bar{L})\Big|_{\mathrm{FS}}$. These sets were numerically obtained as $\{(L,\bar{L})\} = \{(0,0);\ \mathcal{P}(1,4);\ \mathcal{P}(2,3);\ \mathcal{P}(5,9);\ \mathcal{P}(6,8);\ (7,7)\}$, where $\mathcal{P}$ is the permutation operator such that $\mathcal{P}(1,4) = \{(1,4);\ (4,1)\}$. These results are analogous to those for $\Delta_{\boldsymbol{k}\downarrow\downarrow}$. In result, each of the unbarred effective potentials embedded within both spin-polarised gap equations are pairwise equal for various sub-lattice indices.

The aforementioned results leave us inclined to study the unbarred effective potential as a function of both sub-lattices $V^{\sigma_1\sigma_2\sigma_3\sigma_4}_{\boldsymbol{k}\boldsymbol{k}'}(L,L')\Big|_{\mathrm{FS}}$. The purpose is then to investigate whether the aforementioned results extends to the set (L,L'). By numerical calculations, we observe that this is indeed the situation: there exists a set $(\bar{L},\bar{L}')$ for each (L,L') such that $V^{\sigma_1\sigma_2\sigma_3\sigma_4}_{\boldsymbol{k}\boldsymbol{k}'}(L,L')\Big|_{\mathrm{FS}} = -\,V^{\sigma_1\sigma_2\sigma_3\sigma_4}_{\boldsymbol{k}\boldsymbol{k}'}(\bar{L},\bar{L}')\Big|_{\mathrm{FS}}$. More detailed analysis shows that both the set $\{(L,\bar{L})\}$ and $\{(L',\bar{L}')\}$ are the same as that stated in the previous paragraph. These results were also applicable to the unbarred effective potentials of $\Delta_{\boldsymbol{k}\downarrow\downarrow}$. Thus we conclude that each of the unbarred effective potentials embedded within both spin-polarised gap equations are pairwise equal for various combinations of both sub-lattice indices L, L'.

Let us now shift our focus from this detailed information to a higher-level analysis to interpret this finding. Consider the definition of the unbarred effective potential as given in eq. (5.3.4c). From this, we may interpret the pairwise cancellation of this potential as a function of the sub-lattices $\{(L,\bar{L})\}$ and $\{(L',\bar{L}')\}$. We understand that the sum over magnon modes must be equivalent for these indices. A quick numerical check indicates that the unbarred effective potential for (L,L') termwise cancel that for $(\bar{L},\bar{L}')$. Thereby, we note the symmetries of our $g_{L\nu\sigma_1\sigma_2}$-functions in eq. (3.3.9), or equivalently, $g^{(n)}_{L\nu\sigma}$ in eq. (3.3.7). Due to the nature of our spiral-phase spin structure, $\psi_L = 0$, in addition to that there exists an angle $\vartheta_{\bar{L}}$ for each ϑ_L such that $\sin\vartheta_L = -\sin\vartheta_{\bar{L}}$ or $\cos\vartheta_L = -\cos\vartheta_{\bar{L}}$ while the other remains. From observation of $g^{(n)}_{L\nu\sigma}$ in eq. (3.3.7), we thus note that $g^1_{L\nu\uparrow} = -g^1_{\bar{L}\nu\downarrow}$, while $g^2_{L\nu\sigma} = -g^2_{\bar{L}\nu\sigma}$. On the other hand, for the terms in eq. (5.3.4c) to cancel, the product of these functions with the Bogoliubov transformation matrix elements must be cancelled. Thus, we understand that there are several aspects behind the pairwise cancellation of the unbarred effective potentials.

We may then continue to compare with the result in [1]. In their paper, they study a skyrmion spin-structure in which the azimuthal angle $\psi_L \in [0, 2\pi]$. We

discuss whether the $g^{(n)}_{L\nu\sigma}$-functions may equate for L and $\bar{L}$. By studying their spin-lattice structure, we note that also in that there always exist a spin of opposite x- or y-component for each spin. This suggests that the $g^{(n)}_{L\nu\sigma}$-functions indeed equate for L and some $\bar{L}$. Therefore, we conclude that the information we seek lies in the Bogoliubov transformation matrix elements $u_{\boldsymbol{q}L\gamma}$ and $v_{\boldsymbol{q}L\gamma}$.

Unfortunately, the Bogoliubov transformation matrix was obtained numerically without analytical expressions for its elements. An analytical expression for these elements $u_{\boldsymbol{q}L\gamma}$ and $v_{\boldsymbol{q}L\gamma}$ is crucial to develop a more detailed understanding of their nature. However, one must diagonalise a 20×20 matrix in eq. (3.2.23) to obtain these expressions. To avoid this tedious approach, one should instead investigate a magnetic system giving rise to fewer sub-lattices. This may either be obtained by considering a different crystal structure, or perhaps by choosing a finite strength for each component of the DMI-vector and the easy-axis anisotropy constant. With this we motivate future studies of analytically diagonalising the coplanar, non-collinear spin-phase magnet Hamiltonian with the aim to conclude whether the absence of strong topological superconductivity originates from this specific SPFMI, or whether the findings of this thesis extends to all coplanar spin-structures.

7 Conclusion and outlook

This masters thesis investigates the topological nature of the superconducting state arising at the interface of a bilayer comprising a normal metal and a spiral-phase ferromagnetic insulator. This system is studied in the framework of the Holstein-Primakoff transformation; the Bogoliubov transformation; and the Schrieffer-Wolff transformation. Several simplifications are made and implemented, such as the reduction of interactions within the magnet: the easy-axis anisotropy constant is set to null; only one component of the anti-symmetric exchange is finite; and the exchange coupling is diagonal. We study the system Hamiltonian in the mean-field limit, before solving the linearised superconducting gap equation. With the work presented in this thesis, we conclude that our system does not display strong topological superconductivity.

In conclusion, we understand that the nonexistence of strong topological superconductivity in our system arise from the inversion symmetry of the real parts of the unbarred effective potentials. Additionally, there seems to be sets of sub-lattices such that the real parts of these potentials pairwise cancel, while the imaginary parts remain. To gain a more solid understanding of why this situation occurs, one must study the elements of the Bogoliubov transformation matrix. For this reason, the analytic derivation of this transformation matrix remains as a highly interesting outlook. Therefore, we highly encourage future research on this bilayer though with an altered magnetic layer with fewer sub-lattices. From this, one may proceed to diagonalise the corresponding Hamiltonian analytically. The information embedded in this analytical expression may be interpreted to eventually conclude whether the bilayer of a normal metal and a coplanar, non-collinear ferromagnetic insulator may give rise to strong topological superconductivity.

Bibliography

1. Mæland K and Sudbø A. Topological Superconductivity Mediated by Skyrmionic Magnons. Phys. Rev. Lett. 2023 Apr; 130(15):156002. DOI: 10.1103/PhysRevLett.130.156002
2. Swain N, Shahzad M and Sengupta P. Atomic scale skyrmions and large topological Hall effect in a breathing-kagome lattice. 2022 Mar. arXiv: 2203.03359 [cond-mat.str-el]
3. Bardeen J, Cooper LN and Schrieffer JR. Theory of Superconductivity. Phys. Rev. 1957 Dec; 108(5):1175–204. DOI: 10.1103/PhysRev.108.1175
4. Kittel C. *Quantum Theory of Solids, 2nd Revised Edition*. John Wiley & Sons, Inc., 1991
5. Onnes HK. The Superconductivity of Mercury. Comm. Phys. Lab. Univ. Leiden, No.s 120-124. 1911
6. Meissner W and Ochsenfeld R. Ein neuer Effekt bei Eintritt der Supraleitfähigkeit [A new effect when superconductivity occurs]. German. Naturwissenschaften 1933 Nov; 21(44):787–8. DOI: 10.1007/BF01504252
7. Ginzburg VL and Landau LD. On the Theory of Superconductivity. *On Superconductivity and Superfluidity: A Scientific Autobiography*. Berlin, Heidelberg: Springer Berlin Heidelberg, 2009 :113–37. DOI: 10.1007/978-3-540-68008-6_4. Original work published in 1950
8. Ashcroft NW. Metallic Hydrogen: A High-Temperature Superconductor? Phys. Rev. Lett. 1968 Dec; 21(26):1748–9. DOI: 10.1103/PhysRevLett.21.1748
9. Sleight AW, Gillson JL and Bierstedt PE. High-temperature superconductivity in the $BaPb_{1-x}Bi_xO_3$ systems. Solid State Communications 1975 Jul; 17:27–8. DOI: 10.1016/0038-1098(75)90327-0
10. Bednorz JG and Müller KA. Possible high T_c superconductivity in the Ba-La-Cu-O system. Zeitschrift für Physik B Condensed Matter 1986 Apr; 64(2):189–93. DOI: 10.1007/BF01303701
11. Blundell SJ. *Superconductivity: A Very Short Introduction*. Oxford University Press, 2009 May. Chap. 10 What have superconductors ever done for us? Available from: https://academic.oup.com/book/830
12. Sato M and Ando Y. Topological superconductors: a review. Reports on Progress in Physics 2017 May; 80:076501. DOI: 10.1088/1361-6633/aa6ac7

13. Leijnse M and Flensberg K. Introduction to topological superconductivity and Majorana fermions. Semiconductor Science and Technology 2012 Nov; 27:124003. DOI: 10.1088/0268-1242/27/12/124003

14. Ladd TD et al. Quantum computers. Nature 2010 Mar; 464:45–53. DOI: 10.1038/nature08812

15. Devoret MH, Wallraff A and Martinis JM. Superconducting Qubits: A Short Review. 2004. arXiv: cond-mat/0411174 [cond-mat.mes-hall]

16. Landauer R. Irreversibility and Heat Generation in the Computing Process. IBM Journal of Research and Development 1961 Jul; 5:183–91. DOI: 10.1147/rd.53.0183

17. Bérut A et al. Experimental verification of Landauer's principle linking information and thermodynamics. Nature 2012 Mar; 483:187–9. DOI: 10.1038/nature10872

18. Montiel Ross OH. A Review of Quantum-Inspired Metaheuristics: Going From Classical Computers to Real Quantum Computers. IEEE Access 2019 Dec; 8:814–38. DOI: 10.1109/ACCESS.2019.2962155

19. Clarke J and Wilhelm FK. Superconducting quantum bits. Nature 2008 Jun; 453:1031–42. DOI: 10.1038/nature07128

20. Nayak C et al. Non-Abelian anyons and topological quantum computation. Reviews of Modern Physics 2008 Sep; 80:1083–159. DOI: 10.1103/RevModPhys.80.1083

21. Lahtinen V and Pachos J. A Short Introduction to Topological Quantum Computation. SciPost Physics 2017 Sep; 3. DOI: 10.21468/scipostphys.3.3.021

22. Gariglio S, Gabay M, Mannhart J and Triscone J. Interface superconductivity. Physica C: Superconductivity and its Applications. Superconducting Materials: Conventional, Unconventional and Undetermined 2015 Jul; 514:189–98. DOI: 10.1016/j.physc.2015.02.028

23. Nakosai S, Tanaka Y and Nagaosa N. Two-dimensional p-wave superconducting states with magnetic moments on a conventional s-wave superconductor. Physical Review B 2013 Nov; 88:180503. DOI: 10.1103/PhysRevB.88.180503

24. Chen W and Schnyder AP. Majorana edge states in superconductor-noncollinear magnet interfaces. Physical Review B 2015 Dec; 92:214502. DOI: 10.1103/PhysRevB.92.214502

25. Coey JMD. *Magnetism and Magnetic Materials*. Cambridge University Press, 2010 Mar

26. Sudbø A. Quantum Theory of Solids. Digitialized lecture notes for the course "TFY4210 - Quantum Theory of Many-Particle Systems" held by Prof. Asle Sudbø spring 2020. 2021

27. Mæland K, Røst HI, Wells JW and Sudbø A. Electron-magnon coupling and quasiparticle lifetimes on the surface of a topological insulator. Phys. Rev. B 2021 Sep; 104(12):125125. DOI: 10.1103/PhysRevB.104.125125

28. Tsallis C. Diagonalization methods for the general bilinear Hamiltonian of an assembly of bosons. Journal of Mathematical Physics 1978 Jan; 19:277–86. DOI: 10.1063/1.523549

29. Ricardo H. *A Modern Introduction to Linear Algebra*. Taylor & Francis Group, 2010. Chap. 3 Matrix Algebra:157–252

30. Hemmer PC. *Kvantemekanikk, 5. utgave [Quantum mechanics]*. Fagbokforlaget, 2005

31. Bernevig BA and Hughes TL. *Topological Insulators and Topological Superconductors*. Princeton University Press, 2013 Jul

32. Simmons GF. *Introduction to Topology and Modern Analysis*. McGraw-Hill New York, 1963. Chap. 3 Topological Spaces:91–109

33. Wilczek F. Majorana returns. Nature Physics 2009 Sep; 5:614–8. DOI: 10.1038/nphys1380

34. Stern A. Non-Abelian states of matter. Nature 2010 Mar; 464:187–93. DOI: 10.1038/nature08915

35. Freedman MH, Kitaev A, Larsen MJ and Wang Z. Topological Quantum Computation. 2002 Oct. DOI: 10.1090/S0273-0979-02-00964-3

36. Kitaev A. Fault-tolerant quantum computation by anyons. Annals of Physics 2003 Jan; 303:2–30. DOI: 10.1016/s0003-4916(02)00018-0

37. Joshi AW. *Elements of Group Theory for Physicists, 3rd edition*. John Wiley & Sons, Inc., 1988

38. Bogoljubov NN. On a new method in the theory of superconductivity. Il Nuovo Cimento (1955-1965) 1958 Mar; 7:794–805. DOI: 10.1007/BF02745585

39. Colpa J. Diagonalization of the quadratic boson Hamiltonian with zero modes: II. Physical. Physica A: Statistical Mechanics and its Applications 1986 Jan; 134:417–42. DOI: 10.1016/0378-4371(86)90057-9

40. Wilcox RM. Exponential Operators and Parameter Differentiation in Quantum Physics. Journal of Mathematical Physics 1967 Apr; 8:962–82. DOI: 10.1063/1.1705306

41. Dzyaloshinsky I. A thermodynamic theory of "weak" ferromagnetism of antiferromagnetics. Journal of Physics and Chemistry of Solids 1958; 4:241–55. DOI: 10.1016/0022-3697(58)90076-3

42. Moriya T. Anisotropic Superexchange Interaction and Weak Ferromagnetism. Phys. Rev. 1960 Oct; 120(1):91–8. DOI: 10.1103/PhysRev.120.91

43. Simon SH. *The Oxford Solid State Basics*. Oxford University Press, 2013

44. Coey JMD. *Magnetism and Magnetic Materials*. Cambridge University Press, 2009. Chap. 5 Ferromagnetism and exchange:128–94

45. Maplesoft, a division of Waterloo Maple Inc. Maple. Version 2019. Waterloo, Ontario, 1996. Available from: https://www.maplesoft.com/

46. Inc. WR. Mathematica, Version 13.3. Champaign, IL, 2023. Available from: https://www.wolfram.com/mathematica

47. Abnar S. Magnon-mediated interactions between electrons in a multi-band model. Unpublished project thesis. 2023

48. Kittel C. *Introduction to Solid State Physics*. John Wiley & Sons Inc, 2004

49. Van Hove L. The Occurrence of Singularities in the Elastic Frequency Distribution of a Crystal. Phys. Rev. 1953 Mar; 89(6):1189–93. DOI: 10.1103/PhysRev.89.1189

50. Van Rossum G and Drake Jr FL. Python reference manual. Centrum voor Wiskunde en Informatica Amsterdam, 1995

51. Virtanen P et al. SciPy 1.0: Fundamental Algorithms for Scientific Computing in Python. Nature Methods 2020; 17:261–72. DOI: 10.1038/s41592-019-0686-2

52. Sigrist M and Ueda K. Phenomenological theory of unconventional superconductivity. Rev. Mod. Phys. 1991 Apr; 63(2):239–311. DOI: 10.1103/RevModPhys.63.239

53. Nishimori H and Ortiz G. *Elements of Phase Transitions and Critical Phenomena*. Oxford University Press, 2011

54. Fossheim K and Sudbø A. *Superconductivity: Physics and Applications*. John Wiley & Sons, 2004. Chap. 4 The Superconducting State - an Electronic Condensate:79–122

55. Bardyn CE, Karzig T, Refael G and Liew TCH. Chiral Bogoliubov excitations in nonlinear bosonic systems. Physical Review B 2016 Jan; 93:020502. DOI: 10.1103/PhysRevB.93.020502

56. Matsui H et al. BCS-Like Bogoliubov Quasiparticles in High-T_c Superconductors Observed by Angle-Resolved Photoemission Spectroscopy. Physical Review Letters 2003 May; 90:217002. DOI: 10.1103/PhysRevLett.90.217002

57. Leijnse M and Flensberg K. Introduction to topological superconductivity and Majorana fermions. Semiconductor Science and Technology 2012 Nov; 27:124003. DOI: 10.1088/0268-1242/27/12/124003

58. Weber HJ and Arfken GB. *Essential Mathematical Methods for Physicists*. Academic Press, 2003. Chap. 15 Integral Transforms:689–755

59. Euler L. De Progressionibus harmonicis Obersavatioes. Trans. Latin by Aycock A. Commentarii academiae scientiarum Petropolitanae 1740; 7:150–61. Available from: http://eulerarchive.maa.org/backup/E043.html

Appendices

A | Bilayer model

A.1 Elements of the rotated interaction matrix

The lengthy elements of the rotated interaction matrix $\boldsymbol{W}_{ij}$ in eq. (3.2.9) are given by the following

$$\begin{aligned} W_{ij}^{xx} = &\Big(J_{ij}^{x}\cos\vartheta_i\cos\psi_i - D_{ij}^{y}\sin\vartheta_i - D_{ij}^{z}\cos\vartheta_i\sin\psi_i\Big)\cos\vartheta_j\cos\psi_j \\ &+\Big(J_{ij}^{y}\cos\vartheta_i\sin\psi_i + D_{ij}^{x}\sin\vartheta_i + D_{ij}^{z}\cos\vartheta_i\cos\psi_i\Big)\cos\vartheta_j\sin\psi_j \\ &+\Big(J_{ij}^{z}\sin\vartheta_i - D_{ij}^{x}\cos\vartheta_i\sin\psi_i + D_{ij}^{y}\cos\vartheta_i\cos\psi_i\Big)\sin\vartheta_j, \end{aligned} \tag{A.1.1}$$

$$\begin{aligned} W_{ij}^{xy} = &\Big(J_{ij}^{y}\cos\vartheta_i\sin\psi_i + D_{ij}^{x}\sin\vartheta_i + D_{ij}^{z}\cos\vartheta_i\cos\psi_i\Big)\cos\psi_j \\ &-\Big(J_{ij}^{x}\cos\vartheta_i\cos\psi_i - D_{ij}^{y}\sin\vartheta_i - D_{ij}^{z}\cos\vartheta_i\sin\psi_i\Big)\sin\psi_j, \end{aligned} \tag{A.1.2}$$

$$\begin{aligned} W_{ij}^{xz} = &\Big(J_{ij}^{x}\cos\vartheta_i\cos\psi_i - D_{ij}^{y}\sin\vartheta_i - D_{ij}^{z}\cos\vartheta_i\sin\psi_i\Big)\sin\vartheta_j\cos\psi_j \\ &+\Big(J_{ij}^{y}\cos\vartheta_i\sin\psi_i + D_{ij}^{x}\sin\vartheta_i + D_{ij}^{z}\cos\vartheta_i\cos\psi_i\Big)\sin\vartheta_j\sin\psi_j \\ &-\Big(J_{ij}^{z}\sin\vartheta_i - D_{ij}^{x}\cos\vartheta_i\sin\psi_i + D_{ij}^{y}\cos\vartheta_i\cos\psi_i\Big)\cos\vartheta_j, \end{aligned} \tag{A.1.3}$$

$$\begin{aligned} W_{ij}^{yx} = &\Big(J_{ij}^{y}\cos\psi_i - D_{ij}^{z}\sin\psi_i\Big)\cos\vartheta_j\sin\psi_j \\ &-\Big(J_{ij}^{x}\sin\psi_i + D_{ij}^{z}\cos\psi_i\Big)\cos\vartheta_j\cos\psi_j \\ &-\Big(D_{ij}^{y}\sin\psi_i + D_{ij}^{x}\cos\psi_i\Big)\sin\vartheta_j, \end{aligned} \tag{A.1.4}$$

$$\begin{aligned} W_{ij}^{yy} = &\Big(J_{ij}^{x}\sin\psi_i + D_{ij}^{z}\cos\psi_i\Big)\sin\psi_j \\ &+\Big(J_{ij}^{y}\cos\psi_i - D_{ij}^{z}\sin\psi_i\Big)\cos\psi_j, \end{aligned} \tag{A.1.5}$$

$$\begin{aligned} W_{ij}^{yz} = \quad & \Big(J_{ij}^{y}\cos\psi_i - D_{ij}^{z}\sin\psi_i\Big)\sin\vartheta_j\sin\psi_j \\ & - \Big(J_{ij}^{x}\sin\psi_i + D_{ij}^{z}\cos\psi_i\Big)\sin\vartheta_j\cos\psi_j \\ & + \Big(D_{ij}^{x}\cos\psi_i + D_{ij}^{y}\sin\psi_i\Big)\cos\vartheta_j, \end{aligned} \tag{A.1.6}$$

$$\begin{aligned} W_{ij}^{zx} = \quad & \Big(J_{ij}^{x}\sin\vartheta_i\cos\psi_i + D_{ij}^{y}\cos\vartheta_i - D_{ij}^{z}\sin\vartheta_i\sin\psi_i\Big)\cos\vartheta_j\cos\psi_j \\ & + \Big(J_{ij}^{y}\sin\vartheta_i\sin\psi_i - D_{ij}^{x}\cos\vartheta_i + D_{ij}^{z}\sin\vartheta_i\cos\psi_i\Big)\cos\vartheta_j\sin\psi_j \\ & - \Big(J_{ij}^{z}\cos\vartheta_i + D_{ij}^{x}\sin\vartheta_i\sin\psi_i - D_{ij}^{y}\sin\vartheta_i\cos\psi_i\Big)\sin\vartheta_j, \end{aligned} \tag{A.1.7}$$

$$\begin{aligned} W_{ij}^{zy} = \quad & \Big(J_{ij}^{y}\sin\vartheta_i\sin\psi_i - D_{ij}^{x}\cos\vartheta_i + D_{ij}^{z}\sin\vartheta_i\cos\psi_i\Big)\cos\psi_j \\ & - \Big(J_{ij}^{x}\sin\vartheta_i\cos\psi_i + D_{ij}^{y}\cos\vartheta_i - D_{ij}^{z}\sin\vartheta_i\sin\psi_i\Big)\sin\psi_j, \end{aligned} \tag{A.1.8}$$

$$\begin{aligned} W_{ij}^{zz} = \quad & \Big(J_{ij}^{x}\sin\vartheta_i\cos\psi_i + D_{ij}^{y}\cos\vartheta_i - D_{ij}^{z}\sin\vartheta_i\sin\psi_i\Big)\sin\vartheta_j\cos\psi_j \\ & + \Big(J_{ij}^{y}\sin\vartheta_i\sin\psi_i - D_{ij}^{x}\cos\vartheta_i + D_{ij}^{z}\sin\vartheta_i\cos\psi_i\Big)\sin\vartheta_j\sin\psi_j \\ & + \Big(J_{ij}^{z}\cos\vartheta_i + D_{ij}^{x}\sin\vartheta_i\sin\psi_i - D_{ij}^{y}\sin\vartheta_i\cos\psi_i\Big)\cos\vartheta_j. \end{aligned} \tag{A.1.9}$$

B Effective electron-electron interaction

B.1 Second quantisation of the effective interaction Hamiltonian

In this section, we second quantise the effective interaction Hamiltonian in eq. (3.3.2). For completeness, we revisit this Hamiltonian in the following

$$\mathcal{H}_{\text{e-m}}^{(L)} = -2\bar{J}_L \sum_{i\in L} \langle c_i| \boldsymbol{\sigma} |c_i\rangle \cdot \left(\boldsymbol{U}\left(\vartheta_L, \psi_L\right)^T \widetilde{\boldsymbol{S}}_{iL}\right). \tag{3.3.2 revisited}$$

The procedure of second quantising this equation includes two steps to obtain the particle operators explicit in our Hamiltonian. Frist, we must expand the matrix and vector products to obtain the Hamiltonian in terms of the electron operators. Then we proceed to apply the HP transformation in section 2.3 to also have the boson operators explicit in our expression.

We begin with rewriting the matrix product $\langle c_i| \boldsymbol{\sigma} |c_i\rangle$ elementwise along axis $\alpha \in \{x, y, z\}$, before inserting for the spinors

$$\begin{aligned}
\left(\langle c_i| \boldsymbol{\sigma} |c_i\rangle\right)^\alpha &= \langle c_i| \boldsymbol{\sigma}^\alpha |c_i\rangle && \text{(B.1.1a)}\\
&= \begin{pmatrix} c_{i\uparrow}^\dagger & c_{i\downarrow}^\dagger \end{pmatrix} \boldsymbol{\sigma}^\alpha \begin{pmatrix} c_{i\uparrow} \\ c_{i\downarrow} \end{pmatrix} && \text{(B.1.1b)}\\
&= \Big[c_{i\uparrow}^\dagger c_{i\uparrow} \delta_{\alpha,z} + c_{i\uparrow}^\dagger c_{i\downarrow} \left(\delta_{\alpha,x} - i\delta_{\alpha,y}\right) \\
&\qquad + c_{i\downarrow}^\dagger c_{i\uparrow} \left(\delta_{\alpha,x} + i\delta_{\alpha,y}\right) - c_{i\downarrow}^\dagger c_{i\downarrow} \delta_{\alpha,z} \Big]. && \text{(B.1.1c)}
\end{aligned}$$

in which the last line was obtained by inserting for the α-Pauli matrix, given by

$$\boldsymbol{\sigma}^\alpha = \begin{pmatrix} \delta_{\alpha,z} & \delta_{\alpha,x} - i\delta_{\alpha_y} \\ \delta_{\alpha,x} + i\delta_{\alpha,y} & -\delta_{\alpha,z} \end{pmatrix}. \tag{B.1.2}$$

Inserting for the elements in eq. (B.1.1c), the matrix product eventually becomes

$$\langle c_i| \boldsymbol{\sigma} |c_i\rangle = \begin{pmatrix} c_{i\uparrow}^\dagger c_{i\downarrow} + c_{i\downarrow}^\dagger c_{i\uparrow} & -i\left(c_{i\uparrow}^\dagger c_{i\downarrow} - c_{i\downarrow}^\dagger c_{i\uparrow}\right) & c_{i\uparrow}^\dagger c_{i\uparrow} - c_{i\downarrow}^\dagger c_{i\downarrow} \end{pmatrix}. \tag{B.1.3}$$

It remains to expand the product $\boldsymbol{U}_L^T \widetilde{\boldsymbol{S}}_{iL}$ before finalising the first step. With the rotation matrix given by eq. (3.2.7), we get

$$\boldsymbol{U}_L^T \widetilde{\boldsymbol{S}}_{iL} = \begin{pmatrix} \cos\vartheta_L \cos\psi_L \widetilde{S}^x_{iL} - \sin\psi_L \widetilde{S}^y_{iL} + \sin\vartheta_L \cos\psi_L \widetilde{S}^z_{iL} \\ \cos\vartheta_L \sin\psi_L \widetilde{S}^x_{iL} + \cos\psi_L \widetilde{S}^y_{iL} + \sin\vartheta_L \sin\psi_L \widetilde{S}^z_{iL} \\ -\sin\vartheta_L \widetilde{S}^x_{iL} + \cos\vartheta_L \widetilde{S}^z_{iL} \end{pmatrix}. \tag{B.1.4}$$

Inserting the results in eq. (B.1.3) and eq. (B.1.4) into the Hamiltonian in eq. (3.3.2 revisited), we easily see that

$$\begin{aligned} \mathcal{H}^{(L)}_{\text{e-m}} = -2\bar{J}_L \sum_{i\in L} \Big[& \left(c^\dagger_{i\uparrow} c_{i\downarrow} + c^\dagger_{i\downarrow} c_{i\uparrow}\right) \Big(\cos\vartheta_L \cos\psi_L \widetilde{S}^x_{iL} - \sin\psi_L \widetilde{S}^y_{iL} \\ & \qquad + \sin\vartheta_L \cos\psi_L \widetilde{S}^z_{iL} \Big) \\ & - i \left(c^\dagger_{i\uparrow} c_{i\downarrow} - c^\dagger_{i\downarrow} c_{i\uparrow}\right) \Big(\cos\vartheta_L \sin\psi_L \widetilde{S}^x_{iL} + \cos\psi_L \widetilde{S}^y_{iL} \\ & \qquad + \sin\vartheta_L \sin\psi_L \widetilde{S}^z_{iL} \Big) \\ & + \left(c^\dagger_{i\uparrow} c_{i\uparrow} - c^\dagger_{i\downarrow} c_{i\downarrow}\right) \Big(-\sin\vartheta_L \widetilde{S}^x_{iL} + \cos\vartheta_L \widetilde{S}^z_{iL} \Big) \Big]. \end{aligned} \tag{B.1.5}$$

Continue to write this expression more compact by introducing a sum over spins σ as in the following

$$\begin{aligned} \mathcal{H}^{(L)}_{\text{e-m}} = -2\bar{J}_L \sum_{i\in L} \sum_{\sigma} \Big[& c^\dagger_{i\sigma} c_{i(-\sigma)} \Big(\cos\vartheta_L \cos\psi_L \widetilde{S}^x_{iL} - \sin\psi_L \widetilde{S}^y_{iL} + \sin\vartheta_L \cos\psi_L \widetilde{S}^z_{iL} \Big) \\ & - i\sigma c^\dagger_{i\sigma} c_{i(-\sigma)} \Big(\cos\vartheta_L \sin\psi_L \widetilde{S}^x_{iL} + \cos\psi_L \widetilde{S}^y_{iL} + \sin\vartheta_L \sin\psi_L \widetilde{S}^z_{iL} \Big) \\ & + \sigma c^\dagger_{i\sigma} c_{i\sigma} \Big(-\sin\vartheta_L \widetilde{S}^x_{iL} + \cos\vartheta_L \widetilde{S}^z_{iL} \Big) \Big]. \end{aligned} \tag{B.1.6}$$

Eventually, we seek to apply the HP transformation, given by

$$\widetilde{S}^z_{iL} = S - a^\dagger_{iL} a_{iL}, \tag{B.1.7a}$$

$$\widetilde{S}^\beta_{iL} = \frac{1}{2(\delta_{\beta,x} + i\delta_{\beta,y})} \left(\widetilde{S}^+_{iL} + (\delta_{\beta,x} - \delta_{\beta,y}) \widetilde{S}^-_{iL} \right), \tag{B.1.7b}$$

$$\widetilde{S}^+_{iL} \approx \sqrt{2S} a_{iL} \tag{B.1.7c}$$

$$= \left(\widetilde{S}^-_{iL}\right)^\dagger, \tag{B.1.7d}$$

analogous to that presented in section 2.3.

Consider then the integrand of eq. (B.1.6), and let this be denoted I. We proceed to insert for $\widetilde{S}^\alpha$, eventually obtaining

$$
\begin{aligned}
I =& c^\dagger_{i\sigma}c_{i(-\sigma)}\cos\vartheta_L\cos\psi_L\frac{1}{2}\left(\widetilde{S}^+_{iL}+\widetilde{S}^-_{iL}\right) - c^\dagger_{i\sigma}c_{i(-\sigma)}\sin\psi_L\frac{1}{2i}\left(\widetilde{S}^+_{iL}-\widetilde{S}^-_{iL}\right)\\
&+ c^\dagger_{i\sigma}c_{i(-\sigma)}\sin\vartheta_L\cos\psi_L\left(S-a^\dagger_{iL}a_{iL}\right) - i\sigma c^\dagger_{i\sigma}c_{i(-\sigma)}\cos\vartheta_L\sin\psi_L\frac{1}{2}\left(\widetilde{S}^+_{iL}+\widetilde{S}^-_{iL}\right)\\
&- i\sigma c^\dagger_{i\sigma}c_{i(-\sigma)}\cos\psi_L\frac{1}{2i}\left(\widetilde{S}^+_{iL}-\widetilde{S}^-_{iL}\right) - i\sigma c^\dagger_{i\sigma}c_{i(-\sigma)}\sin\vartheta_L\sin\psi_L\left(S-a^\dagger_{iL}a_{iL}\right)\\
&- \sigma c^\dagger_{i\sigma}c_{i\sigma}\sin\vartheta_L\frac{1}{2}\left(\widetilde{S}^+_{iL}+\widetilde{S}^-_{iL}\right) + \sigma c^\dagger_{i\sigma}c_{i\sigma}\cos\vartheta_L\left(S-a^\dagger_{iL}a_{iL}\right)
\end{aligned}
\tag{B.1.8a}
$$

$$
\begin{aligned}
\Rightarrow& c^\dagger_{i\sigma}c_{i(-\sigma)}\cos\vartheta_L\cos\psi_L\frac{1}{2}\left(\widetilde{S}^+_{iL}+\widetilde{S}^-_{iL}\right)\\
&+ c^\dagger_{i\sigma}c_{i(-\sigma)}\sin\vartheta_L\cos\psi_L\left(S-a^\dagger_{iL}a_{iL}\right)\\
&- \sigma c^\dagger_{i\sigma}c_{i(-\sigma)}\cos\psi_L\frac{1}{2}\left(\widetilde{S}^+_{iL}-\widetilde{S}^-_{iL}\right)\\
&- \sigma c^\dagger_{i\sigma}c_{i\sigma}\sin\vartheta_L\frac{1}{2}\left(\widetilde{S}^+_{iL}+\widetilde{S}^-_{iL}\right)\\
&+ \sigma c^\dagger_{i\sigma}c_{i\sigma}\cos\vartheta_L\left(S-a^\dagger_{iL}a_{iL}\right),
\end{aligned}
\tag{B.1.8b}
$$

in which the imaginary parts were discarded to obtain the second part.

Thus, we may proceed to insert for the spin ladder operators $\widetilde{S}^\pm_{iL}$ to obtain

$$
\begin{aligned}
I \approx& \frac{\sqrt{2S}}{2}\Big[c^\dagger_{i\sigma}c_{i(-\sigma)}\cos\vartheta_L\cos\psi_L\frac{1}{2}\left(a_{iL}+a^\dagger_{iL}\right)\\
&\qquad - \sigma c^\dagger_{i\sigma}c_{i(-\sigma)}\cos\psi_L\frac{1}{2}\left(a_{iL}-a^\dagger_{iL}\right)\\
&\qquad - \sigma c^\dagger_{i\sigma}c_{i\sigma}\sin\vartheta_L\frac{1}{2}\left(a_{iL}+a^\dagger_{iL}\right)\Big]\\
&+ \left(\sigma c^\dagger_{i\sigma}c_{i\sigma}\cos\vartheta_L + c^\dagger_{i\sigma}c_{i(-\sigma)}\sin\vartheta_L\cos\psi_L\right)\left(S-a^\dagger_{iL}a_{iL}\right),
\end{aligned}
\tag{B.1.9}
$$

which eventually gives the Hamiltonian

$$
\begin{aligned}
\mathcal{H}^{(L)}_{\text{e-m}} =& -\sqrt{2S}\bar{J}_L\sum_{i\in L}\sum_\sigma\Big\{\Big[c^\dagger_{i\sigma}c_{i(-\sigma)}\cos\vartheta_L\cos\psi_L\frac{1}{2}\left(a_{iL}+a^\dagger_{iL}\right)\\
&\qquad - \sigma c^\dagger_{i\sigma}c_{i(-\sigma)}\cos\psi_L\frac{1}{2}\left(a_{iL}-a^\dagger_{iL}\right)\\
&\qquad - \sigma c^\dagger_{i\sigma}c_{i\sigma}\sin\vartheta_L\frac{1}{2}\left(a_{iL}+a^\dagger_{iL}\right)\Big]\\
&+ 2\left(\sigma c^\dagger_{i\sigma}c_{i\sigma}\cos\vartheta_L + c^\dagger_{i\sigma}c_{i(-\sigma)}\sin\vartheta_L\cos\psi_L\right)\left(S-a^\dagger_{iL}a_{iL}\right)\Big\}.
\end{aligned}
\tag{B.1.10}
$$

Note that due to the sum over spins, each term in this Hamiltonian may be formulated with the addition of an hermitian conjugate term. Nevertheless, eq. (B.1.10) is the second quantised effective interaction Hamiltonian, which concludes this calculation.

B.2 Explicit Umklapp in Fourier transform

We Fourier transform the operator products present in eq. (3.3.3) using the adjusted version transformations in eq. (3.3.4) to explicitly include Umklapp processes. There are two operator products of interest: $a_{iL}c^\dagger_{i\sigma}c_{i\tilde{\sigma}}$ and $a^\dagger_{iL}a_{iL}c^\dagger_{i\sigma}c_{i\tilde{\sigma}}$ for $\tilde{\sigma} = \pm\sigma$. Consider first the former operator product, summed over $i \in L$.

$$\sum_{i\in L} a_{iL}c^\dagger_{i\sigma}c_{i\tilde{\sigma}} = \frac{1}{\sqrt{N_L N^2}} \sum_{i\in L} \sum_{\boldsymbol{q},\boldsymbol{k},\boldsymbol{k}'}^{\mathrm{mBZ}} \sum_{\nu,\nu'} a_{\boldsymbol{q}L}c^\dagger_{\boldsymbol{k}'+\boldsymbol{Q}_{\nu'},\sigma}c_{\boldsymbol{k}+\boldsymbol{Q}_\nu,\tilde{\sigma}} e^{-i(\boldsymbol{q}-\boldsymbol{k}'-\boldsymbol{Q}_{\nu'}+\boldsymbol{k}+\boldsymbol{Q}_\nu)\cdot\boldsymbol{r}_i}. \quad \text{(B.2.1)}$$

Due to the symmetry of the lattice, we may write $e^{-i(\boldsymbol{Q}_\nu-\boldsymbol{Q}_{\nu'})\cdot\boldsymbol{r}_i} = e^{-i(\boldsymbol{Q}_\nu-\boldsymbol{Q}_{\nu'})\cdot\boldsymbol{r}_L}$ and pull it outside the sum over i. Doing this results

$$\sum_{i\in L} a_{iL}c^\dagger_{i\sigma}c_{i\tilde{\sigma}} = \frac{1}{\sqrt{N_L N^2}} \sum_{\nu,\nu'} e^{-i(\boldsymbol{Q}_\nu-\boldsymbol{Q}_{\nu'})\cdot\boldsymbol{r}_L} \sum_{\boldsymbol{q},\boldsymbol{k},\boldsymbol{k}'}^{\mathrm{mBZ}} a_{\boldsymbol{q}L}c^\dagger_{\boldsymbol{k}'+\boldsymbol{Q}_{\nu'},\sigma}c_{\boldsymbol{k}+\boldsymbol{Q}_\nu,\tilde{\sigma}} \sum_{i\in L} e^{-i(\boldsymbol{q}-\boldsymbol{k}'+\boldsymbol{k})\cdot\boldsymbol{r}_i}. \quad \text{(B.2.2)}$$

With the requirement of convergence, we write $e^{-i(\boldsymbol{q}-\boldsymbol{k}'+\boldsymbol{k})\cdot\boldsymbol{r}_i} = \delta_{\boldsymbol{k}',\boldsymbol{k}+\boldsymbol{q}}$, such that the integrand becomes i-independent, leading $\sum_{i\in L} = N_L$. Thus, eq. (B.2.2) may be written as the following

$$\sum_{i\in L} a_{iL}c^\dagger_{i\sigma}c_{i\tilde{\sigma}} = \frac{\sqrt{N_L}}{N} \sum_{\nu,\nu'} e^{-i(\boldsymbol{Q}_\nu-\boldsymbol{Q}_{\nu'})\cdot\boldsymbol{r}_L} \sum_{\boldsymbol{q},\boldsymbol{k}}^{\mathrm{mBZ}} a_{\boldsymbol{q}L}c^\dagger_{\boldsymbol{k}+\boldsymbol{q}+\boldsymbol{Q}_{\nu'},\sigma}c_{\boldsymbol{k}+\boldsymbol{Q}_\nu,\tilde{\sigma}}. \quad \text{(B.2.3)}$$

We proceed to rewrite the momentum index of the daggered electron operator such that both electron operator momenta have an added momentum of $\boldsymbol{Q}_\nu$. Generally, we may write $\boldsymbol{Q}_{\nu'} - \boldsymbol{Q}_\nu = \boldsymbol{Q}_{\nu''} + \boldsymbol{G}_u$ for $\{\boldsymbol{G}_u\}$ the set of electron reciprocal lattice vectors. From this definition of $\boldsymbol{G}_u$, its contribution to the exponent only yields a unit factor. Moreover, due to symmetry of the Brillouin zone, the notation of $\boldsymbol{G}_u$ in the electron momentum is insignificant. The expression in eq. (B.2.3) is thus rewritten to

$$\sum_{i\in L} a_{iL}c^\dagger_{i\sigma}c_{i\tilde{\sigma}} = \frac{\sqrt{N_L}}{N} \sum_{\nu,\nu''} e^{i\boldsymbol{Q}_{\nu''}\cdot\boldsymbol{r}_L} \sum_{\boldsymbol{q},\boldsymbol{k}}^{\mathrm{mBZ}} a_{\boldsymbol{q}L}c^\dagger_{\boldsymbol{k}+\boldsymbol{q}+\boldsymbol{Q}_\nu+\boldsymbol{Q}_{\nu''},\sigma}c_{\boldsymbol{k}+\boldsymbol{Q}_\nu,\tilde{\sigma}}. \quad \text{(B.2.4)}$$

Now, both electron operators have the added momentum $\boldsymbol{Q}_\nu$. Thus, the sum over ν covers momenta across the entire eBZ. For brevity of notation, ν is absorbed by extending the sum over electron momenta to cover eBZ. Procedingly, rename the dummy index $\nu'' \to \nu$. The operator product thereby becomes

$$\sum_{i\in L} a_{iL}c^\dagger_{i\sigma}c_{i\tilde{\sigma}} = \frac{\sqrt{N_L}}{N} \sum_{\nu} e^{i\boldsymbol{Q}_\nu\cdot\boldsymbol{r}_L} \sum_{\boldsymbol{q}}^{\mathrm{mBZ}} \sum_{\boldsymbol{k}}^{\mathrm{eBZ}} a_{\boldsymbol{q}L}c^\dagger_{\boldsymbol{k}+\boldsymbol{q}+\boldsymbol{Q}_\nu,\sigma}c_{\boldsymbol{k}\tilde{\sigma}}. \quad \text{(B.2.5)}$$

The remaining operator product transforms accordingly, resulting

$$\sum_{i\in L} c^\dagger_{i\sigma}c_{i\tilde{\sigma}} = \frac{N_L}{N} \sum_{\nu} e^{i\boldsymbol{Q}_\nu\cdot\boldsymbol{r}_L} \sum_{\boldsymbol{k}}^{\mathrm{eBZ}} c^\dagger_{\boldsymbol{k}+\boldsymbol{Q}_\nu,\sigma}c_{\boldsymbol{k}\tilde{\sigma}}. \quad \text{(B.2.6)}$$

B.3 *Applying the Schrieffer-Wolff transformation

In this section, we apply the Schrieffer-Wolff transformation presented in section 2.2 to the system Hamiltonian in eq. (4.0.1). For completeness, we revisit this Hamiltonian in the following

$$\begin{aligned}\mathcal{H} =& \sum_{\boldsymbol{k},\sigma} \epsilon_{\boldsymbol{k}} c^\dagger_{\boldsymbol{k}\sigma} c_{\boldsymbol{k}\sigma} + \sum_{\boldsymbol{q},\gamma} \omega_{\boldsymbol{q}\gamma} b^\dagger_{\boldsymbol{q}\gamma} b_{\boldsymbol{q}\gamma} \\ &+ \sum_{\boldsymbol{q}}^{\mathrm{mBZ}} \sum_{\boldsymbol{k}}^{\mathrm{eBZ}} \sum_{\nu,\sigma,\tilde{\sigma}} \sum_{L,\gamma=1}^{m} \left[g_{L\nu\sigma\tilde{\sigma}} \left(u_{\boldsymbol{q}L\gamma} b_{\boldsymbol{q}\gamma} + v_{\boldsymbol{q}L\gamma} b^\dagger_{-\boldsymbol{q}\gamma} \right) c^\dagger_{\boldsymbol{k}+\boldsymbol{q}+\boldsymbol{Q}_\nu,\sigma} c_{\boldsymbol{k}\tilde{\sigma}} + \mathrm{h.c} \right],\end{aligned} \tag{4.0.1 revisited}$$

and identify the perturbation

$$\lambda\mathcal{H}_1 = \sum_{\boldsymbol{q},\boldsymbol{k}} \sum_{\nu,\sigma,\tilde{\sigma}} \sum_{L,\gamma=1}^{m} \left[g_{L\nu\sigma\tilde{\sigma}} \left(u_{\boldsymbol{q}L\gamma} b_{\boldsymbol{q}\gamma} + v_{\boldsymbol{q}L\gamma} b^\dagger_{-\boldsymbol{q}\gamma} \right) c^\dagger_{\boldsymbol{k}+\boldsymbol{q}+\boldsymbol{Q}_\nu,\sigma} c_{\boldsymbol{k}\tilde{\sigma}} + \mathrm{h.c} \right]. \tag{B.3.1}$$

Before proceeding to obtain the pair interaction Hamiltonian $\mathcal{H}_{\mathrm{pair}}$, we must first obtain the generator $\lambda\xi$. We do this in accordance with the termwise relation $\xi \sim \mathcal{H}_1$ from eq. (2.5.3). For this reason, study first the perturbation in eq. (B.3.1). Recall that the operator products embedded in the hermitian conjugate terms may be written to the same form as those explicitly present in eq. (B.3.1), as stated in section 3.3. This leaves two operator product forms of $\mathcal{H}_1$. Therefore, only two coefficients are needed to define ξ termwise in terms of $\mathcal{H}_1$; let

$$b_{\boldsymbol{q}\gamma} c^\dagger_{\boldsymbol{k}+\boldsymbol{q}+\boldsymbol{Q}_\nu,\sigma} c_{\boldsymbol{k}\tilde{\sigma}} \quad \rightarrow \quad \mathcal{X}_{\boldsymbol{k}\boldsymbol{q}\gamma\sigma\tilde{\sigma}} b_{\boldsymbol{q}\gamma} c^\dagger_{\boldsymbol{k}+\boldsymbol{q}+\boldsymbol{Q}_\nu,\sigma} c_{\boldsymbol{k}\tilde{\sigma}}, \tag{B.3.2}$$

$$b^\dagger_{-\boldsymbol{q}\gamma} c^\dagger_{\boldsymbol{k}+\boldsymbol{q}+\boldsymbol{Q}_\nu,\sigma} c_{\boldsymbol{k}\tilde{\sigma}} \quad \rightarrow \quad \mathcal{Y}_{\boldsymbol{k}\boldsymbol{q}\gamma\sigma\tilde{\sigma}} b^\dagger_{-\boldsymbol{q}\gamma} c^\dagger_{\boldsymbol{k}+\boldsymbol{q}+\boldsymbol{Q}_\nu,\sigma} c_{\boldsymbol{k}\tilde{\sigma}}, \tag{B.3.3}$$

to make the following ansatz

$$\lambda\xi^{(L)} = \sum_{\boldsymbol{q},\boldsymbol{k}} \sum_{\nu,\sigma,\tilde{\sigma}} \sum_{\gamma=1}^{m} \left[g_{L\nu\sigma\tilde{\sigma}} \left(\mathcal{X}_{\boldsymbol{k}\boldsymbol{q}\gamma\sigma\tilde{\sigma}} u_{\boldsymbol{q}L\gamma} b_{\boldsymbol{q}\gamma} + \mathcal{Y}_{\boldsymbol{k}\boldsymbol{q}\gamma\sigma\tilde{\sigma}} v_{\boldsymbol{q}L\gamma} b^\dagger_{-\boldsymbol{q}\gamma} \right) c^\dagger_{\boldsymbol{k}+\boldsymbol{q}+\boldsymbol{Q}_\nu,\sigma} c_{\boldsymbol{k}\tilde{\sigma}} + \mathrm{h.c} \right], \tag{B.3.4}$$

for which the coefficients $\mathcal{X}_{\boldsymbol{k}\boldsymbol{q}\gamma\sigma\tilde{\sigma}}$ and $\mathcal{Y}_{\boldsymbol{k}\boldsymbol{q}\gamma\sigma\tilde{\sigma}}$ are determined by the requirement $\mathcal{H}_1 = [\xi, \mathcal{H}_0]$ in eq. (2.5.5). In more detail, consider $\langle n| \mathcal{H}_1 |m\rangle$ for $|n\rangle$ and $|m\rangle$ eigenstates of $\mathcal{H}_0$ representing electron states dependent on the γ-mode magnon state. Let one these basis vectors be defined as

$$|n\rangle = \left| n_{\boldsymbol{k}\sigma},\ n_{\boldsymbol{k}+\boldsymbol{q}+\boldsymbol{Q}_\nu,\tilde{\sigma}},\ \eta_{\boldsymbol{q}\gamma} \right\rangle \tag{B.3.5a}$$

$$\equiv |n_{\boldsymbol{k}\sigma}\rangle \otimes \left| n_{\boldsymbol{k}+\boldsymbol{q}+\boldsymbol{Q}_\nu,\tilde{\sigma}} \right\rangle \otimes |\eta_{\boldsymbol{q}\gamma}\rangle, \tag{B.3.5b}$$

where the two first states in the product are electron states, while the remaining is a magnon state. Note that the presence of the second electron state is essential for $\mathcal{H}_1$ and ξ due to the electron scattering whose momentum is not conserved.

Moreover, each state in the product of eq. (B.3.5b) takes values 1 or 0 due to the low temperature region. To indicate electron spin, the finite electron states are denoted $|n_{\boldsymbol{k}\sigma}\rangle \equiv |\sigma\rangle$. To indicate magnon band, a finite magnon state is denoted $|\eta_{\pm\boldsymbol{q}\gamma}\rangle \equiv |\pm\gamma\rangle$. The eigenstates $|n\rangle$ in eq. (B.3.5) are defined such that

$$\mathcal{H}_0 |n\rangle = E_{0,n} |n\rangle , \tag{B.3.6}$$

$$\mathcal{H}_0 \begin{cases} |\sigma,0,0\rangle \\ |0,\tilde{\sigma},0\rangle \\ |0,0,\gamma\rangle \end{cases} = \begin{cases} \epsilon_{\boldsymbol{k}} |\sigma,0,0\rangle \\ \epsilon_{\boldsymbol{k}+\boldsymbol{q}+\boldsymbol{Q}_\nu} |0,\tilde{\sigma},0\rangle \\ \omega_{\boldsymbol{q}\gamma} |0,0,\gamma\rangle \end{cases} . \tag{B.3.7}$$

Note thus that the electron spin quantum number does not impact the electron dispersion. Continue to write the expectation value of $\mathcal{H}_1$ as follows

$$\langle m| \mathcal{H}_1 |n\rangle = \langle m| [\xi, \mathcal{H}_0] |n\rangle \tag{B.3.8a}$$

$$= (E_{0,n} - E_{0,m}) \langle m| \xi |n\rangle . \tag{B.3.8b}$$

We insert the ansatz of ξ in eq. (B.3.4) to obtain the coefficients $\mathcal{X}_{\boldsymbol{k}\boldsymbol{q}\gamma\sigma\tilde{\sigma}}$ and $\mathcal{Y}_{\boldsymbol{k}\boldsymbol{q}\gamma\sigma\tilde{\sigma}}$ by the appropriate choice of states $|m\rangle$ and $|n\rangle$. For example, we get

$$\mathcal{X}_{\boldsymbol{k}\boldsymbol{q}\gamma\sigma\tilde{\sigma}} = \frac{1}{E_{0,n_\mathcal{X}} - E_{0,m_\mathcal{X}}}, \tag{B.3.9}$$

for states $|n_\mathcal{X}\rangle$ and $|m_\mathcal{X}\rangle$ such that the term with coefficient $\mathcal{X}_{\boldsymbol{k}\boldsymbol{q}\gamma\sigma\tilde{\sigma}}$ survives the expectation value. A similar approach gives the coefficient $\mathcal{Y}_{\boldsymbol{k}\boldsymbol{q}\gamma\sigma\tilde{\sigma}}$. Inspect eq. (B.3.4) to note that only the magnon operator varies with the coefficients, while the electron operators remain. Therefore, we choose

$$|n\rangle = |\sigma, 0, \eta_{\boldsymbol{q}\gamma,n}\rangle \tag{B.3.10a}$$

$$|m\rangle = |0, \tilde{\sigma}, \eta_{\boldsymbol{q}\gamma,m}\rangle \tag{B.3.10b}$$

for which $\eta_{\boldsymbol{q}\gamma,n} \in \{\gamma, 0\}$ and $\eta_{\boldsymbol{q}\gamma,m} \in \{0, -\gamma\}$ to obtain $\mathcal{X}_{\boldsymbol{k}\boldsymbol{q}\gamma\sigma\tilde{\sigma}}$ and $\mathcal{Y}_{\boldsymbol{k}\boldsymbol{q}\gamma\sigma\tilde{\sigma}}$, respectively. To ensure clarity and ease comprehension, we present the following overview

$$\mathcal{X}_{\boldsymbol{k}\boldsymbol{q}\gamma\sigma\tilde{\sigma}} \quad \text{from} \quad \begin{cases} |n_\mathcal{X}\rangle = |\sigma,0,\gamma\rangle & \text{giving} \quad E_{0,n_\mathcal{X}} = \epsilon_{\boldsymbol{k}} + \omega_{\boldsymbol{q}\gamma} \\ |m_\mathcal{X}\rangle = |0,\tilde{\sigma},0\rangle & \text{giving} \quad E_{0,m_\mathcal{X}} = \epsilon_{\boldsymbol{k}+\boldsymbol{q}+\boldsymbol{Q}_\nu} \end{cases} \tag{B.3.11}$$

$$\mathcal{Y}_{\boldsymbol{k}\boldsymbol{q}\gamma\sigma\tilde{\sigma}} \quad \text{from} \quad \begin{cases} |n_\mathcal{Y}\rangle = |\sigma,0,0\rangle & \text{giving} \quad E_{0,n_\mathcal{Y}} = \epsilon_{\boldsymbol{k}} \\ |m_\mathcal{Y}\rangle = |0,\tilde{\sigma},-\gamma\rangle & \text{giving} \quad E_{0,m_\mathcal{Y}} = \epsilon_{\boldsymbol{k}+\boldsymbol{q}+\boldsymbol{Q}_\nu} + \omega_{-\boldsymbol{q}\gamma} \end{cases} \tag{B.3.12}$$

of how to obtain the two coefficients of ξ. Note however that the magnon dispersion is momentum inversion symmetric, as concluded previously in eq. (3.2.26). Inserting the states for each coefficient in eq. (B.3.11) into eq. (B.3.9), we thereby get the real coefficients

$$\mathcal{X}_{\boldsymbol{k}\boldsymbol{q}\gamma\sigma\tilde{\sigma}} = \frac{1}{\epsilon_{\boldsymbol{k}} - \epsilon_{\boldsymbol{k}+\boldsymbol{q}+\boldsymbol{Q}_\nu} + \omega_{\boldsymbol{q}\gamma}}, \tag{B.3.13a}$$

$$\mathcal{Y}_{\boldsymbol{k}\boldsymbol{q}\gamma\sigma\tilde{\sigma}} = \frac{1}{\epsilon_{\boldsymbol{k}} - \epsilon_{\boldsymbol{k}+\boldsymbol{q}+\boldsymbol{Q}_\nu} - \omega_{\boldsymbol{q}\gamma}}, \tag{B.3.13b}$$

independent of $\sigma, \tilde{\sigma}$. Therefore, discard these indices of the coefficients above.

At last, we may solve the commutator of $\mathcal{H}_{\text{pair}}$

$$\mathcal{H}_{\text{pair}} = -\frac{1}{2} \sum_{L,L'} \left[\lambda\xi^{(L)},\ \lambda\mathcal{H}_1^{(L')} \right], \tag{B.3.14}$$

where all summation indices in $\mathcal{H}_1^{(L')}$ are primed and may differ from those in $\xi^{(L)}$.

For the purpose of deriving the commutator in eq. (B.3.14), we first write out the hermitian conjugate terms of $\lambda\mathcal{H}_1^{(L)}$ and $\lambda\xi^{(L)}$ to prove that the embedded operator terms may be written as those explicitly written. This is done explicitly for $\lambda\mathcal{H}_1^{(L)}$ in eq. (B.3.1), before extending the calculations to apply for $\lambda\xi^{(L)}$.

By writing out the hermitian conjugate term of $\lambda\mathcal{H}_1$ in eq. (B.3.1), we are left with four particle operator products of the form

$$\left(A b_{\boldsymbol{q}\gamma} + b^\dagger_{-\boldsymbol{q}\gamma} \right) c^\dagger_{\boldsymbol{k}+\boldsymbol{q}+\boldsymbol{Q}_\nu,\sigma} c_{\boldsymbol{k}\tilde{\sigma}} + \left(b_{-\boldsymbol{q}\gamma} + A^\dagger b^\dagger_{\boldsymbol{q}\gamma} \right) c^\dagger_{\boldsymbol{k}\tilde{\sigma}} c_{\boldsymbol{k}+\boldsymbol{q}+\boldsymbol{Q}_\nu,\sigma} \tag{B.3.15}$$

for some A. The latter fermion product may then be written in the form of the former by renaming dummy indices. This procedure is shown in the following

$$(1) \quad \sigma \leftrightarrow \tilde{\sigma}; \qquad \left(b_{-\boldsymbol{q}\gamma} + A^\dagger b^\dagger_{\boldsymbol{q}\gamma} \right) c^\dagger_{\boldsymbol{k}\sigma} c_{\boldsymbol{k}+\boldsymbol{q}+\boldsymbol{Q}_\nu,\tilde{\sigma}} \tag{B.3.16a}$$

$$(2) \quad \boldsymbol{q} \to -\boldsymbol{q}; \qquad \left(b_{\boldsymbol{q}\gamma} + A^\dagger b^\dagger_{-\boldsymbol{q}\gamma} \right) c^\dagger_{\boldsymbol{k}\sigma} c_{\boldsymbol{k}-\boldsymbol{q}+\boldsymbol{Q}_\nu,\tilde{\sigma}} \tag{B.3.16b}$$

$$(3) \quad \boldsymbol{k} \to \boldsymbol{k}+\boldsymbol{q}-\boldsymbol{Q}_\nu; \qquad \left(b_{\boldsymbol{q}\gamma} + A^\dagger b^\dagger_{-\boldsymbol{q}\gamma} \right) c^\dagger_{\boldsymbol{k}+\boldsymbol{q}-\boldsymbol{Q}_\nu,\sigma} c_{\boldsymbol{k}\tilde{\sigma}} \tag{B.3.16c}$$

$$(4) \quad \boldsymbol{Q}_\nu \to -\boldsymbol{Q}_\nu; \qquad \left(b_{\boldsymbol{q}\gamma} + A^\dagger b^\dagger_{-\boldsymbol{q}\gamma} \right) c^\dagger_{\boldsymbol{k}+\boldsymbol{q}+\boldsymbol{Q}_\nu,\sigma} c_{\boldsymbol{k}\tilde{\sigma}}, \tag{B.3.16d}$$

in which the last step (4) is validated by that we may always write $\boldsymbol{Q}_\nu = -\boldsymbol{Q}_\nu + \boldsymbol{G}_u$ for some some electron reciprocal lattice vector $\boldsymbol{G}_u$ whose notation is insignificant due to the symmetry of the Brillouin zone, as previously argued.

Thus, eq. (B.3.1) may be written as a sum over two operator products, as in the following

$$\lambda\mathcal{H}_1^{(L)} = \sum_{\boldsymbol{q},\boldsymbol{k}} \sum_{\nu,\sigma,\tilde{\sigma},\gamma} \left(G_{\boldsymbol{q}L\gamma\nu\sigma\tilde{\sigma}} b_{\boldsymbol{q}\gamma} + G^*_{-\boldsymbol{q}L\gamma\nu\tilde{\sigma}\sigma} b^\dagger_{-\boldsymbol{q}\gamma} \right) c^\dagger_{\boldsymbol{k}+\boldsymbol{q}+\boldsymbol{Q}_\nu,\sigma} c_{\boldsymbol{k}\tilde{\sigma}}, \tag{B.3.17}$$

in which the new coefficients

$$G_{\boldsymbol{q}L\gamma\nu\sigma\tilde{\sigma}} = g_{L\nu\sigma\tilde{\sigma}} u_{\boldsymbol{q}L\gamma} + g_{L\nu\tilde{\sigma}\sigma} v^*_{-\boldsymbol{q}L\gamma} \tag{B.3.18}$$

were defined. Accordingly, $\lambda\xi$ in eq. (B.3.4) extends to

$$\lambda\xi^{(L)} = \sum_{\boldsymbol{q},\boldsymbol{k}} \sum_{\nu,\sigma,\tilde{\sigma},\gamma} \left(\mathcal{X}_{\boldsymbol{k}\boldsymbol{q}\gamma} G_{\boldsymbol{q}L\gamma\nu\sigma\tilde{\sigma}} b_{\boldsymbol{q}\gamma} + \mathcal{Y}_{\boldsymbol{k}\boldsymbol{q}\gamma} G^*_{-\boldsymbol{q}L\gamma\nu\tilde{\sigma}\sigma} b^\dagger_{-\boldsymbol{q}\gamma} \right) c^\dagger_{\boldsymbol{k}+\boldsymbol{q}+\boldsymbol{Q}_\nu,\sigma} c_{\boldsymbol{k}\tilde{\sigma}}. \tag{B.3.19}$$

Thus, the eqs. (B.3.17) and (B.3.19) may be inserted into the commutator $[\xi^{(L)}, \mathcal{H}_1^{(L')}]$ appearing in eq. (B.3.14) to eventually solve for the electron pair interaction. After some algebra, we get

$$\mathcal{H}_{\text{pair}} = -\frac{1}{2} \sum_{\boldsymbol{q},\boldsymbol{k},\nu,\sigma,\tilde{\sigma}} \sum_{\boldsymbol{k}',\nu',\sigma',\tilde{\sigma}'} V^{\sigma\tilde{\sigma}\sigma'\tilde{\sigma}'}_{\boldsymbol{k}\boldsymbol{q}\nu\nu'} c^{\dagger}_{\boldsymbol{k}+\boldsymbol{q}+\boldsymbol{Q}_\nu,\sigma} c_{\boldsymbol{k}\tilde{\sigma}} c^{\dagger}_{\boldsymbol{k}'-\boldsymbol{q}+\boldsymbol{Q}_{\nu'},\sigma'} c_{\boldsymbol{k}'\tilde{\sigma}'}, \tag{B.3.20}$$

in which we disregarded bilinear fermion operator terms for the purpose of deriving the effective electron-electron interaction. With the purpose to ease readability, we redefine the spins as they appear in eq. (B.3.20) to $\sigma_i,\ i = 1, 2, 3, 4$. The effective interaction Hamiltonian is thus rewritten to the following

$$\mathcal{H}_{\text{pair}} = \sum_{\boldsymbol{q},\boldsymbol{k},\nu} \sum_{\boldsymbol{k}',\nu'} \sum_{\{\sigma_i\}} V^{\sigma_1\sigma_2\sigma_3\sigma_4}_{\boldsymbol{k}\boldsymbol{q}\nu\nu'} c^{\dagger}_{\boldsymbol{k}+\boldsymbol{q}+\boldsymbol{Q}_\nu,\sigma_1} c_{\boldsymbol{k}\sigma_2} c^{\dagger}_{\boldsymbol{k}'-\boldsymbol{q}+\boldsymbol{Q}_{\nu'},\sigma_3} c_{\boldsymbol{k}'\sigma_4}, \tag{B.3.21}$$

such that the effective interaction potential $V^{\sigma_1\sigma_2\sigma_3\sigma_4}_{\boldsymbol{k}\boldsymbol{q}\nu\nu'}$ in is defined as follows

$$V^{\sigma_1\sigma_2\sigma_3\sigma_4}_{\boldsymbol{k}\boldsymbol{q}\nu\nu'} = -\frac{1}{2} \sum_{\gamma} \left[\frac{A^{\sigma_1\sigma_2\sigma_3\sigma_4}_{\boldsymbol{q}\gamma\nu\nu'}}{\epsilon_{\boldsymbol{k}} - \epsilon_{\boldsymbol{k}+\boldsymbol{q}+\boldsymbol{Q}_\nu} + \omega_{\boldsymbol{q}\gamma}} - \frac{A^{\sigma_3\sigma_4\sigma_1\sigma_2}_{-\boldsymbol{q}\gamma\nu'\nu}}{\epsilon_{\boldsymbol{k}} - \epsilon_{\boldsymbol{k}+\boldsymbol{q}+\boldsymbol{Q}_\nu} - \omega_{\boldsymbol{q}\gamma}} \right]. \tag{B.3.22}$$

in which we defined the new coefficients

$$A^{\sigma_1\sigma_2\sigma_3\sigma_4}_{\boldsymbol{q}\gamma\nu\nu'} = \sum_{L,L'} G_{\boldsymbol{q}L\gamma\nu\sigma_1\sigma_2} G^{*}_{\boldsymbol{q}L'\gamma\bar{\nu}'\sigma_4\sigma_3} \tag{B.3.23a}$$

$$\begin{aligned} &= \sum_{L,L'} \Big(g_{L\nu\sigma_1\sigma_2} g_{L'\nu'\sigma_3\sigma_4} u_{\boldsymbol{q}L\gamma} v_{-\boldsymbol{q}L'\gamma} + g_{L\nu\sigma_1\sigma_2} g^{*}_{L'\bar{\nu}'\sigma_4\sigma_3} u_{\boldsymbol{q}L\gamma} u^{*}_{\boldsymbol{q}L'\gamma} \\ &\qquad + g^{*}_{L\bar{\nu}\sigma_2\sigma_1} g_{L'\nu'\sigma_3\sigma_4} v^{*}_{-\boldsymbol{q}L\gamma} v_{-\boldsymbol{q}L'\gamma} + g^{*}_{L\bar{\nu}\sigma_2\sigma_1} g^{*}_{L'\bar{\nu}'\sigma_4\sigma_3} v^{*}_{-\boldsymbol{q}L\gamma} u^{*}_{\boldsymbol{q}L'\gamma} \Big), \end{aligned} \tag{B.3.23b}$$

inserted for $G_{\boldsymbol{q}L\gamma\nu\sigma_1\sigma_2}$ as defined in eq. (B.3.18).

C Implementing the model simplifications

C.1 Effective electron-electron interaction potential: plots with distinguished lines

In this section we provide the plots in figs. 5.6 and 5.7 though with all lines distinguished.

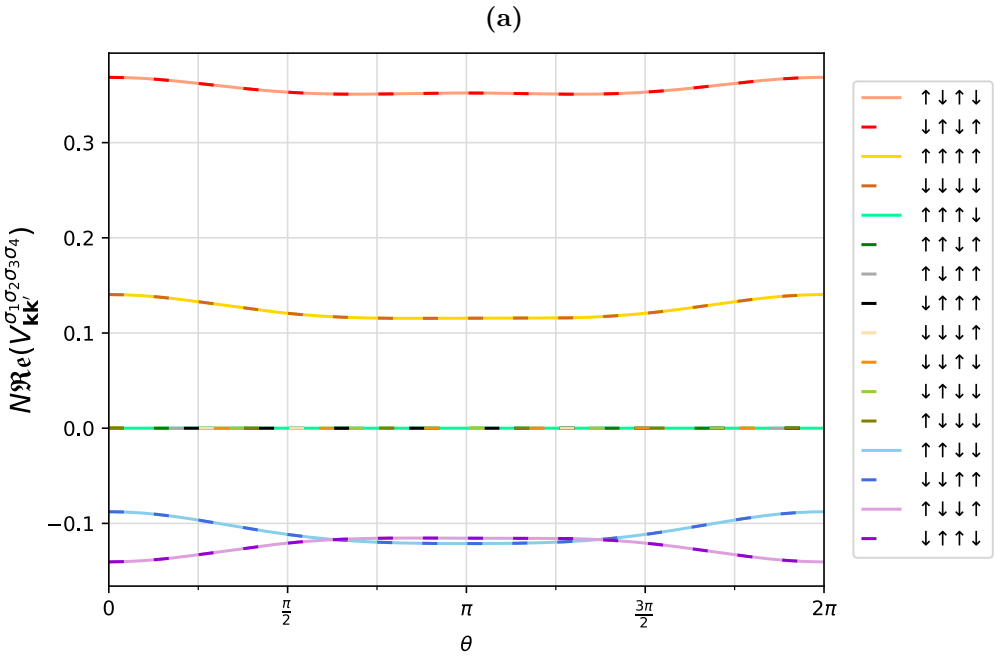

Figure C.1: Corresponds to the plot in fig. 5.6 for $\mu/t = -5.9$. Here, all lines are distinguished by various colours and styles. Figure (a) shows the real parts of the effective interaction potentials, while (b) shows the imaginary parts.
(Continued on next page)

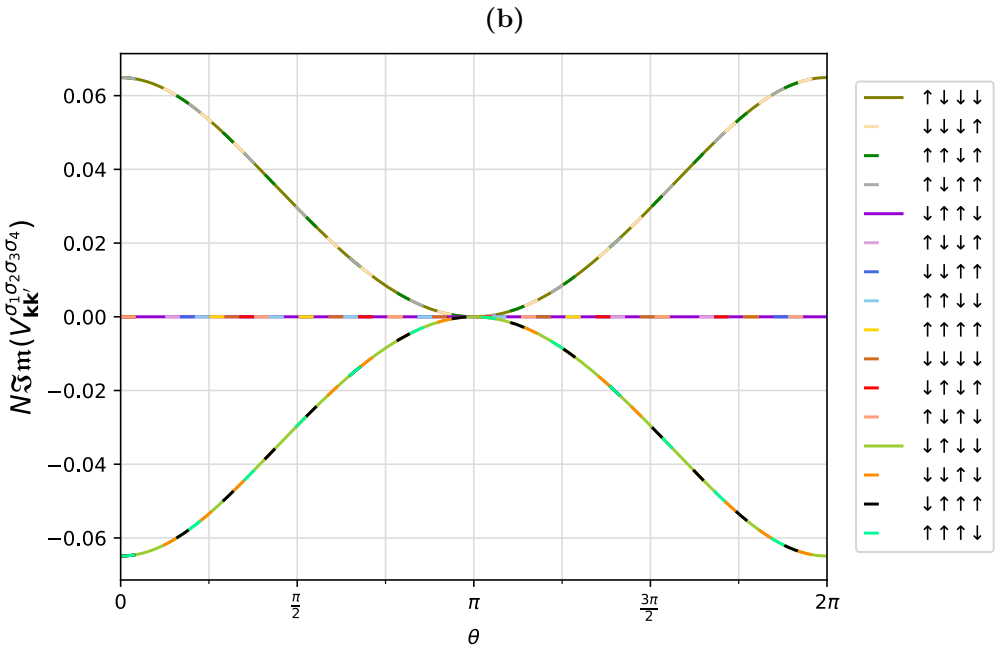

Figure C.1: Corresponds to the plot in fig. 5.6 for $\mu/t = -5.9$. Here, all lines are distinguished by various colours and styles. Figure (a) shows the real parts of the effective interaction potentials, while (b) shows the imaginary parts.

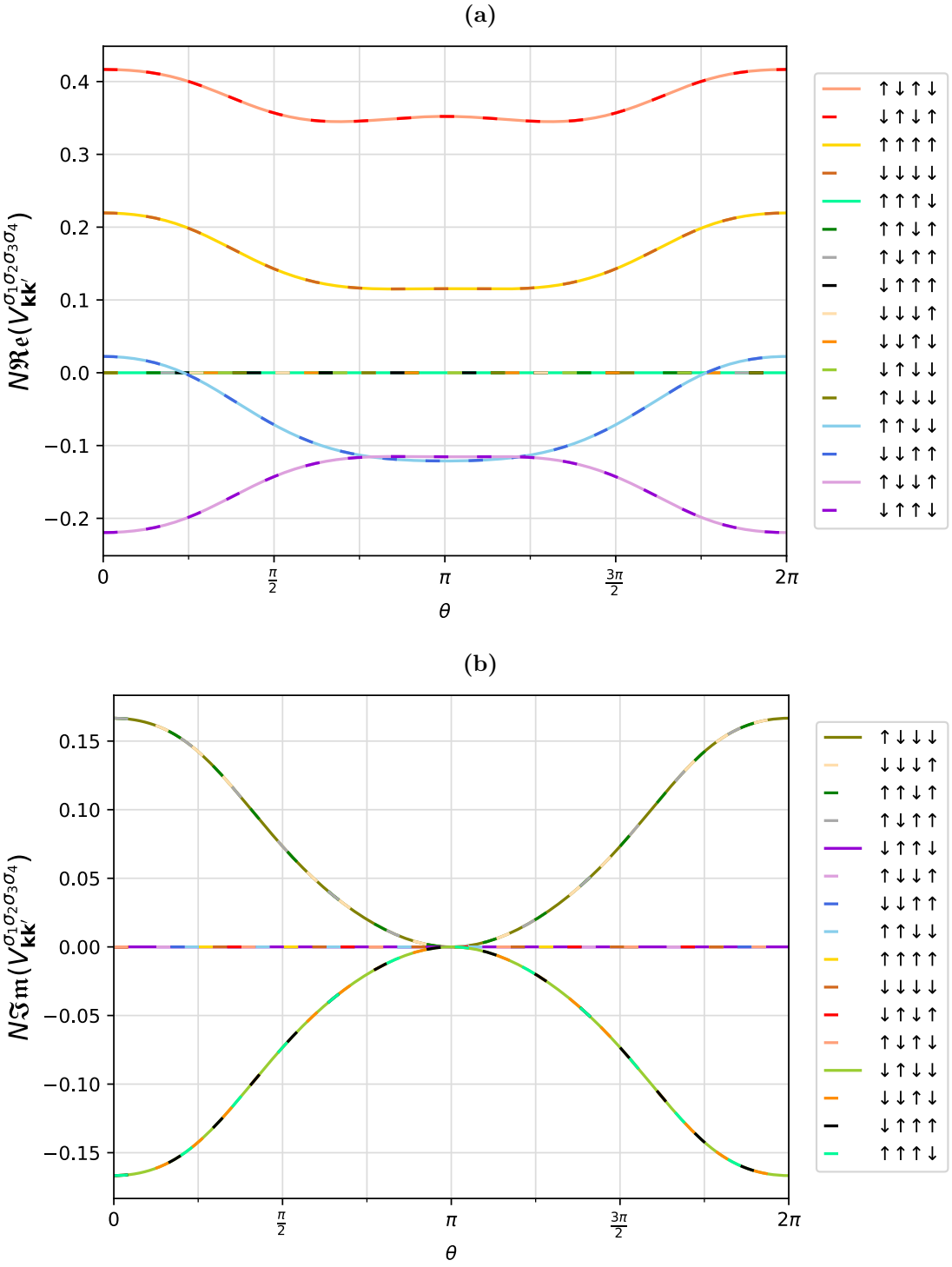

Figure C.2: Corresponds to the plot in fig. 5.7 for $\mu/t = -5.43$. Here, all lines are distinguished by various colours and styles. Figure (a) shows the real parts of the effective interaction potentials, while (b) shows the imaginary parts.

C.2 Barred effective electron-electron interaction potential: plots with distinguished line

In this section we provide the plots in figs. 5.8 and 5.9 though with all lines distinguished.

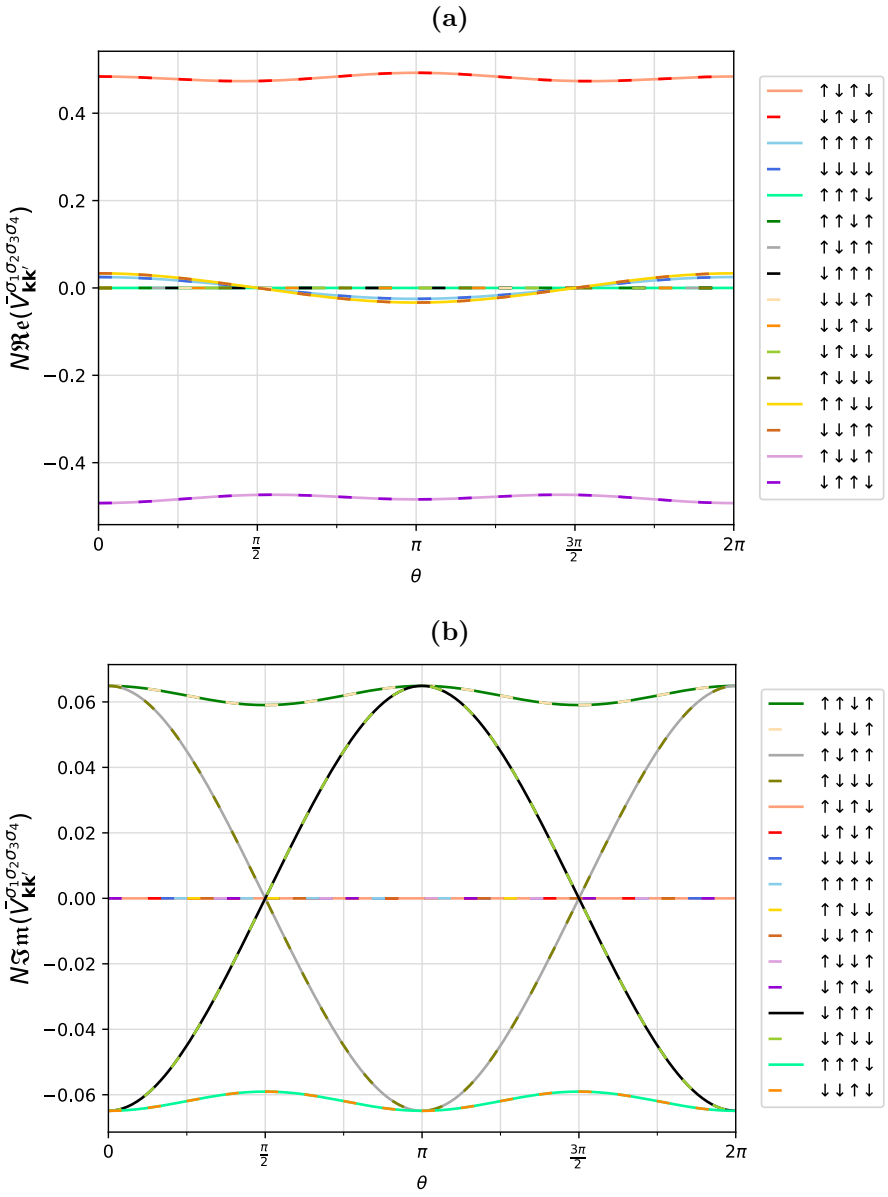

Figure C.3: Corresponds to the plot in fig. 5.8 for $\mu/t = -5.9$. Here, all lines are distinguished by various colours and styles. Figure (a) shows the real parts of the barred effective interaction potentials, while (b) shows the imaginary parts.

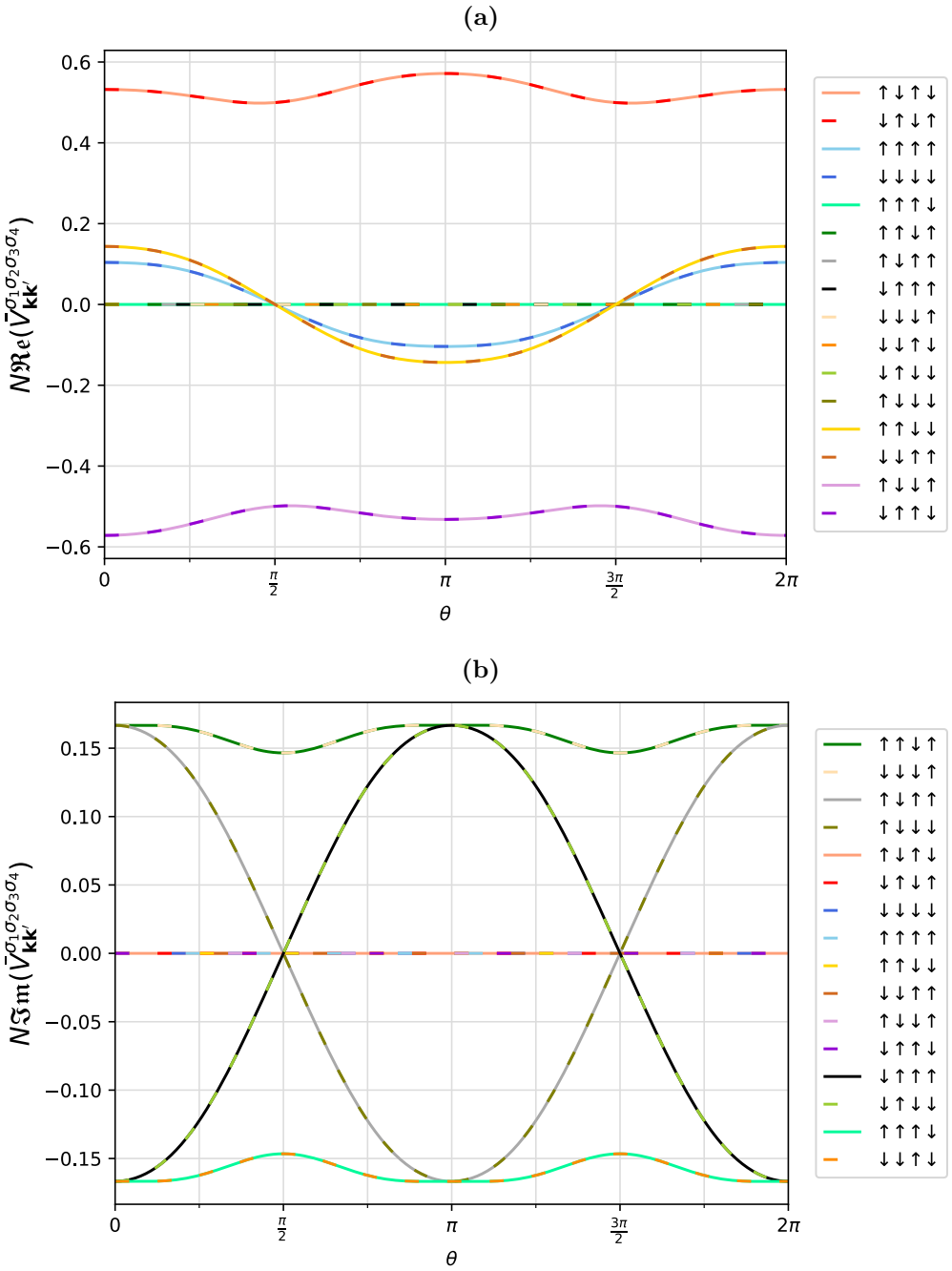

Figure C.4: Corresponds to the plot in fig. 5.9 for $\mu/t = -5.9$. Here, all lines are distinguished by various colours and styles. Figure (a) shows the real parts of the barred effective interaction potentials, while (b) shows the imaginary parts.

D Superconductivity

D.1 General derivation of the Helmholtz free energy

Consider a momentum-space Hamiltonian of N free fermions and its corresponding grand partition function

$$\mathcal{H} = \epsilon_0 + \sum_{\boldsymbol{k}} (\epsilon_{\boldsymbol{k}} - \mu)\, c^\dagger_{\boldsymbol{k}} c_{\boldsymbol{k}}, \tag{D.1.1}$$

$$Z = \sum_{\{n_{\boldsymbol{k}}\}} e^{-\beta \langle \mathcal{H}_{\boldsymbol{k}} \rangle}, \tag{D.1.2}$$

where μ is the chemical potential of the system; $\beta = {}^1\!/_{k_B T}$; and $\langle \mathcal{H}_{\boldsymbol{k}} \rangle = \epsilon_0 + \sum_{\boldsymbol{k}} (\epsilon_{\boldsymbol{k}} - \mu)\, n_{\boldsymbol{k}}$ is the average system energy. Thus, $n_{\boldsymbol{k}}$ is the number of particles occupying state $\boldsymbol{k}$, given by $n_{\boldsymbol{k}} \in \{0, 1\}$ from the Pauli principle [30, ch. 8]. Continue to rewrite the grand partition function by inserting for $\langle \mathcal{H}_{\boldsymbol{k}} \rangle$ and summing over the particle occupation number. After some algebra, we get

$$Z = e^{-\beta \epsilon_0} \prod_{\boldsymbol{k}} \left(1 + e^{-\beta(\epsilon_{\boldsymbol{k}} - \mu)}\right). \tag{D.1.3}$$

The corresponding free energy is then given by

$$F - \mu N = -\frac{1}{\beta} \ln Z, \tag{D.1.4a}$$

$$= \epsilon_0 - \frac{1}{\beta} \sum_{\boldsymbol{k}} \ln \left(1 + e^{-\beta(\epsilon_{\boldsymbol{k}} - \mu)}\right). \tag{D.1.4b}$$

D.2 Deriving the statistical averages

This section presents the full calculations of the minimised Helmholtz free energy, followed by the derivation of the statistical averages $b^\dagger_{\boldsymbol{k}\sigma_1\sigma_2}$.

The free energy of our system is given by

$$F = E_0 - \frac{1}{\beta} \sum_{\boldsymbol{k},\eta} \ln \left(1 + e^{-\beta E^\eta_{\boldsymbol{k}}}\right). \tag{6.2.2 revisited}$$

Its minimisation is given by $\frac{\partial F}{\partial \Delta_{\boldsymbol{k}\sigma_1\sigma_2}} = 0$, giving

$$\frac{\partial F}{\partial \Delta_{\boldsymbol{k}\sigma_1\sigma_2}} = \frac{\partial E_0}{\partial \Delta_{\boldsymbol{k}\sigma_1\sigma_2}} - \frac{1}{\beta}\sum_{\eta}\frac{\partial}{\partial \Delta_{\boldsymbol{k}\sigma_1\sigma_2}}\left[\ln\left(1+e^{-\beta E^{\eta}_{\boldsymbol{k}}}\right)\right]. \tag{D.2.1}$$

Consider each term of eq. (D.2.1). For the first term, insert E_0 as given by eq. (6.1.18) before differentiating

$$\frac{\partial E_0}{\partial \Delta_{\boldsymbol{k}\sigma_1\sigma_2}} = \frac{\partial}{\partial \Delta_{\boldsymbol{k}\sigma_1\sigma_2}}\left[\sum_{\boldsymbol{k}}\epsilon_{\boldsymbol{k}} + \frac{1}{2}\sum_{\boldsymbol{k},\sigma_1,\sigma_2}\Delta_{\boldsymbol{k}\sigma_1\sigma_2}b^{\dagger}_{\boldsymbol{k}\sigma_2\sigma_1} - \frac{1}{2}\sum_{\boldsymbol{k},\eta}E^{\eta}_{\boldsymbol{k}}\right], \tag{D.2.2a}$$

$$= \frac{1}{2}b^{\dagger}_{\boldsymbol{k}\sigma_2\sigma_1} - \frac{1}{2}\sum_{\eta}\frac{\partial E^{\eta}_{\boldsymbol{k}}}{\partial \Delta_{\boldsymbol{k}\sigma_1\sigma_2}}, \tag{D.2.2b}$$

since $\epsilon_{\boldsymbol{k}}$ is a constant of the gap functions.

The second term in eq. (D.2.1) becomes

$$\frac{\partial}{\partial \Delta_{\boldsymbol{k}\sigma_1\sigma_2}}\left[\ln\left(1+e^{-\beta E^{\eta}_{\boldsymbol{k}}}\right)\right] = \frac{1}{1+e^{-\beta E^{\eta}_{\boldsymbol{k}}}}\frac{\partial}{\partial \Delta_{\boldsymbol{k}\sigma_1\sigma_2}}\left[e^{-\beta E^{\eta}_{\boldsymbol{k}}}\right], \tag{D.2.3a}$$

$$= \frac{1}{1+e^{-\beta E^{\eta}_{\boldsymbol{k}}}}(-\beta)\,e^{-\beta E^{\eta}_{\boldsymbol{k}}}\frac{\partial E^{\eta}_{\boldsymbol{k}}}{\partial \Delta_{\boldsymbol{k}\sigma_1\sigma_2}}, \tag{D.2.3b}$$

$$= \frac{-\beta}{e^{\beta E^{\eta}_{\boldsymbol{k}}}+1}\frac{\partial E^{\eta}_{\boldsymbol{k}}}{\partial \Delta_{\boldsymbol{k}\sigma_1\sigma_2}}. \tag{D.2.3c}$$

Inserting the results of eqs. (D.2.2b) and (D.2.3c) into eq. (D.2.1) gives

$$0 = \frac{1}{2}b^{\dagger}_{\boldsymbol{k}\sigma_2\sigma_1} - \frac{1}{2}\sum_{\eta}\frac{\partial E^{\eta}_{\boldsymbol{k}}}{\partial \Delta_{\boldsymbol{k}\sigma_1\sigma_2}} - \frac{1}{\beta}\sum_{\eta}\frac{-\beta}{e^{\beta E^{\eta}_{\boldsymbol{k}}}+1}\frac{\partial E^{\eta}_{\boldsymbol{k}}}{\partial \Delta_{\boldsymbol{k}\sigma_1\sigma_2}}, \tag{D.2.4a}$$

$$= \frac{1}{2}b^{\dagger}_{\boldsymbol{k}\sigma_2\sigma_1} - \frac{1}{2}\sum_{\eta}\frac{\partial E^{\eta}_{\boldsymbol{k}}}{\partial \Delta_{\boldsymbol{k}\sigma_1\sigma_2}}\left(1 - 2\frac{1}{e^{\beta E^{\eta}_{\boldsymbol{k}}}+1}\right). \tag{D.2.4b}$$

Recognising the expression in the parentheses as $\tanh\left(\frac{x}{2}\right)$ for $x = \beta E^{\eta}_{\boldsymbol{k}}$, we may write the following expression for $b^{\dagger}_{\boldsymbol{k}\sigma_2\sigma_1}$

$$b^{\dagger}_{\boldsymbol{k}\sigma_2\sigma_1} = \sum_{\eta}\frac{\partial E^{\eta}_{\boldsymbol{k}}}{\partial \Delta_{\boldsymbol{k}\sigma_1\sigma_2}}\tanh\left(\frac{\beta E^{\eta}_{\boldsymbol{k}}}{2}\right). \tag{D.2.5}$$

Proceed to evaluate the remaining derivative in eq. (D.2.5) by inserting for $E^{\eta}_{\boldsymbol{k}}$ in eq. (6.1.14)

$$\frac{\partial E^{\eta}_{\boldsymbol{k}}}{\partial \Delta_{\boldsymbol{k}\sigma_1\sigma_2}} = \frac{\partial}{\partial \Delta_{\boldsymbol{k}\sigma_1\sigma_2}}\left[\sqrt{\epsilon^2_{\boldsymbol{k}} + \frac{1}{2}\sum_{\sigma,\sigma'}\left|\Delta_{\boldsymbol{k}\sigma\sigma'}\right|^2 + \frac{\eta}{2}\sqrt{A_{\boldsymbol{k}}}}\right], \tag{D.2.6a}$$

$$= \frac{1}{2E^{\eta}_{\boldsymbol{k}}}\left(\frac{1}{2}\Delta^{\dagger}_{\boldsymbol{k}\sigma_1\sigma_2} + \eta\frac{1}{4}\frac{1}{\sqrt{A_{\boldsymbol{k}}}}\frac{\partial A_{\boldsymbol{k}}}{\partial \Delta_{\boldsymbol{k}\sigma_1\sigma_2}}\right), \tag{D.2.6b}$$

$$\equiv \frac{1}{2E^{\eta}_{\boldsymbol{k}}}\left(\frac{1}{2}\Delta^{\dagger}_{\boldsymbol{k}\sigma_1\sigma_2} + \eta B^{\dagger}_{\boldsymbol{k}\sigma_1\sigma_2}\right), \tag{D.2.6c}$$

in which we defined

$$B^\dagger_{\boldsymbol{k}\sigma_1\sigma_2} \equiv \frac{1}{4}\frac{1}{\sqrt{A_{\boldsymbol{k}}}}\frac{\partial A_{\boldsymbol{k}}}{\partial \Delta_{\boldsymbol{k}\sigma_1\sigma_2}}, \tag{D.2.7}$$

Note that since $A_{\boldsymbol{k}} = A_{-\boldsymbol{k}}$, the $B_{\boldsymbol{k}\sigma_1\sigma_2}$ transforms as $\Delta_{\boldsymbol{k}\sigma_1\sigma_2}$ under inversion of $\boldsymbol{k}$.

Inserting into eq. (D.2.5), we write

$$b^\dagger_{\boldsymbol{k}\sigma_2\sigma_1} = \sum_\eta \left(\frac{1}{2}\Delta^\dagger_{\boldsymbol{k}\sigma_1\sigma_2} + \eta B^\dagger_{\boldsymbol{k}\sigma_1\sigma_2}\right)\frac{1}{2E^\eta_{\boldsymbol{k}}}\tanh\left(\frac{\beta E^\eta_{\boldsymbol{k}}}{2}\right), \tag{D.2.8a}$$

$$\equiv \sum_\eta \left(\frac{1}{2}\Delta^\dagger_{\boldsymbol{k}\sigma_1\sigma_2} + \eta B^\dagger_{\boldsymbol{k}\sigma_1\sigma_2}\right)\chi^\eta_{\boldsymbol{k}}, \tag{D.2.8b}$$

in which we defined the new variable

$$\chi^\eta_{\boldsymbol{k}} \equiv \frac{1}{2E^\eta_{\boldsymbol{k}}}\tanh\left(\frac{\beta E^\eta_{\boldsymbol{k}}}{2}\right). \tag{D.2.9}$$

D.3 Deriving the coupling matrix

This section presents the full derivation of the matrix of coupling functions appearing in the matrix formulation of the superconducting gap equation.

The gap equation of the system is given by

$$\Delta_{\boldsymbol{k}\sigma_1\sigma_2} = -\sum_{\boldsymbol{k}',\sigma_3,\sigma_4} \bar{V}^{\sigma_1\sigma_2\sigma_3\sigma_4}_{\boldsymbol{k}'\boldsymbol{k}} \sum_\eta \left(\frac{1}{2}\Delta_{\boldsymbol{k}'\sigma_4\sigma_3} + \eta B_{\boldsymbol{k}'\sigma_4\sigma_3}\right)\chi^\eta_{\boldsymbol{k}'}, \qquad \text{(6.2.4 revisited)}$$

which may be written as

$$|\Delta_{\boldsymbol{k}}\rangle \equiv -\sum_{\boldsymbol{k}'} \boldsymbol{\mathcal{V}}_{\boldsymbol{k}'\boldsymbol{k}} \sum_\eta \left(\frac{1}{2}|\Delta_{\boldsymbol{k}'}\rangle + \eta\,|B_{\boldsymbol{k}'}\rangle\right)\chi^\eta_{\boldsymbol{k}'}, \qquad \text{(6.2.7 revisited)}$$

on matrix form. We say that the coupling matrix $\boldsymbol{\mathcal{V}}_{\boldsymbol{k}'\boldsymbol{k}}$ contains elements $\boldsymbol{\mathcal{V}}_{\boldsymbol{k}'\boldsymbol{k}}[r,c]$ for some row and column $r, c \in \{1,2,3,4\}$.

For brevity of notation, define the parameter

$$\xi_{\boldsymbol{k}\sigma_1\sigma_2} \equiv \sum_\eta \left(\frac{1}{2}\Delta_{\boldsymbol{k}\sigma_1\sigma_2} + \eta B_{\boldsymbol{k}\sigma_1\sigma_2}\right)\chi^\eta_{\boldsymbol{k}}, \tag{D.3.1}$$

and the vector

$$|\xi_{\boldsymbol{k}}\rangle \equiv \left(\xi^{O(s)}_{\boldsymbol{k}\uparrow\downarrow},\ \xi_{\boldsymbol{k}\uparrow\uparrow},\ \xi_{\boldsymbol{k}\downarrow\downarrow},\ \xi^{E(s)}_{\boldsymbol{k}\uparrow\downarrow}\right)^T, \tag{D.3.2}$$

such that the elements

$$\xi^{O(s)}_{\boldsymbol{k}\uparrow\downarrow} \equiv \frac{\xi_{\boldsymbol{k}\uparrow\downarrow} - \xi_{\boldsymbol{k}\downarrow\uparrow}}{2}, \tag{D.3.3a}$$

$$\xi^{E(s)}_{\boldsymbol{k}\uparrow\downarrow} \equiv \frac{\xi_{\boldsymbol{k}\uparrow\downarrow} + \xi_{\boldsymbol{k}\downarrow\uparrow}}{2}, \tag{D.3.3b}$$

are odd and even in spin, respectively. Consequently, they are also even and odd in momentum, respectively.

Thereby, the gap equation in eq. (6.2.4 revisited) may be written

$$\xi_{\boldsymbol{k}\sigma_1\sigma_2} = -\sum_{\boldsymbol{k}',\sigma_3,\sigma_4} \bar{V}^{\sigma_1\sigma_2\sigma_3\sigma_4}_{\boldsymbol{k}'\boldsymbol{k}} \xi_{\boldsymbol{k}'\sigma_4\sigma_3}, \tag{D.3.4}$$

and on matrix form

$$|\xi_{\boldsymbol{k}}\rangle = -\sum_{\boldsymbol{k}'} \boldsymbol{\mathcal{V}}_{\boldsymbol{k}'\boldsymbol{k}} |\xi_{\boldsymbol{k}'}\rangle . \tag{D.3.5}$$

To obtain the elements of the coupling matrix $\boldsymbol{\mathcal{V}}_{\boldsymbol{k}'\boldsymbol{k}}$, we first write out the sum over spins in eq. (D.3.4). Omitting the sum over $\boldsymbol{k}'$ for brevity of notation, we get

$$\xi_{\boldsymbol{k}\sigma_1\sigma_2}(\boldsymbol{k}') = -\left(\bar{V}^{\sigma_1\sigma_2\uparrow\uparrow}_{\boldsymbol{k}'\boldsymbol{k}}\xi_{\boldsymbol{k}'\uparrow\uparrow} + \bar{V}^{\sigma_1\sigma_2\uparrow\downarrow}_{\boldsymbol{k}'\boldsymbol{k}}\xi_{\boldsymbol{k}'\downarrow\uparrow} + \bar{V}^{\sigma_1\sigma_2\downarrow\uparrow}_{\boldsymbol{k}'\boldsymbol{k}}\xi_{\boldsymbol{k}'\uparrow\downarrow} + \bar{V}^{\sigma_1\sigma_2\downarrow\downarrow}_{\boldsymbol{k}'\boldsymbol{k}}\xi_{\boldsymbol{k}'\downarrow\downarrow}\right). \tag{D.3.6}$$

Eventually, we want to write $|\xi_{\boldsymbol{k}}\rangle$ in terms of $|\xi_{\boldsymbol{k}'}\rangle$. Therefore insert for $\xi_{\boldsymbol{k}'\uparrow\downarrow}$ and $\xi_{\boldsymbol{k}'\downarrow\uparrow}$ in terms of $\xi^{O(s)}_{\boldsymbol{k}'\uparrow\downarrow}$ and $\xi^{E(s)}_{\boldsymbol{k}'\uparrow\downarrow}$ defined in eq. (D.3.3), i.e.,

$$\xi_{\boldsymbol{k}'\uparrow\downarrow} = \xi^{E(s)}_{\boldsymbol{k}'\uparrow\downarrow} + \xi^{O(s)}_{\boldsymbol{k}'\uparrow\downarrow}, \tag{D.3.7a}$$

$$\xi_{\boldsymbol{k}'\downarrow\uparrow} = \xi^{E(s)}_{\boldsymbol{k}'\uparrow\downarrow} - \xi^{O(s)}_{\boldsymbol{k}'\uparrow\downarrow}, \tag{D.3.7b}$$

into eq. (D.3.6). This gives

$$\begin{aligned}\xi_{\boldsymbol{k}\sigma_1\sigma_2}(\boldsymbol{k}') &= -\Big[\bar{V}^{\sigma_1\sigma_2\uparrow\uparrow}_{\boldsymbol{k}'\boldsymbol{k}}\xi_{\boldsymbol{k}'\uparrow\uparrow} + \bar{V}^{\sigma_1\sigma_2\uparrow\downarrow}_{\boldsymbol{k}'\boldsymbol{k}}\left(\xi^{E(s)}_{\boldsymbol{k}'\uparrow\downarrow} - \xi^{O(s)}_{\boldsymbol{k}'\uparrow\downarrow}\right) \\ &\qquad + \bar{V}^{\sigma_1\sigma_2\downarrow\uparrow}_{\boldsymbol{k}'\boldsymbol{k}}\left(\xi^{E(s)}_{\boldsymbol{k}'\uparrow\downarrow} + \xi^{O(s)}_{\boldsymbol{k}'\uparrow\downarrow}\right) + \bar{V}^{\sigma_1\sigma_2\downarrow\downarrow}_{\boldsymbol{k}'\boldsymbol{k}}\xi_{\boldsymbol{k}'\downarrow\downarrow}\Big]\end{aligned} \tag{D.3.8a}$$

$$\begin{aligned}&= -\Big[\left(\bar{V}^{\sigma_1\sigma_2\downarrow\uparrow}_{\boldsymbol{k}'\boldsymbol{k}} - \bar{V}^{\sigma_1\sigma_2\uparrow\downarrow}_{\boldsymbol{k}'\boldsymbol{k}}\right)\xi^{O(s)}_{\boldsymbol{k}'\uparrow\downarrow} + \bar{V}^{\sigma_1\sigma_2\uparrow\uparrow}_{\boldsymbol{k}'\boldsymbol{k}}\xi_{\boldsymbol{k}'\uparrow\uparrow} \\ &\qquad + \bar{V}^{\sigma_1\sigma_2\downarrow\downarrow}_{\boldsymbol{k}'\boldsymbol{k}}\xi_{\boldsymbol{k}'\downarrow\downarrow} + \left(\bar{V}^{\sigma_1\sigma_2\downarrow\uparrow}_{\boldsymbol{k}'\boldsymbol{k}} + \bar{V}^{\sigma_1\sigma_2\uparrow\downarrow}_{\boldsymbol{k}'\boldsymbol{k}}\right)\xi^{E(s)}_{\boldsymbol{k}'\uparrow\downarrow}\Big].\end{aligned} \tag{D.3.8b}$$

Consider now each component of $|\xi_{\boldsymbol{k}}\rangle$ as given in eqs. (D.3.2) and (D.3.3). The first element $\xi^{O(s)}_{\boldsymbol{k}\uparrow\downarrow}$ becomes

$$\begin{aligned}\xi^{O(s)}_{\boldsymbol{k}\uparrow\downarrow}(\boldsymbol{k}') = -\frac{1}{2}\Big[&\left(\bar{V}^{\uparrow\downarrow\downarrow\uparrow}_{\boldsymbol{k}'\boldsymbol{k}} - \bar{V}^{\uparrow\downarrow\uparrow\downarrow}_{\boldsymbol{k}'\boldsymbol{k}}\right)\xi^{O(s)}_{\boldsymbol{k}'\uparrow\downarrow} + \bar{V}^{\uparrow\downarrow\uparrow\uparrow}_{\boldsymbol{k}'\boldsymbol{k}}\xi_{\boldsymbol{k}'\uparrow\uparrow} \\ &+ \bar{V}^{\uparrow\downarrow\downarrow\downarrow}_{\boldsymbol{k}'\boldsymbol{k}}\xi_{\boldsymbol{k}'\downarrow\downarrow} + \left(\bar{V}^{\uparrow\downarrow\downarrow\uparrow}_{\boldsymbol{k}'\boldsymbol{k}} + \bar{V}^{\uparrow\downarrow\uparrow\downarrow}_{\boldsymbol{k}'\boldsymbol{k}}\right)\xi^{E(s)}_{\boldsymbol{k}'\uparrow\downarrow} \\ &- \left(\bar{V}^{\downarrow\uparrow\downarrow\uparrow}_{\boldsymbol{k}'\boldsymbol{k}} - \bar{V}^{\downarrow\uparrow\uparrow\downarrow}_{\boldsymbol{k}'\boldsymbol{k}}\right)\xi^{O(s)}_{\boldsymbol{k}'\uparrow\downarrow} - \bar{V}^{\downarrow\uparrow\uparrow\uparrow}_{\boldsymbol{k}'\boldsymbol{k}}\xi_{\boldsymbol{k}'\uparrow\uparrow} \\ &- \bar{V}^{\downarrow\uparrow\downarrow\downarrow}_{\boldsymbol{k}'\boldsymbol{k}}\xi_{\boldsymbol{k}'\downarrow\downarrow} - \left(\bar{V}^{\downarrow\uparrow\downarrow\uparrow}_{\boldsymbol{k}'\boldsymbol{k}} + \bar{V}^{\downarrow\uparrow\uparrow\downarrow}_{\boldsymbol{k}'\boldsymbol{k}}\right)\xi^{E(s)}_{\boldsymbol{k}'\uparrow\downarrow}\Big].\end{aligned} \tag{D.3.9}$$

Collecting the elements of $|\xi_{\boldsymbol{k}'}\rangle$, gives

$$\xi^{O(s)}_{\boldsymbol{k}\uparrow\downarrow}(\boldsymbol{k}') = -\frac{1}{2}\Big[\left(\bar{V}^{\uparrow\downarrow\downarrow\uparrow}_{\boldsymbol{k}'\boldsymbol{k}} - \bar{V}^{\uparrow\downarrow\uparrow\downarrow}_{\boldsymbol{k}'\boldsymbol{k}} - \bar{V}^{\downarrow\uparrow\downarrow\uparrow}_{\boldsymbol{k}'\boldsymbol{k}} + \bar{V}^{\downarrow\uparrow\uparrow\downarrow}_{\boldsymbol{k}'\boldsymbol{k}}\right) \xi^{O(s)}_{\boldsymbol{k}'\uparrow\downarrow} + \left(\bar{V}^{\uparrow\downarrow\uparrow\uparrow}_{\boldsymbol{k}'\boldsymbol{k}} - \bar{V}^{\downarrow\uparrow\uparrow\uparrow}_{\boldsymbol{k}'\boldsymbol{k}}\right) \xi_{\boldsymbol{k}'\uparrow\uparrow} + \left(\bar{V}^{\uparrow\downarrow\downarrow\downarrow}_{\boldsymbol{k}'\boldsymbol{k}} - \bar{V}^{\downarrow\uparrow\downarrow\downarrow}_{\boldsymbol{k}'\boldsymbol{k}}\right) \xi_{\boldsymbol{k}'\downarrow\downarrow} + \left(\bar{V}^{\uparrow\downarrow\downarrow\uparrow}_{\boldsymbol{k}'\boldsymbol{k}} + \bar{V}^{\uparrow\downarrow\uparrow\downarrow}_{\boldsymbol{k}'\boldsymbol{k}} - \bar{V}^{\downarrow\uparrow\downarrow\uparrow}_{\boldsymbol{k}'\boldsymbol{k}} - \bar{V}^{\downarrow\uparrow\uparrow\downarrow}_{\boldsymbol{k}'\boldsymbol{k}}\right) \xi^{E(s)}_{\boldsymbol{k}'\uparrow\downarrow}\Big]. \tag{D.3.10}$$

Before proceeding, define $\widetilde{V} \equiv 2\bar{V}^{\downarrow\uparrow\uparrow\downarrow}_{\boldsymbol{k}'\boldsymbol{k}}$ for brevity of notation. Thus, we may conclude the four elements of the first row of the coupling matrix. Using the symmetries of $\bar{V}^{\sigma_1\sigma_2\sigma_3\sigma_4}_{\boldsymbol{k}'\boldsymbol{k}}$ in eq. (5.3.7), we get

$$\boldsymbol{\mathcal{V}}_{\boldsymbol{k}'\boldsymbol{k}}[1,1] = \frac{1}{2}\left(\bar{V}^{\uparrow\downarrow\downarrow\uparrow}_{\boldsymbol{k}'\boldsymbol{k}} - \bar{V}^{\uparrow\downarrow\uparrow\downarrow}_{\boldsymbol{k}'\boldsymbol{k}} - \bar{V}^{\downarrow\uparrow\downarrow\uparrow}_{\boldsymbol{k}'\boldsymbol{k}} + \bar{V}^{\downarrow\uparrow\uparrow\downarrow}_{\boldsymbol{k}'\boldsymbol{k}}\right) \tag{D.3.11a}$$

$$= \frac{1}{4}\left(\widetilde{V}_{(-\boldsymbol{k}')(-\boldsymbol{k})} + \widetilde{V}_{\boldsymbol{k}'(-\boldsymbol{k})} + \widetilde{V}_{(-\boldsymbol{k}')\boldsymbol{k}} + \widetilde{V}_{\boldsymbol{k}'\boldsymbol{k}}\right) \tag{D.3.11b}$$

$$\equiv \widetilde{V}^{E(\boldsymbol{k}')E(\boldsymbol{k})}_{\boldsymbol{k}'\boldsymbol{k}}, \tag{D.3.11c}$$

$$\boldsymbol{\mathcal{V}}_{\boldsymbol{k}'\boldsymbol{k}}[1,2] = \frac{\bar{V}^{\uparrow\downarrow\uparrow\uparrow}_{\boldsymbol{k}'\boldsymbol{k}} - \bar{V}^{\downarrow\uparrow\uparrow\uparrow}_{\boldsymbol{k}'\boldsymbol{k}}}{2} = \frac{\bar{V}^{\uparrow\downarrow\uparrow\uparrow}_{\boldsymbol{k}'\boldsymbol{k}} + \bar{V}^{\uparrow\downarrow\uparrow\uparrow}_{\boldsymbol{k}'(-\boldsymbol{k})}}{2} \tag{D.3.12a}$$

$$\equiv \bar{V}^{\uparrow\downarrow\uparrow\uparrow E(\boldsymbol{k})}_{\boldsymbol{k}'\boldsymbol{k}}, \tag{D.3.12b}$$

$$\boldsymbol{\mathcal{V}}_{\boldsymbol{k}'\boldsymbol{k}}[1,3] = \frac{\bar{V}^{\uparrow\downarrow\downarrow\downarrow}_{\boldsymbol{k}'\boldsymbol{k}} - \bar{V}^{\downarrow\uparrow\downarrow\downarrow}_{\boldsymbol{k}'\boldsymbol{k}}}{2} = \frac{\bar{V}^{\uparrow\downarrow\downarrow\downarrow}_{\boldsymbol{k}'\boldsymbol{k}} + \bar{V}^{\uparrow\downarrow\downarrow\downarrow}_{\boldsymbol{k}'(-\boldsymbol{k})}}{2} \tag{D.3.13a}$$

$$\equiv \bar{V}^{\uparrow\downarrow\downarrow\downarrow E(\boldsymbol{k})}_{\boldsymbol{k}'\boldsymbol{k}}, \tag{D.3.13b}$$

$$\boldsymbol{\mathcal{V}}_{\boldsymbol{k}'\boldsymbol{k}}[1,4] = \frac{1}{2}\left(\bar{V}^{\uparrow\downarrow\downarrow\uparrow}_{\boldsymbol{k}'\boldsymbol{k}} + \bar{V}^{\uparrow\downarrow\uparrow\downarrow}_{\boldsymbol{k}'\boldsymbol{k}} - \bar{V}^{\downarrow\uparrow\downarrow\uparrow}_{\boldsymbol{k}'\boldsymbol{k}} - \bar{V}^{\downarrow\uparrow\uparrow\downarrow}_{\boldsymbol{k}'\boldsymbol{k}}\right) \tag{D.3.14a}$$

$$= \frac{1}{4}\left(\widetilde{V}_{(-\boldsymbol{k}')(-\boldsymbol{k})} - \widetilde{V}_{\boldsymbol{k}'(-\boldsymbol{k})} + \widetilde{V}_{(-\boldsymbol{k}')\boldsymbol{k}} - \widetilde{V}_{\boldsymbol{k}'\boldsymbol{k}}\right) \tag{D.3.14b}$$

$$\equiv \widetilde{V}^{O(\boldsymbol{k}')E(\boldsymbol{k})}_{\boldsymbol{k}'\boldsymbol{k}}, \tag{D.3.14c}$$

coupling functions of the gap parameters, even or odd in momenta $\boldsymbol{k}'$, $\boldsymbol{k}$.

Continue to apply this method to the remaining components of $|\xi_{\boldsymbol{k}}\rangle$. The second element $\xi_{\boldsymbol{k}\uparrow\uparrow}$ becomes

$$\xi_{\boldsymbol{k}\uparrow\uparrow}(\boldsymbol{k}') = -\Big[\left(\bar{V}^{\uparrow\uparrow\downarrow\uparrow}_{\boldsymbol{k}'\boldsymbol{k}} - \bar{V}^{\uparrow\uparrow\uparrow\downarrow}_{\boldsymbol{k}'\boldsymbol{k}}\right) \xi^{O(s)}_{\boldsymbol{k}'\uparrow\downarrow} + \bar{V}^{\uparrow\uparrow\uparrow\uparrow}_{\boldsymbol{k}'\boldsymbol{k}} \xi_{\boldsymbol{k}'\uparrow\uparrow} + \bar{V}^{\uparrow\uparrow\downarrow\downarrow}_{\boldsymbol{k}'\boldsymbol{k}} \xi_{\boldsymbol{k}'\downarrow\downarrow} + \left(\bar{V}^{\uparrow\uparrow\downarrow\uparrow}_{\boldsymbol{k}'\boldsymbol{k}} + \bar{V}^{\uparrow\uparrow\uparrow\downarrow}_{\boldsymbol{k}'\boldsymbol{k}}\right) \xi^{E(s)}_{\boldsymbol{k}'\uparrow\downarrow}\Big], \tag{D.3.15}$$

by inserting for $(\sigma_1\sigma_2) = (\uparrow\uparrow)$ into eq. (D.3.8b). The four elements of the second row of the coupling matrix are thereby

$$\boldsymbol{\mathcal{V}}_{\boldsymbol{k}'\boldsymbol{k}}[2,1] = \bar{V}^{\uparrow\uparrow\downarrow\uparrow}_{\boldsymbol{k}'\boldsymbol{k}} - \bar{V}^{\uparrow\uparrow\uparrow\downarrow}_{\boldsymbol{k}'\boldsymbol{k}} = -\bar{V}^{\uparrow\uparrow\uparrow\downarrow}_{(-\boldsymbol{k}')\boldsymbol{k}} - \bar{V}^{\uparrow\uparrow\uparrow\downarrow}_{\boldsymbol{k}'\boldsymbol{k}} \tag{D.3.16a}$$

$$\equiv -2\bar{V}^{\uparrow\uparrow\uparrow\downarrow E(\boldsymbol{k}')}_{\boldsymbol{k}'\boldsymbol{k}}, \tag{D.3.16b}$$

$$\boldsymbol{\mathcal{V}}_{\boldsymbol{k}'\boldsymbol{k}}[2,2] = \bar{V}^{\uparrow\uparrow\uparrow\uparrow}_{\boldsymbol{k}'\boldsymbol{k}}, \tag{D.3.17}$$

$$\boldsymbol{\mathcal{V}}_{\boldsymbol{k}'\boldsymbol{k}}[2,3] = \bar{V}^{\uparrow\uparrow\downarrow\downarrow}_{\boldsymbol{k}'\boldsymbol{k}}, \tag{D.3.18}$$

$$\boldsymbol{\mathcal{V}}_{\boldsymbol{k}'\boldsymbol{k}}[2,4] = \bar{V}^{\uparrow\uparrow\downarrow\uparrow}_{\boldsymbol{k}'\boldsymbol{k}} + \bar{V}^{\uparrow\uparrow\uparrow\downarrow}_{\boldsymbol{k}'\boldsymbol{k}} = -\bar{V}^{\uparrow\uparrow\uparrow\downarrow}_{(-\boldsymbol{k}')\boldsymbol{k}} + \bar{V}^{\uparrow\uparrow\uparrow\downarrow}_{\boldsymbol{k}'\boldsymbol{k}} \tag{D.3.19a}$$

$$\equiv 2\bar{V}^{\uparrow\uparrow\uparrow\downarrow O(\boldsymbol{k}')}_{\boldsymbol{k}'\boldsymbol{k}}. \tag{D.3.19b}$$

Moreover, the third element of $|\xi_{\boldsymbol{k}}\rangle$, $\xi_{\boldsymbol{k}\downarrow\downarrow}$, becomes

$$\xi_{\boldsymbol{k}\downarrow\downarrow}(\boldsymbol{k}') = -\Big[\left(\bar{V}^{\downarrow\downarrow\downarrow\uparrow}_{\boldsymbol{k}'\boldsymbol{k}} - \bar{V}^{\downarrow\downarrow\uparrow\downarrow}_{\boldsymbol{k}'\boldsymbol{k}}\right)\xi^{O(s)}_{\boldsymbol{k}'\uparrow\downarrow} + \bar{V}^{\downarrow\downarrow\uparrow\uparrow}_{\boldsymbol{k}'\boldsymbol{k}}\xi_{\boldsymbol{k}'\uparrow\uparrow} + \bar{V}^{\downarrow\downarrow\downarrow\downarrow}_{\boldsymbol{k}'\boldsymbol{k}}\xi_{\boldsymbol{k}'\downarrow\downarrow} + \left(\bar{V}^{\downarrow\downarrow\downarrow\uparrow}_{\boldsymbol{k}'\boldsymbol{k}} + \bar{V}^{\downarrow\downarrow\uparrow\downarrow}_{\boldsymbol{k}'\boldsymbol{k}}\right)\xi^{E(s)}_{\boldsymbol{k}'\uparrow\downarrow}\Big], \tag{D.3.20}$$

by inserting for $(\sigma_1\sigma_2) = (\downarrow\downarrow)$ into eq. (D.3.8b). Thus, the four elements of the third row of the coupling matrix become

$$\boldsymbol{\mathcal{V}}_{\boldsymbol{k}'\boldsymbol{k}}[3,1] = \bar{V}^{\downarrow\downarrow\downarrow\uparrow}_{\boldsymbol{k}'\boldsymbol{k}} - \bar{V}^{\downarrow\downarrow\uparrow\downarrow}_{\boldsymbol{k}'\boldsymbol{k}} = -\bar{V}^{\downarrow\downarrow\uparrow\downarrow}_{(-\boldsymbol{k}')\boldsymbol{k}} - \bar{V}^{\downarrow\downarrow\uparrow\downarrow}_{\boldsymbol{k}'\boldsymbol{k}} \tag{D.3.21a}$$

$$\equiv -2\bar{V}^{\downarrow\downarrow\uparrow\downarrow E(\boldsymbol{k}')}_{\boldsymbol{k}'\boldsymbol{k}}, \tag{D.3.21b}$$

$$\boldsymbol{\mathcal{V}}_{\boldsymbol{k}'\boldsymbol{k}}[3,2] = \bar{V}^{\downarrow\downarrow\uparrow\uparrow}_{\boldsymbol{k}'\boldsymbol{k}}, \tag{D.3.22}$$

$$\boldsymbol{\mathcal{V}}_{\boldsymbol{k}'\boldsymbol{k}}[3,3] = \bar{V}^{\downarrow\downarrow\downarrow\downarrow}_{\boldsymbol{k}'\boldsymbol{k}}, \tag{D.3.23}$$

$$\boldsymbol{\mathcal{V}}_{\boldsymbol{k}'\boldsymbol{k}}[3,4] = \bar{V}^{\downarrow\downarrow\downarrow\uparrow}_{\boldsymbol{k}'\boldsymbol{k}} + \bar{V}^{\downarrow\downarrow\uparrow\downarrow}_{\boldsymbol{k}'\boldsymbol{k}} = -\bar{V}^{\downarrow\downarrow\uparrow\downarrow}_{(-\boldsymbol{k}')\boldsymbol{k}} + \bar{V}^{\downarrow\downarrow\uparrow\downarrow}_{\boldsymbol{k}'\boldsymbol{k}} \tag{D.3.24a}$$

$$\equiv 2\bar{V}^{\downarrow\downarrow\uparrow\downarrow O(\boldsymbol{k}')}_{\boldsymbol{k}'\boldsymbol{k}}. \tag{D.3.24b}$$

At last, we write the fourth element of $|\xi_{\boldsymbol{k}}\rangle$, $\xi^{E(s)}_{\boldsymbol{k}\uparrow\downarrow}$

$$\begin{aligned}\xi^{E(s)}_{\boldsymbol{k}\uparrow\downarrow}(\boldsymbol{k}') = -\frac{1}{2}\Big[&\left(\bar{V}^{\uparrow\downarrow\downarrow\uparrow}_{\boldsymbol{k}'\boldsymbol{k}} - \bar{V}^{\uparrow\downarrow\uparrow\downarrow}_{\boldsymbol{k}'\boldsymbol{k}}\right)\xi^{O(s)}_{\boldsymbol{k}'\uparrow\downarrow} + \bar{V}^{\uparrow\downarrow\uparrow\uparrow}_{\boldsymbol{k}'\boldsymbol{k}}\xi_{\boldsymbol{k}'\uparrow\uparrow} \\ &+ \bar{V}^{\uparrow\downarrow\downarrow\downarrow}_{\boldsymbol{k}'\boldsymbol{k}}\xi_{\boldsymbol{k}'\downarrow\downarrow} + \left(\bar{V}^{\uparrow\downarrow\downarrow\uparrow}_{\boldsymbol{k}'\boldsymbol{k}} + \bar{V}^{\uparrow\downarrow\uparrow\downarrow}_{\boldsymbol{k}'\boldsymbol{k}}\right)\xi^{E(s)}_{\boldsymbol{k}'\uparrow\downarrow} \\ &+ \left(\bar{V}^{\downarrow\uparrow\downarrow\uparrow}_{\boldsymbol{k}'\boldsymbol{k}} - \bar{V}^{\downarrow\uparrow\uparrow\downarrow}_{\boldsymbol{k}'\boldsymbol{k}}\right)\xi^{O(s)}_{\boldsymbol{k}'\uparrow\downarrow} + \bar{V}^{\downarrow\uparrow\uparrow\uparrow}_{\boldsymbol{k}'\boldsymbol{k}}\xi_{\boldsymbol{k}'\uparrow\uparrow} \\ &+ \bar{V}^{\downarrow\uparrow\downarrow\downarrow}_{\boldsymbol{k}'\boldsymbol{k}}\xi_{\boldsymbol{k}'\downarrow\downarrow} + \left(\bar{V}^{\downarrow\uparrow\downarrow\uparrow}_{\boldsymbol{k}'\boldsymbol{k}} + \bar{V}^{\downarrow\uparrow\uparrow\downarrow}_{\boldsymbol{k}'\boldsymbol{k}}\right)\xi^{E(s)}_{\boldsymbol{k}'\uparrow\downarrow}\Big].\end{aligned} \tag{D.3.25}$$

Collecting the elements of $|\xi_{\boldsymbol{k}'}\rangle$, gives

$$\begin{aligned}\xi^{O(s)}_{\boldsymbol{k}\uparrow\downarrow}(\boldsymbol{k}') = -\frac{1}{2}\Big[&\left(\bar{V}^{\uparrow\downarrow\downarrow\uparrow}_{\boldsymbol{k}'\boldsymbol{k}} - \bar{V}^{\uparrow\downarrow\uparrow\downarrow}_{\boldsymbol{k}'\boldsymbol{k}} + \bar{V}^{\downarrow\uparrow\downarrow\uparrow}_{\boldsymbol{k}'\boldsymbol{k}} - \bar{V}^{\downarrow\uparrow\uparrow\downarrow}_{\boldsymbol{k}'\boldsymbol{k}}\right)\xi^{O(s)}_{\boldsymbol{k}'\uparrow\downarrow} \\ &+ \left(\bar{V}^{\uparrow\downarrow\uparrow\uparrow}_{\boldsymbol{k}'\boldsymbol{k}} + \bar{V}^{\downarrow\uparrow\uparrow\uparrow}_{\boldsymbol{k}'\boldsymbol{k}}\right)\xi_{\boldsymbol{k}'\uparrow\uparrow} + \left(\bar{V}^{\uparrow\downarrow\downarrow\downarrow}_{\boldsymbol{k}'\boldsymbol{k}} + \bar{V}^{\downarrow\uparrow\downarrow\downarrow}_{\boldsymbol{k}'\boldsymbol{k}}\right)\xi_{\boldsymbol{k}'\downarrow\downarrow} \\ &+ \left(\bar{V}^{\uparrow\downarrow\downarrow\uparrow}_{\boldsymbol{k}'\boldsymbol{k}} + \bar{V}^{\uparrow\downarrow\uparrow\downarrow}_{\boldsymbol{k}'\boldsymbol{k}} + \bar{V}^{\downarrow\uparrow\downarrow\uparrow}_{\boldsymbol{k}'\boldsymbol{k}} + \bar{V}^{\downarrow\uparrow\uparrow\downarrow}_{\boldsymbol{k}'\boldsymbol{k}}\right)\xi^{E(s)}_{\boldsymbol{k}'\uparrow\downarrow}\Big].\end{aligned} \tag{D.3.26}$$

In similar manner, we may now conclude the four elements of the fourth row of the coupling matrix.

$$\boldsymbol{\mathcal{V}}_{\boldsymbol{k}'\boldsymbol{k}}[4,1] = \frac{1}{2}\left(\bar{V}^{\uparrow\downarrow\downarrow\uparrow}_{\boldsymbol{k}'\boldsymbol{k}} - \bar{V}^{\uparrow\downarrow\uparrow\downarrow}_{\boldsymbol{k}'\boldsymbol{k}} + \bar{V}^{\downarrow\uparrow\downarrow\uparrow}_{\boldsymbol{k}'\boldsymbol{k}} - \bar{V}^{\downarrow\uparrow\uparrow\downarrow}_{\boldsymbol{k}'\boldsymbol{k}}\right) \tag{D.3.27a}$$

$$= \frac{1}{4}\left(\widetilde{V}_{(-\boldsymbol{k}')(-\boldsymbol{k})} + \widetilde{V}_{\boldsymbol{k}'(-\boldsymbol{k})} - \widetilde{V}_{(-\boldsymbol{k}')\boldsymbol{k}} - \widetilde{V}_{\boldsymbol{k}'\boldsymbol{k}}\right) \tag{D.3.27b}$$

$$\equiv \widetilde{V}^{E(\boldsymbol{k}')O(\boldsymbol{k})}_{\boldsymbol{k}'\boldsymbol{k}}, \tag{D.3.27c}$$

$$\boldsymbol{\mathcal{V}}_{\boldsymbol{k}'\boldsymbol{k}}[4,2] = \frac{\bar{V}^{\uparrow\downarrow\uparrow\uparrow}_{\boldsymbol{k}'\boldsymbol{k}} + \bar{V}^{\downarrow\uparrow\uparrow\uparrow}_{\boldsymbol{k}'\boldsymbol{k}}}{2} = \frac{\bar{V}^{\uparrow\downarrow\uparrow\uparrow}_{\boldsymbol{k}'\boldsymbol{k}} - \bar{V}^{\uparrow\downarrow\uparrow\uparrow}_{\boldsymbol{k}'(-\boldsymbol{k})}}{2} \tag{D.3.28a}$$

$$\equiv \bar{V}^{\uparrow\downarrow\uparrow\uparrow O(\boldsymbol{k})}_{\boldsymbol{k}'\boldsymbol{k}}, \tag{D.3.28b}$$

$$\boldsymbol{\mathcal{V}}_{\boldsymbol{k}'\boldsymbol{k}}[4,3] = \frac{\bar{V}^{\uparrow\downarrow\downarrow\downarrow}_{\boldsymbol{k}'\boldsymbol{k}} + \bar{V}^{\downarrow\uparrow\downarrow\downarrow}_{\boldsymbol{k}'\boldsymbol{k}}}{2} = \frac{\bar{V}^{\uparrow\downarrow\downarrow\downarrow}_{\boldsymbol{k}'\boldsymbol{k}} - \bar{V}^{\uparrow\downarrow\downarrow\downarrow}_{\boldsymbol{k}'(-\boldsymbol{k})}}{2} \tag{D.3.29a}$$

$$\equiv \bar{V}^{\uparrow\downarrow\downarrow\downarrow O(\boldsymbol{k})}_{\boldsymbol{k}'\boldsymbol{k}}, \tag{D.3.29b}$$

$$\boldsymbol{\mathcal{V}}_{\boldsymbol{k}'\boldsymbol{k}}[4,4] = \frac{1}{2}\left(\bar{V}^{\uparrow\downarrow\downarrow\uparrow}_{\boldsymbol{k}'\boldsymbol{k}} + \bar{V}^{\uparrow\downarrow\uparrow\downarrow}_{\boldsymbol{k}'\boldsymbol{k}} + \bar{V}^{\downarrow\uparrow\downarrow\uparrow}_{\boldsymbol{k}'\boldsymbol{k}} + \bar{V}^{\downarrow\uparrow\uparrow\downarrow}_{\boldsymbol{k}'\boldsymbol{k}}\right) \tag{D.3.30a}$$

$$= \frac{1}{4}\left(\widetilde{V}_{(-\boldsymbol{k}')(-\boldsymbol{k})} - \widetilde{V}_{\boldsymbol{k}'(-\boldsymbol{k})} - \widetilde{V}_{(-\boldsymbol{k}')\boldsymbol{k}} + \widetilde{V}_{\boldsymbol{k}'\boldsymbol{k}}\right) \tag{D.3.30b}$$

$$\equiv \widetilde{V}^{O(\boldsymbol{k}')O(\boldsymbol{k})}_{\boldsymbol{k}'\boldsymbol{k}}. \tag{D.3.30c}$$

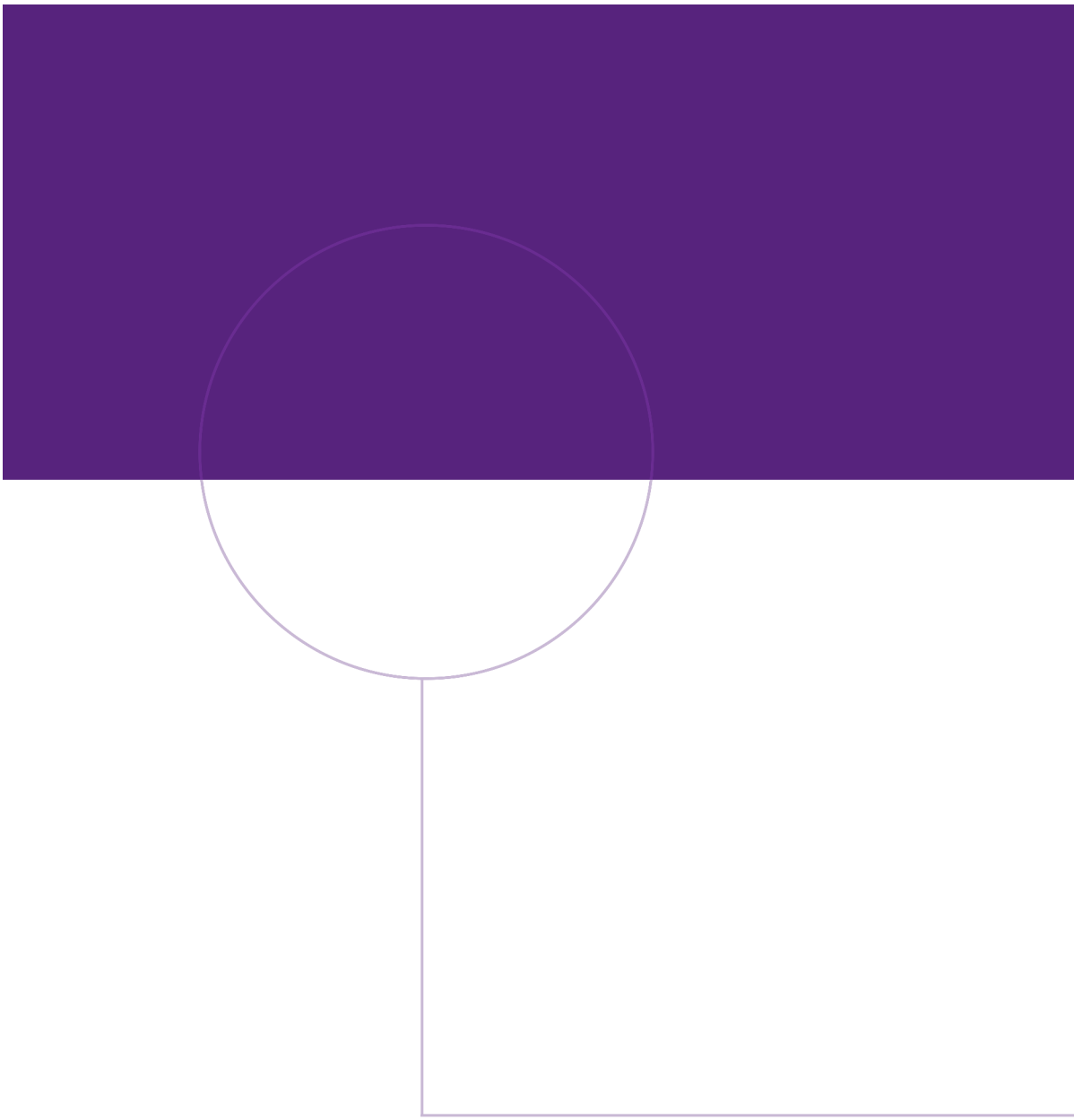

NTNU

Norwegian University of
Science and Technology